



DEPARTMENT OF PHYSICS

UNIVERSITY OF CAPE TOWN

IYUNIVESITHI YASEKAPA • UNIVERSITEIT VAN KAAPSTAD

Search for tWZ production in the Full Run 2 ATLAS
dataset using events with four leptons

Jake Reich

Student Number: RCHJAK001

Supervisor: Dr. James Keaveney

Co-Supervisor: Dr. Sahal Yacoob

A thesis submitted in fulfilment
of the requirements for the degree of
Master in Science

August 2021

Abstract

The search for tWZ production using 139 fb^{-1} of pp collision data at a centre-of-mass energy of $\sqrt{s} = 13 \text{ TeV}$, recorded by the ATLAS experiment at CERN, is presented. Events containing exactly four electrons or muons (tetralepton) are selected with additional criteria based on the number of jets, the number of b -tagged jets, and the number of Z boson candidates are used to define signal and control regions. The large $t\bar{t}Z$ and ZZ backgrounds are distinguished from signal by a BDT-based algorithm. Inputs to the BDT-based algorithm include, a kinematic reconstruction algorithm which reconstructs leptonically decaying top quarks and a BDT-based algorithm which aims to classify ℓb systems originating from top quarks. The expected signal strength is extracted via a blinded maximum-likelihood fit to multiple signal and control regions. The measured signal strength is $\mu(tWZ) = 1.91^{+0.95}_{-0.82}$, leading to an expected significance of 1.44σ . An expected upper limit on the signal strength is set and is given by $\mu_{up}^{exp} = 1.61^{+2.35}_{-1.16}$. Furthermore, a combined blinded maximum-likelihood fit was performed across the tetralepton and trilepton (studied in an independent analysis) channels, to further increase the sensitivity of $\sigma(tWZ)$. The measured signal strength is $\mu(tWZ) = 1.80^{+0.70}_{-0.65}$, leading to an expected significance of 1.61σ . An expected upper limit on the signal strength is set and is given by $\mu_{up}^{exp} = 1.43^{+2.04}_{-1.03}$.

Declaration

*17 I certify that this assignment/report is my own work, based on my personal study and/or research and that I have
18 acknowledged all material and sources used in its preparation, whether they be books, articles, reports, lecture notes,
19 and any other kind of document, electronic or personal communication. I also certify that this assignment/report
20 has not previously been submitted for assessment in any other unit, except where specific permission has been granted
21 from all unit coordinators involved, or at any other time in this unit, and that I have not copied in part or whole
22 or otherwise plagiarised the work of other students and/or persons.*

Acknowledgements

24

Contents

25	1 Introduction	7
26	2 Theory	8
27	2.1 Standard Model of Particle Physics	8
28	2.1.1 The Top Quark	9
29	2.2 tWZ	11
30	2.2.1 Tetralepton Channel	11
31	2.2.2 Comparison to Trilepton Channel	12
32	3 The ATLAS Experiment and Detector	14
33	3.1 The ATLAS Experiment	14
34	3.1.1 Large Hadron Collider (LHC)	14
35	3.2 The ATLAS Detector	15
36	3.2.1 Coordinate System and Kinematics	16
37	3.2.2 Inner Detector	16
38	3.2.3 Electromagnetic and Hadronic Calorimeters	17
39	3.2.4 Muon Spectrometer	17
40	3.2.5 Trigger and Data Acquisition System	17
41	3.2.6 Particle Identification and Object Reconstruction	17
42	4 Search for tWZ production using events with four leptons	20
43	4.1 Data and Monte Carlo Simulation	20
44	4.1.1 Data Samples	20
45	4.1.2 Monte Carlo Samples	20
46	4.1.3 Trigger Strategy	21
47	4.2 Physics objects	23
48	4.2.1 Leptons	23
49	4.2.2 Jets	23
50	4.2.3 b -tagging	24
51	4.2.4 Overlap Removal Procedure	24
52	4.3 Kinematic cuts	24
53	4.4 Regions and Event Selection	24
54	4.4.1 Optimization studies for event selection	26
55	4.5 Signal and Control Regions	28
56	4.5.1 tWZ OF SR	29
57	4.5.2 tWZ SF SR	29
58	4.5.3 $t\bar{t}Z$ CR	29
59	4.5.4 ZZb CR	32
60	4.5.5 $(tWZ)_{\text{fake}}$ CR	32
61	4.6 Fake Lepton Estimation	34
62	4.7 Improving signal vs background discrimination	37
63	4.7.1 Two Neutrino Scanning Method ($2\nu\text{SM}$) Algorithm	37
64	4.7.2 Boosted Decision Trees	40
65	4.7.3 Object-level BDT	42
66	4.7.4 Event-level BDT	48

67	4.8 Systematic Uncertainties	51
68	4.8.1 Experimental uncertainties	51
69	4.8.2 Theoretical uncertainties	54
70	4.8.3 Generic shape systematic uncertainties	54
71	4.9 Analysis Pipeline and TRexFitter	55
72	4.9.1 Fitting Procedure	55
73	4.10 Results	57
74	4.10.1 Tetralepton Channel	57
75	4.10.2 Trilepton and Tetralepton Channels	60
76	5 Summary and Conclusions	64

77

Chapter 1

78

Introduction

79 The production of a single top quark in association with a W^\pm and Z boson (tWZ) at the CERN LHC is sensitive
 80 to both the neutral and charged electroweak couplings of the top quark as the process involves the simultaneous
 81 production of a W boson and a Z boson in association with the top quark. Due to the very large coupling of
 82 the top quark to the Higgs boson, the electroweak couplings of the top quark are a theoretically well-motivated
 83 area in which to search for the first signs of new physics [80, 52] that could offer a resolution to the Hierarchy
 84 Problem [62, 30]. The recent lack of signs of new physics from LHC data tells us that new physics is either very
 85 heavy, or is very weakly coupled to Standard Model particles, therefore signs of new physics might only be observed
 86 in anomalous rates of well-chosen processes. A prime example of such a process is tWZ . This has an extremely low
 87 production cross section (≈ 160 fb for $\sqrt{s} = 13$ TeV [25]), meaning that it is an extremely rare process to observe
 88 and subsequently, it has never been observed by any particle physics experiment.

89

90 The latest datasets recorded by the ATLAS experiment at the CERN LHC are sufficiently large to allow a potential
 91 observation of tWZ production. In this analysis, the Full Run 2 dataset recorded by ATLAS is used to search for
 92 tWZ production in the tetralepton channel (tWZ with exactly four final state leptons). A kinematic reconstruction
 93 technique is used which aims to discriminate between tWZ and our most prominent background process, $t\bar{t}Z$. In
 94 addition to this, Machine Learning techniques are implemented to further isolate our tWZ signal. Backgrounds
 95 from Standard Model (SM) processes including those in which one or more leptons originate from the semileptonic
 96 decay of a heavy hadron or a photon conversion are estimated by fitting predictions from simulation to data in
 97 dedicated control regions. As this work forms the basis of an official ATLAS analysis, only blinded results are shown.
 98 A maximum likelihood fit is performed over our two tWZ signal regions and three control regions, to measure the
 99 cross section of tWZ in the tetralepton channel. In this thesis only the tetralepton channel is explored, however,
 100 the results of a combined fit that includes an entirely independent analysis of the trilepton channel is presented
 with no overlap of events between the regions defined for these channels.

102

Chapter 2

103

Theory

2.1 Standard Model of Particle Physics

105 The SM is a model based on Quantum Field Theory (QFT) which classifies all known elementary particles and
 106 describes their interactions. It is a well-tested model and has shown to be hugely successful in describing experimental data to great precision [8, 7]. For example, in the top quark sector, the $t\bar{t}$ cross section predictions have
 107 been confirmed to 3.9% accuracy [40, 71]. It incorporates three of the four fundamental forces of nature: the
 108 electromagnetic, the weak and the strong forces. In Figure 1, all known elementary particles described by the SM,
 109 are shown.

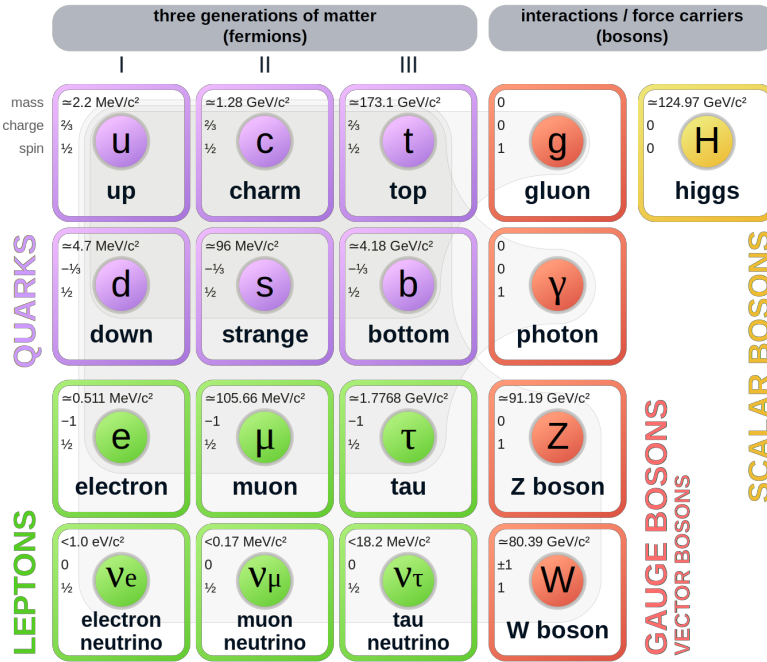


Figure 1: A summary of the elementary particles described by the SM [75] is shown. Fermions are shown on the left, with quarks shown in purple and leptons shown in green. Bosons are shown on the right, with gauge bosons shown in red and the Higgs boson shown in yellow. The mass, electric charge and spin of each particle is shown on the top left of each particle's block.

111 Particles in the SM are uniquely described by their quantum numbers: electric charge and spin. The SM particles
 112 are split into main two classes, based off their spin quantum numbers. Particles which have half-integer spin are
 113 called fermions, and those which have integer spin are called bosons. Fermions are further divided into three genera-
 114 tions, each comprising of two quarks, one charged lepton and one neutrino. In a generation, the more massive quark
 115 has an electric charge of $+2/3$ (up-type) and the less massive quark has an electric charge of $-1/3$ (down-type). All

116 charged leptons have an electric charge of -1 and all neutrinos are electrically neutral. The masses of the particles
 117 in a generation increase with increasing generation number, with generation 1 particles being the least massive and
 118 generation 3 particles being the most massive. Quarks carry electric and colour charge, and can therefore interact
 119 via the electromagnetic, weak and strong forces. Colour charge can take on three values: red, green and blue.
 120 It is important to note that colour charge is completely unrelated to the everyday meaning of colour, and it just
 121 represents the quantum state of the particle. Due to colour confinement [100], quarks cannot be isolated from one
 122 another. They exist in colourless bound states, called hadrons, consisting of two or more quarks. Hadrons consisting
 123 of an even number of quarks are known as mesons and those consisting of an odd number of quarks are known as
 124 baryons. On the other hand, charged leptons (electron (e), muon (μ) and tau (τ)) only carry electric charge and
 125 can therefore interact electromagnetically and weakly, but not through the strong interaction. The electric and
 126 colour neutral fermions, neutrinos, can only interact via the weak force.

127
 128 Particles are able to interact with one-another via the exchange of a gauge boson (boson with spin-1). Photons
 129 are massless, spin-1 gauge bosons which mediate electromagnetic interactions between particles which carry electric
 130 charge, such as quarks and charged leptons (e , μ and τ). The weak interaction is mediated by three massive gauge
 131 bosons, the electrically charged W^+ and W^- bosons and the electrically neutral Z boson. Gluons are massless,
 132 spin-1 gauge bosons which mediate strong interactions between particles which carry colour charge, such as quarks.
 133 Since gluons carry colour charge, they interact with themselves. The massive, spin-0, electrically neutral Higgs
 134 boson mediates the Higgs field which gives mass to the W^\pm and Z bosons via the so-called Brout-Englert-Higgs
 135 mechanism [46, 58, 57]. The Brout-Englert-Higgs mechanism induces spontaneous electroweak symmetry breaking
 136 to provide mass terms for the W^\pm and Z bosons in the electroweak Lagrangian of the SM. All particles described in
 137 the SM have their own antiparticle, with the same mass, but opposite charges. Some particles, such as the photon,
 138 are their own antiparticle.

139
 140 Although the SM is hugely successful, it is incomplete and fails to describe certain observed phenomena. The most
 141 notable example being the absence of gravity. The gravitational force is $\approx 10^{29}$ [92] weaker than the weak force,
 142 therefore quantum gravitational effects are expected to only become significant at energies much larger than that
 143 currently accessible by the LHC (known as the Planck scale $\approx 10^9$ GeV) [62]. This large difference in strength
 144 between the weak force and gravity is known as the Hierarchy Problem. Cosmological observations infer that around
 145 84% of the matter in the universe consists of gravitationally interacting matter known as dark matter [61]. None
 146 of the particles described in the SM are good dark matter candidates, therefore the SM only accounts for a small
 147 fraction of the total matter of the universe. The large discrepancy between the observed amount of matter and
 148 antimatter in the universe, sometimes referred to as the matter-antimatter asymmetry, is not fully explained by
 149 the SM. Neutrinos in the SM are assumed to be massless, however observations of neutrino oscillations (neutrinos
 150 undergoing flavour change as they travel through space) imply that neutrinos do have mass [49]. Beyond the
 151 Standard Model (BSM) theories attempt to explain the phenomena which the SM cannot. For example, a popular
 152 extension to the SM, Supersymmetry (SUSY) introduces new particles to the SM which are counterparts to the
 153 existing SM particles with the same quantum numbers, except for their spins [64]. It provides elegant explanations
 154 to many shortcomings of the SM, however none of the supersymmetric particles described by SUSY have been
 155 observed experimentally [34].

156 2.1.1 The Top Quark

157 The top quark is the heaviest particle in the SM, with a mass of 172.76 ± 0.30 GeV [55]. According to the SM, since
 158 the coupling to the Higgs boson is proportional to the the mass of the interacting particle, the top quark is strongly
 159 coupled to the Higgs boson. Therefore, physics processes involving top quarks is a theoretically well-motivated area
 160 to search for new physics, since top quarks are the most likely particles to couple to new physics theories at the TeV
 161 scale. Its large mass also makes it highly unstable, with a mean lifetime of $\approx 0.5 \times 10^{-24}$ s [55]. The top quark's
 162 lifetime is shorter than that of the hadronisation process, and it therefore decays before hadronising. The top quark
 163 can therefore be measured indirectly via its decay products. Top quarks almost always decay to a W boson and
 164 a b -quark ($\frac{\Gamma(Wb)}{\Gamma(Wq(q=b,s,d))} = 0.957 \pm 0.034$ [55]). The b -quark is the second heaviest quark in the SM, however its
 165 lifetime is still longer than the hadronisation time scale [55]. In hadron collider experiments, b -quarks travel a short
 166 distance in the detector before hadronising to form jets. In Table 1, the dominant final state branching fractions of
 167 the top quark are shown.
 168 Top quark decays with hadronic final states are more than twice as likely than those with leptonic final states.
 169 Final state decays to different lepton flavours are roughly equally probable.

Decay Mode	Branching Fraction ($\frac{\Gamma_i}{\Gamma}$)
$t \rightarrow Wb \rightarrow e\nu_e b$	$(11.10 \pm 0.30)\%$
$t \rightarrow Wb \rightarrow \mu\nu_\mu b$	$(11.40 \pm 0.20)\%$
$t \rightarrow Wb \rightarrow \tau\nu_\tau b$	$(10.70 \pm 0.50)\%$
$t \rightarrow Wb \rightarrow q\bar{q}b$	$(66.50 \pm 1.40)\%$

Table 1: The dominant final state branching fractions of the top quark [55] are shown.

170
171 Top quark production can be placed into two main categories: pair production ($t\bar{t}$) and single-top production (t) [88].
172 In the LHC, top quarks are mainly produced in pairs via strong interactions in gluon-gluon fusion ($gg \rightarrow t\bar{t}$) or quark
173 annihilation ($q\bar{q} \rightarrow t\bar{t}$). Top quark production via gluon-gluon fusion is the dominating process [23]. The production
174 cross section for $t\bar{t}$ (leptonic final state) in pp collisions with $\sqrt{s} = 13$ TeV was measured by ATLAS with a value
175 of $830 \pm 0.4(\text{stat}) \pm 36(\text{syst}) \pm 14(\text{lumi})$ pb [4], with good agreement between measurement and theoretical prediction.
176

177 Single top production occurs via the weak interaction. The most abundant production mechanisms leading to
178 single top production are the s -, t - and Wt - channels [55]. In the s -channel, an initial quark annihilates with an
179 anti-quark of different flavour, producing a virtual W boson which decays to a top quark and anti-bottom quark.
180 In the t -channel, an initial b quark interacts with a different flavour quark via the exchange of a W boson. This
181 interaction produces a top quark and another quark. In the Wt -channel, an initial gluon interacts with a b quark
182 to produce a top quark and a W boson, either via the absorption of the gluon by the b quark or via the exchange
183 of a top quark. In Table 2, single top production cross sections in pp collisions at $\sqrt{s} = 13$ TeV for the s -, t - and
184 Wt -channels, are shown.

Channel	Process	Total Cross Section [pb]
s	$q\bar{q}' \rightarrow W \rightarrow \bar{b}t$	$10.32^{+0.40}_{-0.36}$
t	$bq' \rightarrow W \rightarrow tq$	$216.99^{+9.04}_{-7.71}$
Wt	$bg \rightarrow b/t \rightarrow Wt$	71.7 ± 3.85

Table 2: Single top production cross sections in pp collisions at $\sqrt{s} = 13$ TeV for the s -, t - and Wt -channels [35]
are shown. The prime superscript on q' indicates that the quark has a different flavour to q .

185 Single top production is suppressed compared to pair produced top production, with $t\bar{t}$ production (leptonic final
186 state) being around three times as likely to occur than single top production across all decay channels.
187

2.1.1.1 Motivation for the search for tWZ production in the tetralepton channel

188 The recent lack of signs of new physics from LHC data [91] tells us that new physics is either very heavy, or is
189 very weakly coupled to SM particles. We therefore might only observe signs of new physics in anomalous rates of
190 well-chosen processes. The tWZ process is a prime example of such a process. It has an extremely low production
191 cross section of ≈ 160 fb for $\sqrt{s} = 13$ TeV [25], and has subsequently never been observed by any particle physics
192 experiment. Since tWZ involves a charged W boson and neutral Z boson, its cross section is sensitive to the
193 charged and neutral couplings to the top quark. In turn, the top quark is strongly coupled to the Higgs boson, due
194 to its large mass. Due to the top quark's large coupling to the Higgs boson, corrections to the Higgs boson mass
195 diverge in the SM. The top quark's couplings are modified, in order to remove this divergence, in many scenarios of
196 new physics that aim to resolve the Hierarchy Problem. Since the Z boson may be radiated from the initial-state
197 b -quark, the final-state top quark, or the final-state Z boson, the tWZ process embeds the $b - Z$, $t - Z$ and $W - Z$
198 electroweak couplings which are often modified in BSM physics. Therefore tWZ is an important process in the
199 search for signs of new physics and BSM physics.
200

201 One such BSM theory which is sensitive to tWZ production [66, 73] is the Standard Model Effective Field Theory
202 (SMEFT) [27]. The SMEFT attempts to describe physics at large energy scales which we have not yet been able

203 to probe experimentally. The SMEFT inherits the same QFT framework as the SM, and adds terms to the SM La-
 204 grangian which describe the interactions of SM particles at higher energy scales. Analogous to the coupling constants
 205 found in the SM Lagrangian, which indicate the interaction strengths between different particles, SMEFT contains
 206 scalar coefficients which operate in the same way. These scalar coefficients are known as Wilson coefficients. It has
 207 been shown that the cross section of tWZ is sensitive to many Wilson coefficients. An experimental constraint on
 208 the cross section of tWZ is therefore expected to be impactful on a global fit on all the Wilson coefficients in SMEFT.

209
 210 Prior to this analysis, only three experimental studies of tWZ in ATLAS have been performed. Two of the studies
 211 utilised the trilepton channel to search for tWZ production, whereas the third study utilised both the tri- and
 212 tetralepton channels. The first search utilised 36 fb^{-1} of ATLAS data and an upper limit on the cross section of
 213 tWZ was set at a value of ≈ 6 times the SM cross section [79]. The second search in the trilepton channel utilised
 214 139 fb^{-1} of ATLAS data and an expected upper limit on the cross section of tWZ was set at a value of ≈ 2.6 times the
 215 SM cross section [99]. In Section 4.10.2, the aforesaid analysis will be used in combination with this analysis,
 216 in order to further increase the sensitivity of the cross section of tWZ . The third study investigated the feasibility
 217 of a cross section measurement of tWZ production with CMS Run 3 data (300 fb^{-1}) [98], by utilising the tri- and
 218 tetralepton channels. The study showed that it is possible to exclude $\mu(tWZ)$ at the 7σ significance level using
 219 300 fb^{-1} of data. This study needs to be further investigated, since its findings seem improbable given the results
 220 obtained in this thesis.

221 2.2 tWZ

222 2.2.1 Tetralepton Channel

223 In Figure 2, the Leading Order (LO) Feynman diagram for tWZ in the tetralepton channel, is shown.

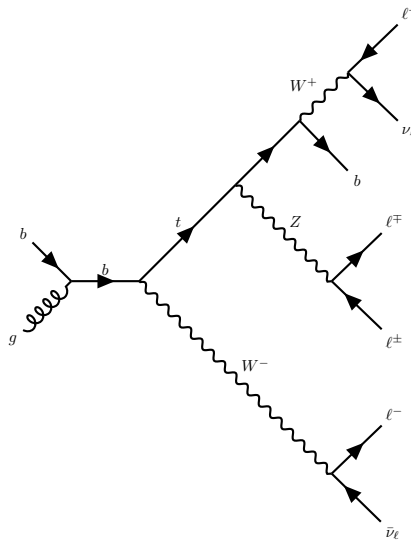


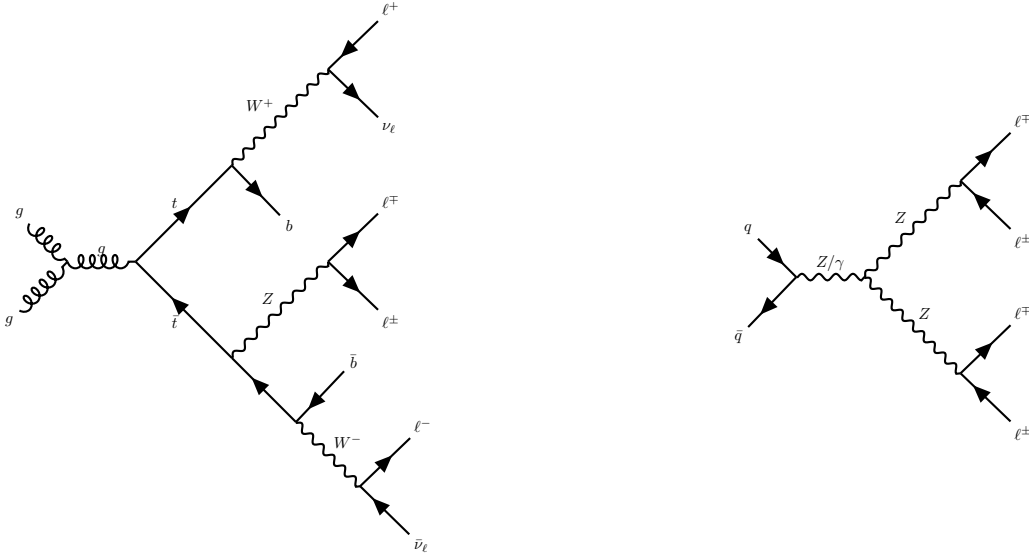
Figure 2: The LO Feynman diagram of tWZ production in the tetralepton channel is shown.

224 2.2.1.1 Backgrounds

225 The main backgrounds for tWZ (tetralepton channel) are the production of a two tops, both in the $\ell\nu b^1$ final state
 226 channel, together with a Z boson ($t\bar{t}Z$) and diboson production with fully leptonic final states (ZZ). In Figure
 227 2.2.1.1, LO Feynman diagrams for $t\bar{t}Z$ and ZZ in the tetralepton channel, are shown.

¹In this thesis, ℓ refers to an electron or muon, ν refers to a neutrino or anti-neutrino and b refers to a bottom quark or anti-bottom quark

228



229

Figure 3: The LO Feynman diagrams for $t\bar{t}Z$ (left) and ZZ (right) in the tetralepton channel are shown.

230 The $t\bar{t}Z$ process contains four leptons and two b -quarks in its final state ($\sigma_{(t\bar{t}Z).Br(4\ell)}^{\text{NLO}} = 0.95 \pm 0.08_{\text{stat}} \pm 0.10_{\text{syst}}$
 231 pb at $\sqrt{s} = 13$ TeV [2]) and can easily mimic the tWZ signal process, for instance, by one of its b -jets getting
 232 missed during detection. The ZZ process contains four leptons and zero b -quarks in its final state ($\sigma_{(ZZ).Br(4\ell)}^{\text{NNLO}} =$
 233 $14.6^{+1.9}_{-1.8}(\text{stat})^{+0.5}_{-0.3}(\text{syst}) \pm 0.2(\text{theo}) \pm 0.4(\text{lumi})$ pb at $\sqrt{s} = 13$ TeV [63]). One way in which ZZ can mimic the tWZ
 234 signal process is by reconstruction of a non-prompt b -jet.

235 2.2.2 Comparison to Trilepton Channel

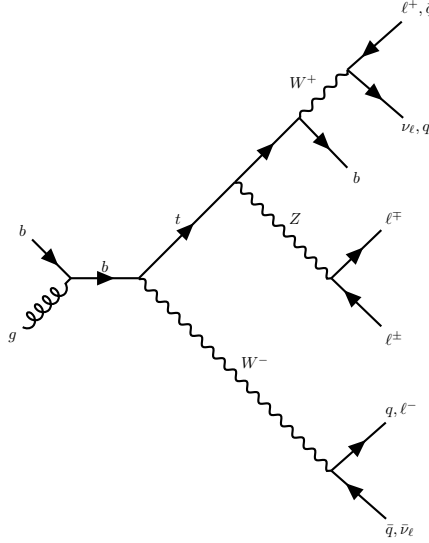


Figure 4: The LO Feynman diagram of tWZ production in the tri-lepton channel.

236 The most apparent difference between the tri and tetralepton channels is the number of events present, with the
 237 tetralepton channel having far less events in its phase space than that of the tri-lepton channel. The lack of statistics
 238 in the tetralepton channel can be attributed to its low cross section times branching ratio of $\sigma_{(tW^\pm Z).Br(4\ell)}^{\text{NLO}} =$
 239 0.7 fb [25]. The tri-lepton channel has a cross section times branching ratio of $\sigma_{(tW^\pm Z).Br(3\ell)}^{\text{NLO}} = 3.9$ fb [25], which is
 240 around a factor of four larger than that of the tetralepton channel. This difference between the production cross

241 section of the two decay channels can be largely attributed to the difference in branching ratios ($\frac{\Gamma_i}{\Gamma}$) between a
242 hadronically decaying W boson, $\frac{\Gamma_{W \rightarrow had}}{\Gamma_W} = (67.41 \pm 0.27)\%$ [55], present in the tri-lepton channel and a leptonically
243 decaying W boson, $\frac{\Gamma_{W \rightarrow \ell\nu}}{\Gamma_W} = (10.86 \pm 0.09)\%$ [55], present in the tetralepton channel. Despite the tetralepton
244 channel's low statistics, it is not subject to the large WZ background present in the trilepton channel [99]. The
245 tetralepton channel has a substantial amount of ZZ background (not present in the trilepton channel), fortunately
246 this can be easily suppressed due to the full reconstructability of the two leptonically decaying Z -bosons.

247

Chapter 3

The ATLAS Experiment and Detector

248

249 3.1 The ATLAS Experiment

250 The ATLAS (A Toroidal LHC ApparatuS) detector is one of two general purpose detectors at CERN (the European
 251 Organization for Nuclear Research) near Geneva in Switzerland. These detectors collect data from the collisions
 252 provided by the worlds highest energy particle accelerator [29], the Large Hadron Collider (LHC) situated at CERN.

253 In this section, information about the LHC and the ATLAS detector are given. This includes technical aspects
 254 of the ATLAS detector and the processing of data into meaningful physics objects¹ to be used in analyses. The
 255 following chapter consists of information from "The LHC Design Report" [29], "LHC Machine" [48] and "The
 256 ATLAS Experiment at the CERN Large Hadron Collider" [41] unless otherwise stated.

258 3.1.1 Large Hadron Collider (LHC)

259 The LHC is a circular 27 km particle accelerator located in an underground tunnel on the border between France
 260 and Switzerland. The accelerator consists of supercooled, superconducting magnets which accelerate and collide
 261 beams of protons at centre-of-mass energies up to $\sqrt{s} = 13$ TeV at instantaneous luminosities of $\mathcal{L} \sim 10^{34}$ cm $^{-2}$ s $^{-1}$.
 262 In the LHC, pp beams consist of bunches of protons which collide every 25 ns, corresponding to a frequency of 40
 263 MHz. Several accelerator systems are used to accelerate protons and heavy ions to such high energies. Protons are
 264 extracted from a tank of ionised hydrogen gas and are injected into the Linear Accelerator 2 (LINAC), where they
 265 are linearly accelerated to momenta of 50 MeV. The proton bunches are then sequentially accelerated by a chain
 266 of circular accelerators. The chain starts with the Booster which accelerates the protons to momenta of up to 1.4
 267 GeV. The proton bunches are then fed through to the Proton Synchrotron (PS) and the Super Proton Synchrotron
 268 (SPS) which accelerate the protons to momenta of up to 25 GeV and 450 GeV respectively. The protons are
 269 then transferred to two beam pipes of the LHC where they travel in opposite directions. Both proton beams are
 270 accelerated to their final momenta of 6.5 TeV, resulting in a centre-of-mass energy of 13 TeV. These proton beams
 271 then collide at one of the four main interaction points (positions along the beam pipe where collisions occur)
 272 situated along the LHC.

273 The four main experiments located at the interaction points are ATLAS, the Compact Muon Solenoid (CMS),
 274 Large Hadron Collider Beauty (LHCb) Experiment and A Large Ion Collider Experiment (ALICE). The ATLAS
 275 and CMS detectors are general-purpose detectors which investigate a wide range of physics processes. Since both
 276 ATLAS and CMS can measure the same processes, they are able to cross-check and validate measurements taken
 277 by one another. The LHCb detector is specifically designed to study decays of particles containing b -quarks. The
 278 ALICE detector is designed to study the strongly interacting quark-gluon plasma which is formed at extremely
 279 high energy densities. At the interaction points, the two proton beams which consist of protons in closely packed
 280 bunches, travel in opposite directions to one another and collide. Many hard pp collisions (events) can occur per
 281 bunch crossing, however it is the most energetic collision in the bunch crossing that is interesting for discovery
 282 potential. The most energetic collision is therefore chosen to be studied and any additional collisions are aimed
 283 to be rejected. These additional collisions are referred to as *pile-up*. Pileup complicates the reconstruction of the
 284 particles originating from the hard collision of interest.

¹a detector signal (or a combination of detector signals) that represent a candidate for a particle (e.g leptons and jets)

286 **3.1.1.1 Luminosity**

287 This section consists of information from "Modern Particle Physics" [92], unless otherwise stated. The event
288 production rate at the LHC, $R(t)$, for a certain process of interest is given by,

$$R(t) = \mathcal{L}(t)\sigma \quad (3.1)$$

289 where $\mathcal{L}(t)$ is the instantaneous luminosity and σ and is the cross section of the process of interest. The instantaneous
290 luminosity, $\mathcal{L}(t)$, is independent on the process of interest, and depends on various collider and beam parameters.
291 $\mathcal{L}(t)$ can be written in terms of these parameters as,

$$\mathcal{L}(t) = f \frac{N n_1 n_2}{4\pi \sigma_x \sigma_y} \quad (3.2)$$

292 where f is the beam revolution frequency, N is the number of proton bunches colliding per second, n_1 and n_2 are the
293 number of protons in the colliding bunches, σ_x and σ_y are the beam spread in the x and y directions respectively.
294 The average number of visible (particles that are measurable by the detector) pp interactions per bunch crossing,
295 $\langle\mu\rangle$, can be written as,

$$\langle\mu\rangle = \frac{\sigma_{inel}\mathcal{L}}{Nf} \quad (3.3)$$

296 where σ_{inel} is the inelastic pp interaction cross section. The total integrated luminosity, L , across some time interval,
297 is given by,

$$L = \int \mathcal{L} dt. \quad (3.4)$$

298 The units of L are inverse area, and are given by fb^{-1} at the LHC and the ATLAS detector. In Figure 5, the total
299 integrated luminosity vs time, recorded by ATLAS for $\sqrt{s} = 13$ TeV pp collisions at the LHC is shown [94].

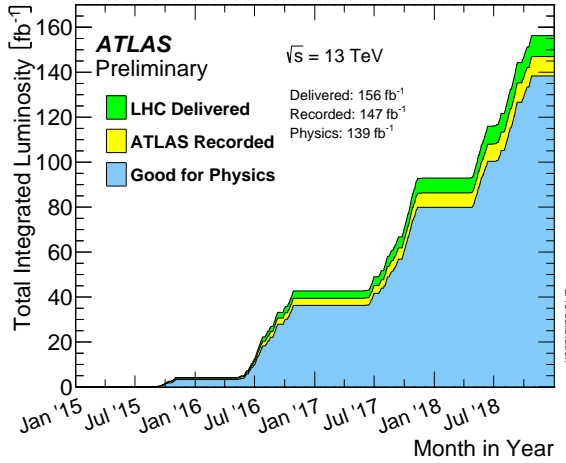


Figure 5: The total integrated luminosity vs time, recorded by ATLAS for $\sqrt{s} = 13$ TeV pp collisions at the LHC
is shown [94]. The total integrated luminosity delivered by the LHC, recorded by ATLAS and certified to be good
quality data are shown by the green, yellow and blue histograms respectively. The month and year of data taking
is shown on the x-axis and the total integrated luminosity (in fb^{-1}) is shown on the y-axis.

300 A total integrated luminosity of 139 fb^{-1} of data certified as good for physics was recorded by ATLAS between
301 2015 and 2018. This data taking period is referred to as Run 2. It occurred after the Run 1 data taking period
302 (2011 and 2012) and the Long Shutdown 1 LHC upgrade period (2013 and 2014). In this analysis, we use the Full
303 Run 2 dataset.

304 **3.2 The ATLAS Detector**

305 In Figure 6, the schematic of the ATLAS detector, is shown.

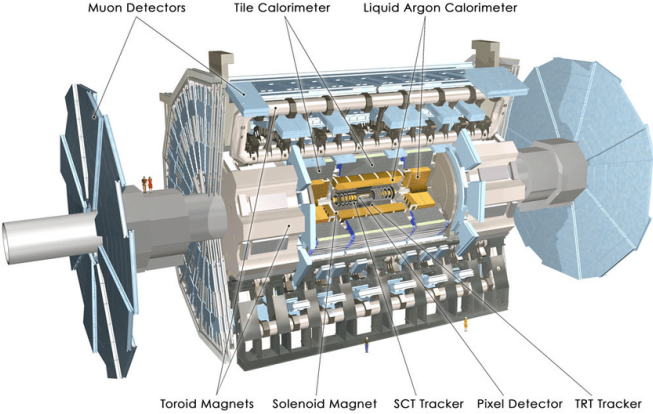


Figure 6: A schematic of the ATLAS detector is shown. [41]

306 The detector is cylindrically shaped which covers close to 4π in solid angle. It has a length of 44 m, a diameter
 307 of 25 m and a mass of 7000 tons. The ATLAS detector consists of four main sub-detectors arranged in concentric
 308 cylindrical layers around the beam pipe. These include the inner detector, the electromagnetic calorimeter,
 309 the hadronic calorimeters and the muon spectrometer. The sub-detectors record the momenta, energies and trajectories
 310 of different particles produced in the collider, allowing for the reconstruction and identification of these particles to
 311 be used in physics analyses.

312 3.2.1 Coordinate System and Kinematics

313 The ATLAS detector adopts a right-handed coordinate system. The origin is at the nominal interaction point
 314 with the z -axis defined to be counter-clockwise along the beam line. The $x - y$ plane (or transverse plane) is
 315 perpendicular to the beam line, with the x -axis pointing towards the centre of the LHC ring and the y -axis
 316 pointing upwards towards the Earth's surface. The azimuthal angle, $\phi \in [-\pi, \pi]$, is measured in the transverse
 317 plane with respect to the positive x -axis. The polar angle, $\theta \in [0, \pi]$, is measured in the $z - y$ plane with respect
 318 to the positive y -axis. A quantity called the pseudorapidity, $\eta \in [0, \infty]$ is defined as,

$$\eta = -\ln \tan\left(\frac{\theta}{2}\right) \quad (3.5)$$

319 The polar angle, η , is often used instead of θ , since the difference in η between two particles, $\Delta\eta$, is invariant under
 320 a Lorentz boost in the z -direction [95]. The angular distance between two physics objects, ΔR , can be written as,

$$\Delta R = \sqrt{(\Delta\phi)^2 + (\Delta\eta)^2} \quad (3.6)$$

321 where $\Delta\phi$ is the difference in ϕ between the two physics objects of interest. Quantities defined in the transverse
 322 plane are often used to describe the kinematics of physics objects in hadron collider experiments. The transverse
 323 momentum, p_T , is defined as,

$$p_T = \sqrt{(p_x)^2 + (p_y)^2} \quad (3.7)$$

324 where p_x and p_y are the x and y components of the physics object's momenta, respectively. The transverse energy,
 325 E_T , is defined as,

$$E_T = \sqrt{m^2 + p_T^2} \quad (3.8)$$

326 where m is the invariant mass of the physics object.

327 3.2.2 Inner Detector

328 The inner detector is the first layer of concentric cylindrical sub-detector layers in the ATLAS detector. It is used
 329 to identify charged particles and reconstruct the trajectories of charged particles produced in the collisions via
 330 energy deposition in semiconductor material (hits) and the ionisation of gas. It consists of three complementary
 331 sub-detectors (in order from nearest to farthest from the beam pipe): the Pixel Detector, the Semiconductor Tracker

(SCT) and the Transition Radiation Detector (TRT). The Pixel Detector and SCT are based on semiconductor technology and have the highest granularity of any sub-detector in ATLAS, in order to cope with the high frequency of collisions near the interaction point. The TRT consists of drift tubes (straws) containing a gas mixture, which allows measurement of the energy deposited by charged particles through the ionisation of the gas. Solenoid magnets surround the inner detector and bend the trajectories of charged particles. The charges and transverse momenta of particles can be inferred from their bent trajectories, which are reconstructed by the hits produced via energy deposition in the Inner Detector.

3.2.3 Electromagnetic and Hadronic Calorimeters

The Electromagnetic Calorimeter (ECAL) and Hadronic Calorimeter (HCAL) surround the Inner Detector, with the ECAL nearer to the beam line. The ECAL and HCAL provide accurate measurements of the energy of particles which interact electromagnetically (e.g. photons and electrons) and hadronically (e.g. jets), respectively. Particles entering the calorimeters interact with the detector material and create either a electromagnetic shower (in the ECAL) or a hadronic shower (in the HCAL), depositing all their energy in the calorimeter cells. The primary mechanism of energy deposition in the ECAL is through bremsstrahlung (for electrons) and pair production (photons). Hadrons usually deposit a small amount of their energy in the ECAL, and interact via inelastic scattering with the nuclei of the detector material. The hadronic showers (jets) produced in these nuclear interactions travel much further than an electromagnetic shower, and for that reason, the volume of the HCAL is designed to occupy a much larger space than that of the ECAL.

3.2.4 Muon Spectrometer

The Muon Spectrometer (MS) is the outermost sub-detector of ATLAS and surrounds the HCAL. Muons traverse through the inner detector and calorimeters, with minimal energy loss, before reaching the MS. The MS consists of trigger and high-precision tracking systems. Large superconducting toroid shaped magnets deflect the incoming muons to measure their trajectories and subsequently their momenta via the curvature of the trajectories. The MS measures muon trajectories as they ionize gas (filled with Ar and CO₂ gas) in the MS drift chambers.

3.2.5 Trigger and Data Acquisition System

The Trigger and Data Acquisition System (TDAQ) manages and handles the large amount of data produced within the ATLAS detector. In Run 2, pp bunch crossings occur every 25 ns, corresponding to an event rate of 40 MHz. The TDAQ system performs a fast preliminary reconstruction to select events with signatures which are interesting for physics analyses. The information collected from these events are permanently stored for offline reconstruction and analysis, and the rest (the vast majority of events) are discarded. The trigger system reduces the 40 MHz data rate to around 1 kHz.

3.2.6 Particle Identification and Object Reconstruction

Particles originating from pp collisions, or from their subsequent decays, traverse through the ATLAS detector and interact with its different sub-detectors, producing characteristic electronic signals. These signals are then processed by various algorithms to reconstruct and identify the physics objects (e.g. electrons, muons, jets) in the event. This section outlines the procedures used to define these physics objects.

3.2.6.1 Tracks and primary vertices

The trajectories of charged particles, or tracks, are reconstructed in the ID. First, energy is deposited by charged particles (hits) in pixels or strips, in the Pixel and SCT detectors respectively. Adjacent pixels or strips are grouped together in *energy clusters*. Energy clusters define 3D space-points indicating the location where the charged particle traversed. Track seeds are then defined as sets of three space-points, in either the Pixel or SCT detectors. A Kalman filter [11] is then used to build track candidates from the track seeds. Often, multiple track candidates are built per track seed, therefore an ambiguity solver [38] is needed for finding the track which best represents the traversal of the charged particle. The ambiguity solver ranks each track from a given seed based on, the number of associated hits, the number of holes (expected hits which are absent), track momenta and the χ^2 of the track fit. Low ranked tracks are then discarded. High ranked tracks are refitted, introducing information from the TRT.

379 The primary vertex is the location of the pp collision of interest (i.e. from the hard scatter). The primary vertex
 380 from the hard scatter needs to be identified, to isolate the event of interest from unwanted pile-up events. In the
 381 event reconstruction procedure [72], the primary vertex is defined as the vertex of the event with the largest sum
 382 of $(p_T)^2$ (corresponding to the measured $(p_T)^2$ of the particle from its reconstructed track) of its associated tracks.
 383 Furthermore, the primary vertex is required to have at least two associated tracks. To reduce contamination from
 384 fake tracks used in primary vertex reconstruction, only tracks which pass certain tight selection criteria are used
 385 in the reconstruction procedure. An iterative fitting procedure is then used to reconstruct the primary vertex by
 386 finding a set of reconstructed tracks which have a common vertex.

387 3.2.6.2 Electrons

388 Since electrons are charged particles, they give rise to tracks in the Inner Detector. They also deposit energy in the
 389 ECAL via electromagnetic showering. Electrons are therefore reconstructed and identified from signals in the Inner
 390 Detector and ECAL. Electrons are reconstructed using a dynamic clustering algorithm [1] which matches electron
 391 candidate tracks in the Inner Detector to energy clusters in the ECAL. The dynamic clustering algorithm matches
 392 tracks to energy clusters which have local maxima, to form electron candidates.
 393 A likelihood discriminant is used to identify electrons. Quantities measured in the Inner Detector and ECAL
 394 are used as input, such that they discriminate well between prompt isolated electrons and other physics objects
 395 (e.g. jets, electron from a photon conversion, electron from a semi-leptonically decaying hadron). Important input
 396 variables include the shape of the electromagnetic shower, track quality in the Inner Detector and information from
 397 the TRT.

398 3.2.6.3 Muons

399 Muons leave tracks in the Inner Detector and the MS. They traverse the ECAL and HCAL with no significant
 400 energy loss. Muons are therefore reconstructed and identified from information in the Inner Detector and MS.
 401 Tracks are reconstructed [5] in the Inner Detector and MS independently. Both tracks are combined, using a global
 402 χ^2 fit, resulting in reconstructed muon candidates.

403 Similar to electron identification, muons use a likelihood discriminant to identify prompt muons and suppress
 404 background contamination (mainly from pion and kaon decays).

406 3.2.6.4 Jets and b -tagging

407 Coloured particles emerging from the interaction point result in collimated streams of colourless particles, known
 408 as jets. Jets can deposit energy in the Inner Detector and in the HCAL. Jets in ATLAS are reconstructed from
 409 topological clusters using the anti- k_t algorithm [31]. Topological clusters are groups of adjacent calorimeter cells
 410 which contain energy deposition above the average amount of noise expected in the cell. Adjacent cells are grouped
 411 together under certain criteria to form topological clusters which form jets.

412 Different tagging algorithms are used to identify the quark flavour which initiated a jet. b -quark tagging is used
 413 extensively in top physics, due to the b -quark present in the top quark's dominant decay channel (See Table
 414 1). Hadrons arising from b -quark hadronisation have mean lifetimes ~ 1.5 ps and travel (on average) a few
 415 millimetres before decaying. This creates a secondary vertex within the jet (See Figure 7). This characteristic decay
 416 signature, along with several other unique features of b -jets, are exploited in b -tagging algorithms to distinguish
 417 b -jets from c - or light flavour jets. In Figure 7, an illustration of the production of a b -jet, is shown.
 418 In this analysis, we use the recommended DL1r (Deep-Learning Flavour Tagger) tagging algorithm [17]. The DL1r
 419 algorithm combines outputs from several low-level tagging algorithms using a Deep Neural Network and outputs
 420 the probability that a given input jet is identified as a b , c or light flavoured jet.

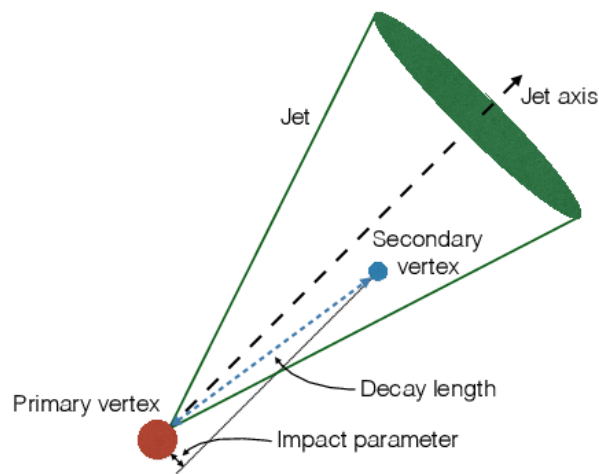


Figure 7: An illustration [42] of the production of a b -jet is shown. This illustrates the presence of a secondary vertex within a b -jet.

422

Chapter 4

423

Search for tWZ production using events with four leptons

424

425 In this chapter, the analysis is presented for tWZ production in the tetralepton channel based on an integrated
426 luminosity of 139 fb^{-1} of data recorded by ATLAS. This includes a description of the data and simulated Monte
427 Carlo (MC) samples, definitions of physics objects, event selection and the subsequent definition of signal and control
428 regions used in this analysis. Furthermore, estimation of the fake lepton component using the MC template method
429 is described. A kinematic reconstruction algorithm and various Machine Learning techniques, used to discriminate
430 between signal and background events, are described. An outline of the systematic uncertainties affecting the
431 measurement are presented. Finally, the results of the analysis and a study of the analysis projected to higher
432 luminosities is presented.

433

4.1 Data and Monte Carlo Simulation

434

4.1.1 Data Samples

435 The pp collision data used in this analysis was collected with the ATLAS detector at the LHC from 2015 to
436 2018. This data period of data taking is referred to as Run 2. During this period, pp collisions at $\sqrt{s} = 13 \text{ TeV}$,
437 corresponding to an integrated luminosity of 156 fb^{-1} , were delivered by the LHC. The ATLAS detector managed
438 to record 147 fb^{-1} of this total delivered data. 139 fb^{-1} of the data recorded by ATLAS is considered to be good
439 enough for physics analyses (the data passes certain quality control criteria) and placed into the *Good Runs List* [54].
440 Specific time-intervals where the luminosity is assumed to be constant are known as *lumi-blocks*. Only events from
441 lumi-blocks in which LHC beams were stable and all ATLAS detectors were operational are selected. The list
442 of suitable run and lumi-blocks is summarised in the official Good Runs Lists for 2015-2018 data, as specified in
443 Ref. [53]. The integrated luminosities corresponding to the individual datasets for years 2015, 2016, 2017 and 2018
444 are 3.2 fb^{-1} , 33.0 fb^{-1} , 44.3 fb^{-1} and 58.5 fb^{-1} respectively.

445

4.1.2 Monte Carlo Samples

446 Simulated MC samples were generated and used to model the SM tWZ signal and its backgrounds. The following
447 background processes are considered:

- 448 • **$t\bar{t}Z$:** $t\bar{t}$ with an associated Z -boson, in the tetralepton final state. Therefore, both top quarks decay leptonically
449 (e.g. $t \rightarrow W^+ b \rightarrow \ell^+ \nu b$) and of these top quarks emits a Z -boson which decays leptonically ($Z \rightarrow \ell^\pm \ell^\mp$ (OSSF
450 lepton pair)). This results in a final state with 4 leptons and 2 b-quarks.
- 451 • **ZZ :** Diboson production with a tetralepton final state, therefore both Z -bosons decay leptonically ($Z \rightarrow \ell^\pm \ell^\mp$
452 (OSSF lepton pair)).
- 453 • **other:** Processes with a relatively minimal, but non-negligible background contribution
 - VVV ($V = W/Z$)
 - $t\bar{t}$

454

455

- $t\bar{t}W$
- $t\bar{t}WW$
- $t\bar{t}H$
- WZ
- $t\bar{t}t$
- $t\bar{t}\bar{t}\bar{t}$
- tZq

The MC simulations are achieved via the use of event generators and parton shower generators. The parton shower generators simulate any incoming or outgoing particles from the hard process, which carry QCD color charge and can therefore lead to parton showers. The production of tWZ events is simulated with the **MADGRAPH5_AMC@NLO 2.3.3** [9] generator providing matrix element (ME) calculations at NLO (next-to-leading order) in QCD. The events are interfaced with **PYTHIA 8.235** for the parton shower. The production of $t\bar{t}Z$ and $t\bar{t}W$ events are simulated with the **MADGRAPH5_AMC@NLO 2.3.3** generator providing ME calculations at NLO in QCD. The events are interfaced with **PYTHIA 8.210** [90] for the parton shower. Event generation of tWZ and $t\bar{t}Z$ results in diagrams which overlap with one another, that is, these diagrams contain the same initial and final state particles. Several methods exist in order to separate between the two processes, by removing the overlap, therefore avoiding double counting. There are two different diagram removal procedures, diagram removal procedure 1 (DR1) [44] and diagram removal procedure 2 (DR2). The DR1 scheme is used to remove the overlap (interference) between tWZ and $t\bar{t}Z$. A comparison to the DR2 scheme is used to estimate part of the theoretical systematic on the modelling of the tWZ signal (See Section 4.8.2). Diboson processes which feature the three charged leptons and one neutrino or four charged lepton in their final states, such as WZ and ZZ , are simulated using **SHERPA 2.2.2** [26] at NLO in QCD precision. The events are interfaced with **SHERPA** for the parton shower. Triboson processes such as WWW , WWZ , WZZ , and ZZZ containing up to six leptons in their final states are simulated using **SHERPA 2.2.2** at NLO in QCD precision. The events are interfaced with **SHERPA** for the parton shower. The production of $t\bar{t}$ events are simulated with the **POWHEG** [51] generator providing ME calculations at NLO in QCD. The events are interfaced with **PYTHIA 8.210** for the parton shower. The production of $t\bar{t}t$, $t\bar{t}\bar{t}\bar{t}$ and $t\bar{t}WW$ are simulated using the **MADGRAPH5_AMC@NLO 2.2.2** generator at LO in QCD precision. The events are interfaced with **PYTHIA 8.186** [89] for the parton shower. The production of $t\bar{t}$ with an associated Higgs boson, $t\bar{t}H$, are generated using the **MADGRAPH5_AMC@NLO 2.6.0** generator at NLO in QCD precision. The events are showered using **PYTHIA 8.230** [90]. The production of $t\bar{t}$ events are simulated with the **POWHEG** generator providing ME calculations at NLO in QCD. The events are showered using **PYTHIA 8.230**. The production of a single top quark in association with a Z-boson and an extra parton, tZq , is simulated using **MADGRAPH5_AMC@NLO 2.3.3** at NLO in QCD precision. The events are interfaced with **PYTHIA 8.230** for the parton shower. In Table 3, the event generator and parton shower used for each process's sample are shown.

Process	Event Generator	Cross section calculation	Parton Shower
tWZ	MADGRAPH5_AMC@NLO 2.3.3	NLO	PYTHIA 8.235
$t\bar{t}Z$	MADGRAPH5_AMC@NLO 2.3.3	NLO	PYTHIA 8.210
ZZ , WZ	SHERPA 2.2.2	NLO	SHERPA
VVV ($V = W/Z$)	SHERPA 2.2.2	NLO	SHERPA
$t\bar{t}$	POWHEG	NLO	PYTHIA 8.230
$t\bar{t}W$	MADGRAPH5_AMC@NLO 2.3.3	NLO	PYTHIA 8.210
$t\bar{t}WW$	MADGRAPH5_AMC@NLO 2.2.2	LO	PYTHIA 8.186
$t\bar{t}H$	MADGRAPH5_AMC@NLO 2.6.0	NLO	PYTHIA 8.230
$t\bar{t}t$, $t\bar{t}\bar{t}\bar{t}$	MADGRAPH5_AMC@NLO 2.2.2	LO	PYTHIA 8.186
tZq	MADGRAPH5_AMC@NLO 2.3.3	NLO	PYTHIA 8.230

Table 3: The event generator and parton shower used for the signal and background process's MC samples is shown.

4.1.3 Trigger Strategy

Events in data and simulation are selected via either single lepton or dilepton (electron or muon) triggers. To selected events, a logical **OR** between the triggers is applied. This means that events have to be selected by at least

one of the single or dilepton triggers. Electrons and muons may be surrounded by other particles which could lead to problems in the reconstruction and identification process. They are therefore required to be sufficiently isolated from other particles. This is done by defining an isolation variable which ensures that the summed energies of the particles in a cone defined around the muon, with radius ΔR , are small. The isolation variable for a cone of radius x , $I_{\Delta R=x}$, is given by,

$$I_{\Delta R=x} = \frac{\sum_i E_i}{p_T^{e/m}} \quad (4.1)$$

where E_i is the energy of the i^{th} particle within the cone and $p_T^{e/m}$ is the p_T of the electron or muon. In order to identify an electron or muon, various properties and detector signals related to them are fed into different Machine Learning classifiers to determine the likelihood of the particle being an electron or a muon. Cuts are applied to the output of the classifiers to define working points which correspond to different selection efficiencies. The names commonly given to different working points, in order of decreasing efficiency, are very loose, loose, medium and tight. The single-muon trigger used to select muons in 2015 data and simulation requires a muon with $p_T > 20$ GeV, an identification criteria corresponding to a loose working point and $I_{\Delta R=0.2} < 0.12$. Two single-muon triggers are used to select muons in 2016-2018 data and simulation. The first requires a muon with $p_T > 26$ GeV, an identification criteria corresponding to a medium working point and $I_{\Delta R=0.3} < 0.06$. The second requires a muon with $p_T > 50$ GeV. Two single-electron triggers are used to select electrons in 2015 data and simulation. The first requires an electron with $p_T > 24$ GeV and an identification criteria corresponding to a medium working point. The second requires an electron with $p_T > 120$ GeV and an identification criteria corresponding to a loose working point. Three single leptons triggers are used to select electrons in 2016-2018 data and simulation. The first requires an electron with $p_T > 26$ GeV, an identification criteria corresponding to a tight working point and $I_{\Delta R=0.2} < 0.1$. The second requires an electron with $p_T > 60$ GeV and an identification criteria corresponding to a medium working point. The third requires an electron with $p_T > 140$ GeV and an identification criteria corresponding to a loose working point. The di-muon trigger used to select muons in 2015 data and simulation requires that one muon have $p_T > 18$ GeV and another muon to have $p_T > 8$ GeV. The di-muon trigger used to select muons in 2016-2018 data and simulation requires that one muon have $p_T > 22$ GeV and another muon to have $p_T > 8$ GeV. The di-electron trigger used to select electrons in 2015 data and simulation requires two electrons, each with $p_T > 12$ GeV, and identification criteria corresponding to loose working points. The di-electron trigger used to select electrons in 2016-2018 data and simulation requires two electrons, each with $p_T > 17$ GeV, and identification criteria corresponding to very loose working points. A final electron-muon trigger is used to select electrons and muons in 2016-2018 data and simulation that requires an electron with $p_T > 17$ GeV and a muon with $p_T > 14$ GeV, and identification criteria corresponding to loose working points. In Table 4, a summary of the triggers used to select muons and electrons in data and simulation are shown.

Trigger	Selection [GeV]	Working Point
Single-muon*	$p_T > 20$	loose
Single-muon	$p_T > 26$	medium
Single-muon	$p_T > 50$	-
Single-electron*	$p_T > 24$	medium
Single-electron*	$p_T > 120$	loose
Single-electron	$p_T > 26$	loose
Single-electron	$p_T > 60$	medium
Single-electron	$p_T > 140$	loose
Di-muon*	$p_T > 18, p_T > 8$	-
Di-muon	$p_T > 18, p_T > 8$	-
Di-electron*	$p_T > 12$	loose
Di-electron*	$p_T > 12$	loose
Di-electron	$p_T > 17$	very loose
Electron-Muon	electron $p_T > 17$, muon $p_T > 14$	loose

Table 4: Single lepton and dilepton (electron and muon) triggers used to select events in data and simulation. Triggers labelled with * are only used for 2015 data and simulation.

524 4.2 Physics objects

525 In this section the physics objects (leptons, jets and b -tagged jets) used in this analysis are outlined.

526 4.2.1 Leptons

527 In this analysis only e and μ leptons are considered, since τ leptons are difficult to detect in the ATLAS detector.
 528 They are challenging to detect since they have an extremely short lifetime (290.3 ± 0.5 fs [55]) which causes them
 529 to decay before reaching any detector components and therefore can only be reconstructed via their decay products.
 530 In addition to our selection criteria of exactly four leptons, it is required that the Leading (L), Next-to-Leading
 531 (NL), Next-to-Next-to-Leading (NNL) and Next-to-Next-to-Next-to-Leading (NNNL) leptons have p_T greater than
 532 28, 18, 10 and 10 GeV respectively. Relatively loose object-level cuts are chosen in an attempt to maximize our
 533 signal statistics, since the analysis is heavily statistically limited. Reconstructed electrons are required to be within
 534 $|\eta| < 2.47$ and excluding the transition region between the barrel and end-cap calorimeters at $1.37 < |\eta| < 1.52$.
 535 Reconstructed muons are required to be within $|\eta| < 2.5$. The transverse impact parameter, d_0 , is defined as the
 536 minimal spatial distance between the object's (referring to leptons) trajectory and the primary vertex (the vertex
 537 associated with the p - p hard scatter). The longitudinal impact parameter, z_0 , is defined as the value of z of the
 538 point on the object's trajectory which determines d_0 . To ensure consistency between the lepton and the primary
 539 vertex, it is required that $|\frac{d_0}{\sigma(d_0)}| < 5$, $|z_0 \sin \theta| < 0.5$ mm for electrons and $|\frac{d_0}{\sigma(d_0)}| < 3$, $|z_0 \sin \theta| < 0.5$ mm for muons,
 540 following the current recommendations [93]. To avoid instances where one detector signal can result in multiple
 541 different reconstructed objects, an overlap removal procedure is applied which ignores all but one of these objects
 542 (See Section 4.2.4). Electrons are selected using a likelihood based discriminant [1] which takes measurements
 543 from the tracking system, calorimeter system and quantities derived from both the tracking and calorimeter system
 544 as input. Muons are selected using the Muon Selection Tool [78]. Loose electrons are defined with the criteria
 545 above, using the LooseAndBLayerLH ($\sim 91\%$ selection efficiency for electrons with $E_T > 30$ GeV [45]) identification
 546 algorithm (which has a certain cut applied). Similarly, tight electrons are defined with the criteria above, using
 547 the TightLH ($\sim 80\%$ selection efficiency for electrons with $E_T > 30$ GeV [45]) algorithm (which has a certain cut
 548 applied). Both loose and tight muons use the Medium ($\sim 95\%$ selection efficiency [5]) algorithm (which has a certain
 549 cut applied). Tight leptons additionally require that they are sufficiently isolated from other particles produced
 550 in the collision. This is done by defining a cone of radius $\Delta R = \sqrt{\Delta\eta^2 + \Delta\phi^2}$ around the particle of interest and
 551 summing the p_T of all the reconstructed particles surrounding the particle of interest, situated within the cone.
 552 A quantity, I_{rel} , is then defined as, $I_{rel} = \frac{\sum p_T(\text{surrounding candidate})}{p_T(\text{candidate})}$, the ratio of this sum to the p_T of the lepton
 553 candidate. If this value is large, it is likely that the particle of interest originated from a jet (together with many
 554 other particles), whereas a prompt decay product resulting from the hard scatter will have little to no energy
 555 surrounding it ($I_{rel} \ll 1$). The IsolationSelectionTool with the PLVTight ($\sim 70\%$ efficiency [6]) and PLVTight
 556 ($\sim 70\%$ efficiency at $p_T = 30$ GeV [37]) algorithm are used for tight electrons and tight muons respectively (following
 557 the current recommendations [85]). In Table 5, a summary of the selection criteria for leptons is shown.

	Electrons		Muons	
	Tight	Loose	Tight	Loose
p_T cuts		$p_T(\ell_1, \ell_2, \ell_3, \ell_4) > (28, 18, 10, 10)$ GeV		
Overlap Removal		Described in Section 4.2.4		
η cuts	$ \eta(\ell_e) < 2.47$ excluding $1.37 < \eta(\ell_e) < 1.52$	$ \eta(\ell_\mu) < 2.5$		
Impact Parameters	$ \frac{d_0}{\sigma(d_0)} < 5$, $ z_0 \sin \theta < 0.5$ mm	$ \frac{d_0}{\sigma(d_0)} < 3$, $ z_0 \sin \theta < 0.5$ mm		
Identification WP	TightLH	LooseAndBLayerLH	Medium	Medium
Isolation WP	PLVTight	Not Used	PLVTight	Not Used

Table 5: A summary of the requirements applied for selecting tight and loose leptons (e, μ) is shown.

558 4.2.2 Jets

559 Jets are reconstructed using the anti- k_t algorithm (See Section 3.2.6.4). The AntiKt4EMPFlowjets ($\sim 97\%$ average
 560 efficiency with JVT (outlined in the subsequent paragraph) > 0.2 [93]) algorithm (which has a certain cut applied)
 561 is used, following the current recommendations [93]. The jet-vertex-tagger (JVT) and the forward jet-vertex-tagger

(fJVT) [50] are likelihood discriminant which aim to suppress pile-up jets. The `Medium` algorithm (which has a certain cut applied) is used for the JVT and the fJVT (following the current recommendations [83]). Additionally, a requirement that jets have a JVT value greater than 0.5 is applied. In the same way as with leptons, ambiguities are removed where one detector signal can result in multiple different reconstructed objects, via overlap removal (See Section 4.2.4). Jets are required to be within $p_T(\text{jet}) > 20 \text{ GeV}$. These relatively loose p_T cuts are applied in an attempt to increase our limited signal statistics. A forward jet is a signature of single top quark production, jets are therefore required to have $|\eta| < 4.5$ in order to include these forward jets.

4.2.3 b -tagging

The DL1r b -tagger [76] was used to identify jets as b -jets (See Section 3.2.6.4). Different DL1r working points are used to identify b -jets in our event selection (See Section 4.4). The working points are defined as different cuts on the DL1r score corresponding to a b -jet tagging efficiency of 60%, 70%, 77% and 85%. The efficiency of the DL1r b -tagger is measured using control samples in data and in simulation. From these measurements, correction factors are derived to correct the tagging rates in the simulation. In the case of b -tagged jets, the correction factors and their uncertainties are estimated from data using dileptonic $t\bar{t}$ events [15, 12]. Sources of uncertainty affecting the b -tagging efficiencies are evaluated as a function of jet p_T , including bin-to-bin correlations. Since this analysis is heavily statistically limited, the amount of statistics in our regions are aimed to be maximized. In an attempt to achieve this goal in the $t\bar{t}Z$ CR, b -tagged jets were placed under *tight* and *loose* definitions. A tight b -tagged jet is defined as a jet which passes the 77%, 70%, 65% or 60% DL1r b -tagger working point. A loose b -tagged jet is defined as a jet which passes 85% DL1r b -tagger working point, but not the 77%, 70%, 65% or 60% DL1r b -tagger working points. Different numbers and definitions of tight and loose b -tagged jets were tried in each region, with the final selection criteria being chosen which maximised the expected significance of $\sigma(tWZ)$ (See Section 4.4.1).

4.2.4 Overlap Removal Procedure

An overlap removal procedure is performed to avoid instances where one detector signal can result in multiple different reconstructed objects. The overlap removal procedure is used on pre-selected leptons and jets. It is performed sequentially, in the following steps:

- 587 1. If the separation between a pre-selected electron and pre-selected muon is within $\Delta R < 0.01$, or they share a
track, the pre-selected electron is discarded.
- 589 2. If the separation between a jet and a pre-selected electron is within $\Delta R < 0.2$, the jet is discarded.
- 590 3. Any remaining electron or muon closer than $\Delta R = 0.4$ to a jet, is discarded.
- 591 4. If the distance between a jet and a pre-selected muon is $\Delta R < 0.4$ and the jet has more than two associated
592 tracks, then the muon is discarded, otherwise the jet is discarded.

4.3 Kinematic cuts

In order to suppress potential fakes and quarkonia (low mass resonances such as J/ψ and upsilon) a requirement that all OSSF lepton pairs have an invariant mass, m_{OSSF} , greater than 10 GeV is applied. The final state lepton charges must sum to zero. Therefore a requirement of $\sum_{i=1}^4 \text{charge}(\ell_i) = 0$ is applied. The invariant mass of the OSSF lepton pair coming from the Z boson must equal the invariant mass of the Z boson, and noting that e, μ reconstruction and identification in the ATLAS detector has a high efficiency [67], these OSSF leptons are used to reconstruct Z bosons with relatively high confidence. A Z candidate is defined in this analysis as an OSSF lepton pair with an invariant mass, m_{OSSF} , satisfying the condition, $|m_{\text{OSSF}} - m_Z| < 30 \text{ GeV}$, where $m(Z)$ is the nominal Z boson mass (91.1876 GeV [55]). This wider mass window is used in order to cover the full range of the $m(Z)$ distribution, in an attempt to increase the number of events which pass our baseline selections. Multiple Z candidates can be present in certain decay channels (e.g. $eeee, \mu\mu ee, \mu\mu\mu\mu$). In these cases, the Z candidate which has an invariant mass closest to the nominal Z boson mass is chosen.

4.4 Regions and Event Selection

Two tWZ SRs are defined in an attempt to suppress and constrain the ZZ background. Both tWZ SRs are required to have exactly four tight leptons, exactly one Z -boson candidate, exactly one tight b -tagged jet (from the decay of

the top quark) and greater than or equal to one jet. The two tWZ SR's differ by the flavours of their leptons which don't originate from the decay of a Z -boson (non- Z leptons). The ZZ background has two Z -bosons which decay into a pair of OSSF lepton pairs, in order to mimic the tWZ signal. This is taken advantage of, to define a tWZ region enriched in ZZ background and one with a minimal ZZ background component. This is done by requiring that one of the tWZ SRs has its two non- Z leptons to have opposite flavour and the other tWZ SR is required to have its non- Z leptons to have the same flavour. These two disjoint tWZ SRs are named tWZ OF SR and tWZ SF SR respectively. It is therefore expected that the tWZ SF SR contains the majority of the ZZ background events across both tWZ SRs. In order to check the modelling of the most dominant background components in our signal region, $t\bar{t}Z$ and ZZb control regions are defined. The $t\bar{t}Z$ control region has the same requirement on the number of reconstructed Z boson candidates in the signal region (due to a commonality on the number of Z bosons present in both processes), however it is required that there are at least two jets and that exactly two of these jets are b -tagged (corresponding to the b -quark jets originating from the two top quark decays). A ZZb region is defined, as opposed to a ZZ region, since the ZZ background present in the tWZ signal region contains exactly one b -tagged jet. Therefore defining a region with ZZ plus exactly one b -jet more closely resembles the ZZ background present in the signal region. In addition to this, mis-modelling of ZZ has been seen in other analyses [3, 39], further motivating the use of a ZZb control region over a ZZ CR. The ZZb CR requires exactly two Z boson candidates and exactly one b -tagged jet, resulting in an implicit requirement on the number of jets ($N_{jet} \geq 1$).

Fake leptons are objects reconstructed as leptons, but do not correspond to the leptons that are of interest in our analysis. Fake leptons can be split up into two main categories, irreducible (prompt) fakes and reducible (non-prompt) fakes. Irreducible fakes are true leptons which do not come from the process of interest. Reducible fakes are objects which are mis-identified or incorrectly reconstructed as leptons. In the ATLAS detector, the probability for a fake to occur is very low. In order to constrain the fake lepton component contained within the $t\bar{t}Z$ sample, a $(tWZ)_{fake}$ CR is defined which is as similar as possible to the tWZ SRs but is enhanced in fakes. This is achieved by defining the $(tWZ)_{fake}$ CR to inherit the same selection criteria as the tWZ SRs however, in this case, a requirement of exactly 3 tight leptons and exactly 1 loose (and NOT tight) lepton is applied. Loose leptons are required in this region, since looser leptons are more likely to be fakes compared to tighter leptons. A $(t\bar{t}Z)_{fake}$ CR, requiring exactly 3 tight leptons and exactly 1 loose (and NOT tight) lepton, was tried as an alternative to the $(tWZ)_{fake}$ CR. This suppression of fakes can be explained by the extra b -tagged jet requirement (exactly two b -tagged jets are required in the $t\bar{t}Z$ region, compared to exactly one in the tWZ SRs (See Table 6)) which causes suppression of fakes via the overlap removal procedure (See Section 4.2.4). In Table 6, a summary of the final selection criteria and region definitions is shown.

Baseline selections				
$N_\ell = 4$				
$p_T(\ell_1, \ell_2, \ell_3, \ell_4) > (28, 10, 10, 10)$ GeV $p_T(\text{jet}) > 20$ GeV, $ \eta(\text{jet}) < 4.5$, $\text{jvt} > 0.5$ $ \eta(\ell_e) < 2.47$ excluding $1.37 < \eta(\ell_e) < 1.52$ $ \eta(\ell_\mu) < 2.5$ $\sum_{i=1}^4 \text{charge}(\ell_i) = 0$ All OSSF lepton pairs require $m_{\text{OSSF}} > 10$ GeV				
Regions				
tWZ OF SR	tWZ SF SR	$t\bar{t}Z$ CR	ZZb CR	$(tWZ)_{fake}$ CR
$N_\ell(\text{tight}) = 4$	$N_\ell(\text{tight}) = 4$	$N_\ell(\text{tight}) = 4$	$N_\ell(\text{tight}) = 4$	$N_\ell(\text{tight}) = 3$ $N_\ell(\text{loose and NOT tight}) = 1$
$N_Z \text{ candidate} = 1$	$N_Z \text{ candidate} = 1$	$N_Z \text{ candidate} = 1$	$N_Z \text{ candidate} = 2$	$N_Z \text{ candidate} = 1$
$N_{jet} \geq 1$	$N_{jet} \geq 1$	$N_{jet} \geq 2$	$N_{jet} \geq 1$	$N_{jet} \geq 1$
$N_{b\text{-jet}}(\text{tight}) = 1$	$N_{b\text{-jet}}(\text{tight}) = 1$	$N_{b\text{-jet}}(\text{tight}) \geq 1$ $N_{b\text{-jet}}(\text{loose}) \geq 0$ $N_{b\text{-jet}}(\text{tight}) + N_{b\text{-jet}}(\text{loose}) = 2$	$N_{b\text{-jet}}(\text{tight}) = 1$	$N_{b\text{-jet}}(\text{tight}) = 1$
Opp. Flavour non- Z leptons	Same Flavour non- Z leptons	-	-	-

Table 6: A summary of the requirements applied for selecting events in the signal and control regions is shown.

641 4.4.1 Optimization studies for event selection

642 In order to find the selection criteria for jets and leptons which maximized sensitivity to the tWZ signal, studies
 643 were performed by plotting the expected significance (Z_μ^{exp}) and expected upper limit (μ_{up}^{exp}) for different selection
 644 criteria. The fitting procedure as described in Section 4.9.1 was used to calculate the expected upper limits and
 645 expected significances in this study (these metrics are fully described later in Section 4.9.1). The same selection
 646 criteria and regions defined in Table 6 was used (unless otherwise specified), except for the selection(s) which were
 647 being optimised in each case. In Figure 8 the expected significance (Z_μ^{exp}) and expected upper limits (μ_{up}^{exp}) for
 different $\eta(jet)$ cuts are shown.

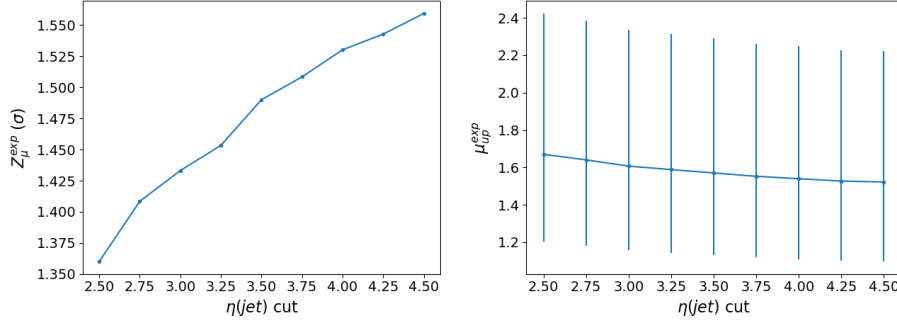


Figure 8: **Left:** Expected significance (Z_μ^{exp}) for different $\eta(jet)$ cuts is shown. The cuts applied on the $\eta(jet)$ are shown on the x-axis and corresponding expected significance from the likelihood fit is shown on the y-axis. **Right:** Expected upper limit (μ_{up}^{exp}) for different $\eta(jet)$ cuts is shown. The cuts applied on the $\eta(jet)$ are shown on the x-axis and corresponding expected upper limits are shown on the y-axis. Error bars representing the total uncertainty on the expected upper limits are shown as vertical lines.

648 From Figure 8, it can be seen that the $\eta(jet)$ cut which maximises the sensitivity of tWZ in the tetralepton channel
 649 is requiring that $\eta(jet) < 4.5$. This selection criteria was set for the $\eta(jet)$ across all regions. In Figure 9 the
 650 expected significance (Z_μ^{exp}) and expected upper limits (μ_{up}^{exp}) for different $p_T(jet)$ cuts are shown.

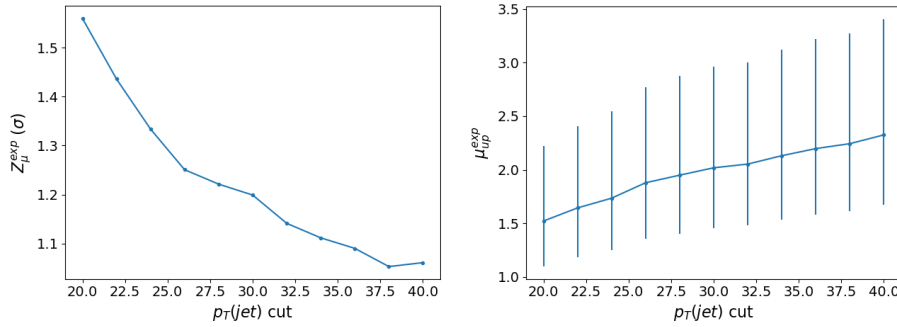


Figure 9: **Left:** Expected significance (Z_μ^{exp}) for different $p_T(jet)$ cuts is shown. The cuts applied on the $p_T(jet)$ are shown on the x-axis and corresponding expected significance from the likelihood fit is shown on the y-axis. **Right:** Expected upper limit (μ_{up}^{exp}) for different $p_T(jet)$ cuts is shown. The cuts applied on the $p_T(jet)$ are shown on the x-axis and corresponding expected upper limits are shown on the y-axis. Error bars representing the total uncertainty on the expected upper limits are shown as vertical lines.

651 From Figure 9, it can be seen that the $p_T(jet)$ cut which maximises the sensitivity of tWZ is requiring that
 652 $p_T(jet) > 20$ GeV. This selection criteria was set for the $p_T(jet)$ across all regions. In Figure 10 the expected
 653 significance (Z_μ^{exp}) and expected upper limits (μ_{up}^{exp}) for a range of different configurations of DL1r b -tagged jet
 654 working points across different regions.

655 From Figure 10, it can be seen that requiring that b -tagged jets pass the 77% DL1r WP in the tWZ SR, $(tWZ)_{fake}$
 656 CR and the ZZb CR and that at least one b -tagged jet in the $t\bar{t}Z$ SR passes the 77% DL1r WP (the other jet
 657 is just required to pass the 85% DL1r WP) maximises the sensitivity overall (compared to the other investigated
 658 configurations). This configuration was chosen b -tagged jets. The $p_T(L \text{ Lepton})$ is constrained by the single lepton
 659 configuration.

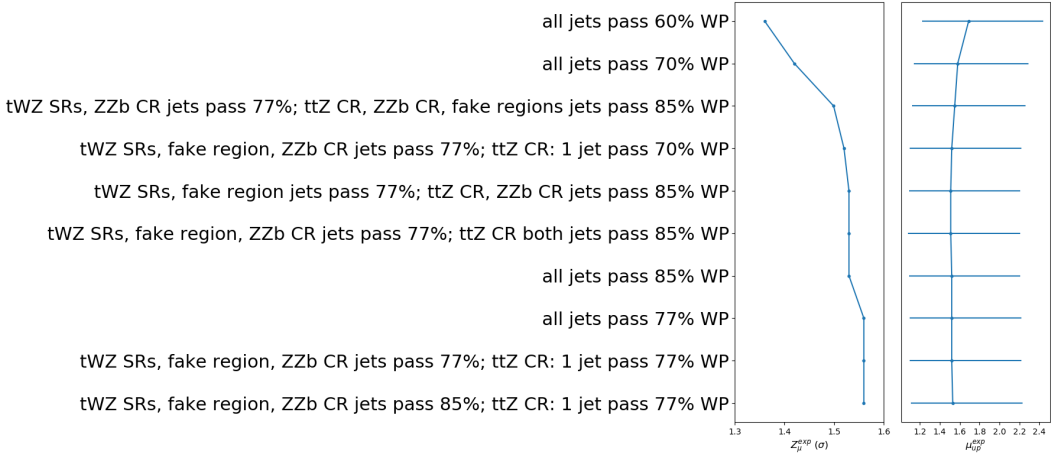


Figure 10: Expected significance (Z_μ^{exp}) and expected upper limit ($\mu_{\text{up}}^{\text{exp}}$) for different configurations of DL1r b -tagged jet working points is shown. The common y-axis shows the different configurations of DL1r b -tagged jet working points. On the left panel, the expected significance from the likelihood fit is shown on the x-axis. On the right panel, the expected upper limit from the likelihood fit is shown on the x-axis (with the corresponding total uncertainty represented by horizontal lines).

triggers 4. A cut was chosen to be applied on the p_T (NL Lepton) slightly tighter than the tightest single lepton p_T cut in the trigger. The p_T (NL Lepton) cut can be optimized by comparing the expected significance and limit for a range of p_T (NL Lepton) cuts to determine the cut which maximizes sensitivity. In Figure 11 the expected significance (Z_μ^{exp}) and expected upper limits ($\mu_{\text{up}}^{\text{exp}}$) for different p_T (NL Lepton) cuts is shown.

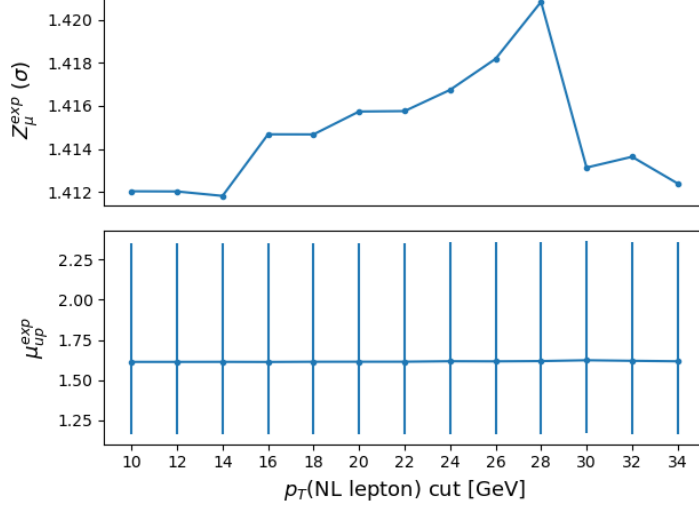


Figure 11: Expected significance (Z_μ^{exp}) and expected upper limit ($\mu_{\text{up}}^{\text{exp}}$) for different p_T (NL Lepton) cuts is shown. The common x-axis shows cut applied to the p_T of the next-to-leading lepton. On the top panel, the expected significance from the likelihood fit is shown on the y-axis. On the bottom panel, the expected upper limit from the likelihood fit is shown on the y-axis (with the corresponding total uncertainty represented by vertical lines).

Since there is a very small change between the different p_T (NL Lepton) cuts on the sensitivity of tWZ , a p_T (NL Lepton) cut is applied at 18 GeV (avoiding a p_T cut near the sharp drop in expected significance after 28 GeV), therefore applying a cut above the tightest, looser dilepton trigger p_T cut (17 GeV) to suppress any systematic from the modelling of the trigger efficiency.

668 4.5 Signal and Control Regions

669 In this section, expected number of events of variables in each region are shown. For each figure in this section, the
 670 data is given by the black points and the MC predictions for each process are given by the filled histograms. The
 671 vertical lines on the data points represent the statistical uncertainty in the data and the diagonally-lined bands
 672 represent the total (statistical and systematic added in quadrature) uncertainty. The lower panel in each plot shows
 673 the ratios of the data to the theoretical predictions. In order to suppress a bias towards large signal observations
 674 in the development of the analysis, data has not been analysed in bins where the expected $\frac{\text{signal}}{\text{background}}$ exceeds 0.1.
 675 This is known as blinding. Blinded bins in the CRs are shaded with black diagonal lines and their data points are
 676 omitted. All data points are omitted in the SRs. In Table 7, the expected number of events for each sample in each
 region are shown. The finite number of events expected to be observed in data (MC simulation) carries an associated

		tWZ OF SR	tWZ SF SR	$t\bar{t}Z$ CR	ZZb CR	$(tWZ)_{\text{fake}}$ CR
$t\bar{t}Z$		13.9 ± 1.8	10.1 ± 1.4	31.7 ± 4.5	5.3 ± 0.7	19.1 ± 2.5
$t\bar{t}Z$ fakes		0.068 ± 0.048	0.032 ± 0.026	0.07 ± 0.04	0.05 ± 0.03	5.0 ± 2.5
tWZ		3.8 ± 0.4	2.6 ± 0.3	2.6 ± 0.9	1.4 ± 0.2	5.0 ± 0.7
ZZ		0.5 ± 0.2	8.8 ± 2.7	1.2 ± 0.4	46 ± 14	7.8 ± 2.4
other	$t\bar{t}$	$6e-06 \pm 3e-06$	0.25 ± 0.44	0.27 ± 0.22	$6e-06 \pm 3e-06$	2.4 ± 0.9
	tZq	0.08 ± 0.04	0.08 ± 0.04	0.06 ± 0.03	0.06 ± 0.02	4.9 ± 0.8
	$t\bar{t}W$	0.007 ± 0.007	0.003 ± 0.003	$6e-06 \pm 3e-06$	0.002 ± 0.006	1.0 ± 0.3
	WZ	0.04 ± 0.02	0.04 ± 0.02	0.013 ± 0.013	0.05 ± 0.03	1.8 ± 0.4
	$t\bar{t}t$	0.0010 ± 0.0008	0.002 ± 0.001	0.014 ± 0.004	$6e-06 \pm 3e-06$	0.010 ± 0.004
	$t\bar{t}t\bar{t}$	0.0093 ± 0.0081	0.011 ± 0.009	0.057 ± 0.021	$6e-06 \pm 3e-06$	0.02 ± 0.01
	$t\bar{t}WW$	0.029 ± 0.026	0.03 ± 0.02	0.26 ± 0.10	0.01 ± 0.03	0.20 ± 0.06
	$VVV (V = W/Z)$	0.28 ± 0.09	0.20 ± 0.06	0.07 ± 0.02	0.20 ± 0.05	0.3 ± 0.1
	$t\bar{t}H$	0.85 ± 0.18	0.67 ± 0.14	2.0 ± 0.4	0.15 ± 0.04	2.2 ± 0.5
Total		19.7 ± 2.0	22.9 ± 3.1	38.4 ± 4.6	53.2 ± 14.0	49.5 ± 4.8
data		-	-	36	49	57

Table 7: The expected number of events for each sample in each region is shown.

677 statistical uncertainty. To first order, this uncertainty can be written as the square root of the expected number
 678 of events to be observed in data. In contrast to this, predictions based on MC simulation carry uncertainties due
 679 to the finite number of simulated events utilised. This uncertainty can be quantified by the Number of Equivalent
 680 Events [47], N_{equiv} , which relates the sample of N events (weighted by MC event weights) to N_{equiv} events with all
 681 MC event weights equal to 1, that would have the same relative statistical fluctuation. The Number of Equivalent
 682 Events, N_{equiv} , can be written as,

$$N_{\text{equiv}} = \frac{(\sum_i^N w_i)^2}{\sum_i^N w_i^2} \quad (4.2)$$

684 where w_i is the MC event weight for event i . The standard uncertainty of N_{equiv} is given by $u(N_{\text{equiv}}) = \sqrt{N_{\text{equiv}}}$.
 685 The Number of Equivalent Events for each sample in each region can be studied in order to ensure that the number
 686 of events simulated for a given process is large in comparison to the number of events expected for that process in
 687 data, thereby ensuring that uncertainties from MC statistics will be small (or sub-leading). In Table 8, the number
 688 of equivalent events, N_{equiv} and its percentage uncertainty ($\frac{u(N_{\text{equiv}})}{N_{\text{equiv}}} \times 100$), is shown for each sample in each region.

tWZ OF SR		tWZ SF SR		$t\bar{t}Z$ CR		ZZb CR		$(tWZ)_{\text{fake}}$ CR		
N_{equiv}	Uncertainty [%]	N_{equiv}	Uncertainty [%]							
tWZ	6463 ± 80	1	4153 ± 64	1.6	4800 ± 69	1.4	2497 ± 50	2	8645 ± 93	1.1
$t\bar{t}Z$	1364 ± 37	2.7	1031 ± 32	3	3237 ± 57	1.8	561 ± 24	4.2	1923 ± 44	2.3
ZZ	51 ± 7	14	975 ± 31	3.2	268 ± 16	6.1	7023 ± 84	1.2	969 ± 31	3.2
other	748 ± 27	3.7	2.5 ± 1.6	64	4.2 ± 2.1	49	255 ± 16	6.3	21.5 ± 4.6	21.6
$t\bar{t}Z$ fakes	6.7 ± 2.6	39	1.3 ± 1.1	87	16.1 ± 4.0	25	7.2 ± 2.7	37	484 ± 22	4.5
Total	8633 ± 93	1.1	6163 ± 79	1.3	8326 ± 91	1.1	10344 ± 102	1	12044 ± 110	1

Table 8: The number of equivalent events, N_{equiv} and its percentage uncertainty ($\frac{u(N_{\text{equiv}})}{N_{\text{equiv}}} \times 100$), is shown for each sample in each region.

689
690
691
692

N_{equiv} is much larger compared to the number of expected events (See Table 7) for the signal and background processes in all regions. This tells us that there is a large number of simulated events for these samples. Therefore ensuring that uncertainties resulting from MC statistics will be small (or sub-leading).

693

4.5.1 tWZ OF SR

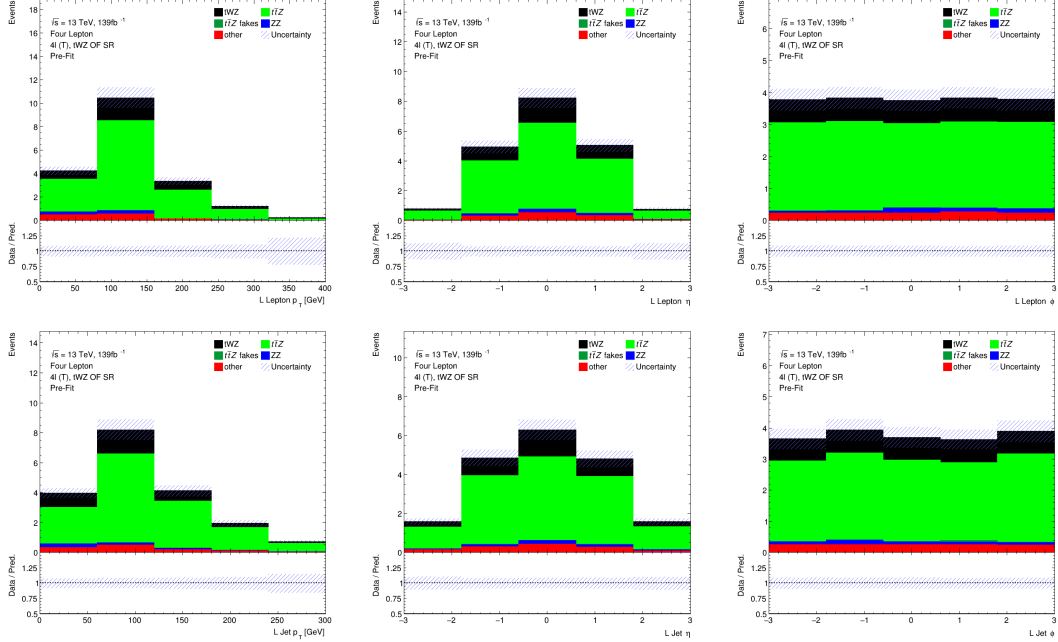
694 In this section, expected number of events of variables in the tWZ OF SR are shown. In Figure 12, comparisons of 695 simulation and data of p_T , η and ϕ for leading (L) leptons and leading (NL) jets in the tWZ OF SR are shown.

Figure 12: Comparisons of simulation and data of p_T , η and ϕ for leading (L) leptons (top row) and leading (NL) jets (bottom row) in the tWZ OF SR are shown.

696 All bins for each plot in Figure 12 have $\frac{signal}{background}$ exceeding 0.1 and are therefore blinded. This region is therefore 697 enriched in tWZ signal events. In Figure 13, comparisons of simulation and data of H_T (scalar sum of Jet p_T), the 698 Number of jets, the scalar sum of b -tagged jet p_T and the number of b -tagged jets in the tWZ OF SR are shown. 699 All bins for each plot in Figure 13 have $\frac{signal}{background}$ exceeding 0.1 and are therefore blinded. This region is therefore 700 enriched in tWZ signal events.
701

4.5.2 tWZ SF SR

702 In this section, expected number of events of variables in the tWZ SF SR are shown. In Figure 14, comparisons of 703 simulation and data of p_T , η and ϕ for leading (L) leptons and leading (NL) jets in the tWZ SF SR are shown.704 All bins for each plot in Figure 14 have $\frac{signal}{background}$ exceeding 0.1 and are therefore blinded. This region is therefore 705 enriched in tWZ signal events. In Figure 15, comparisons of simulation and data of H_T (scalar sum of Jet p_T), the 706 Number of jets, the scalar sum of b -tagged jet p_T and the number of b -tagged jets in the tWZ SF SR are shown.707 The vast majority of bins for each plot in Figure 15 have $\frac{signal}{background}$ exceeding 0.1 and are therefore blinded. This 708 region is therefore enriched in tWZ signal events. The deviations in data and simulation in the two bins (in the 709 HT and σb jet p_T distributions) which are not blinded, are within the expected uncertainties.
710

4.5.3 $t\bar{Z}$ CR

711 In this section, expected number of events of variables in the $t\bar{Z}$ CR are shown. In Figure 16, comparisons of 712 simulation and data of p_T , η and ϕ for leading (L) leptons and leading (NL) jets in the $t\bar{Z}$ CR are shown.

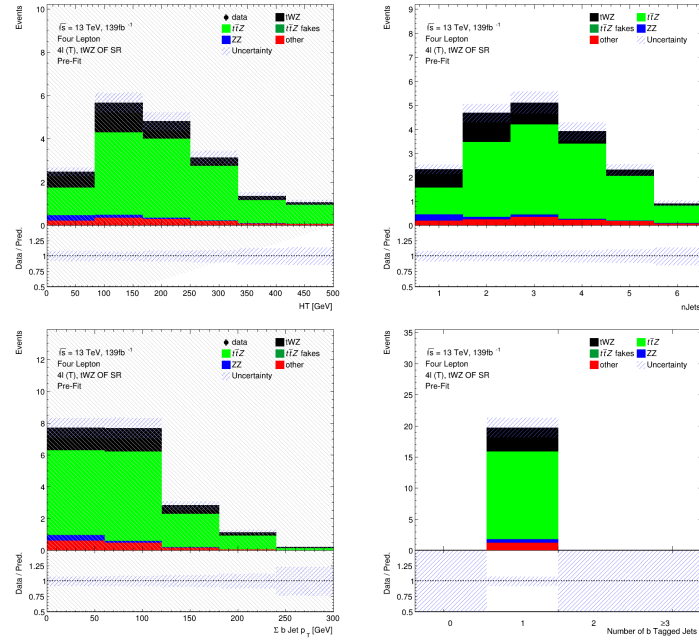


Figure 13: Comparisons of simulation and data of H_T (scalar sum of Jet p_T), the Number of jets, the scalar sum of b -tagged jet p_T and the number of b -tagged jets (top left to bottom right) in the tWZ OF SR are shown.

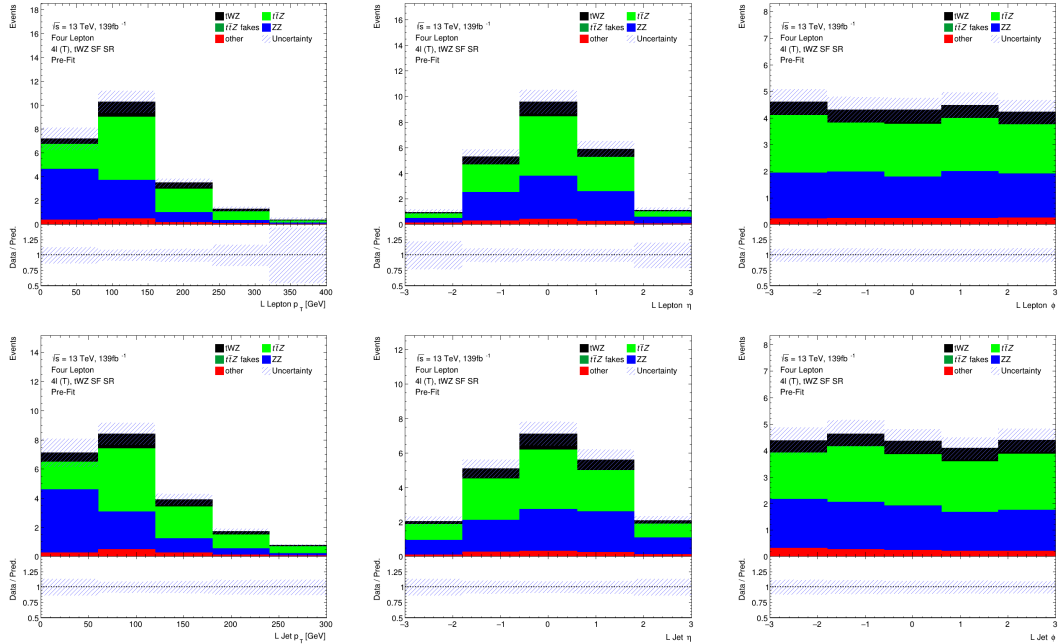


Figure 14: Comparisons of simulation and data of p_T , η and ϕ for leading (L) leptons (top row) and leading (NL) jets (bottom row) in the tWZ SF SR are shown.

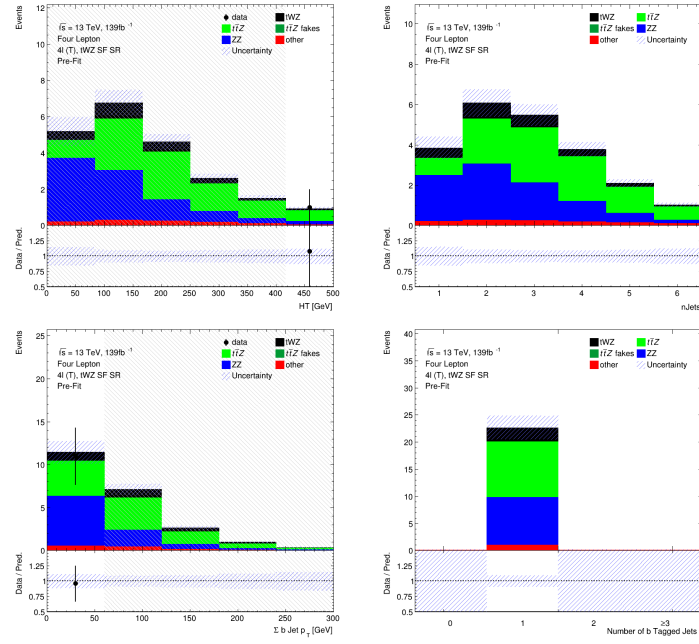


Figure 15: Comparisons of simulation and data of H_T (scalar sum of Jet p_T), the Number of jets, the scalar sum of b -tagged jet p_T and the number of b -tagged jets (top left to bottom right) in the tWZ SF SR are shown.

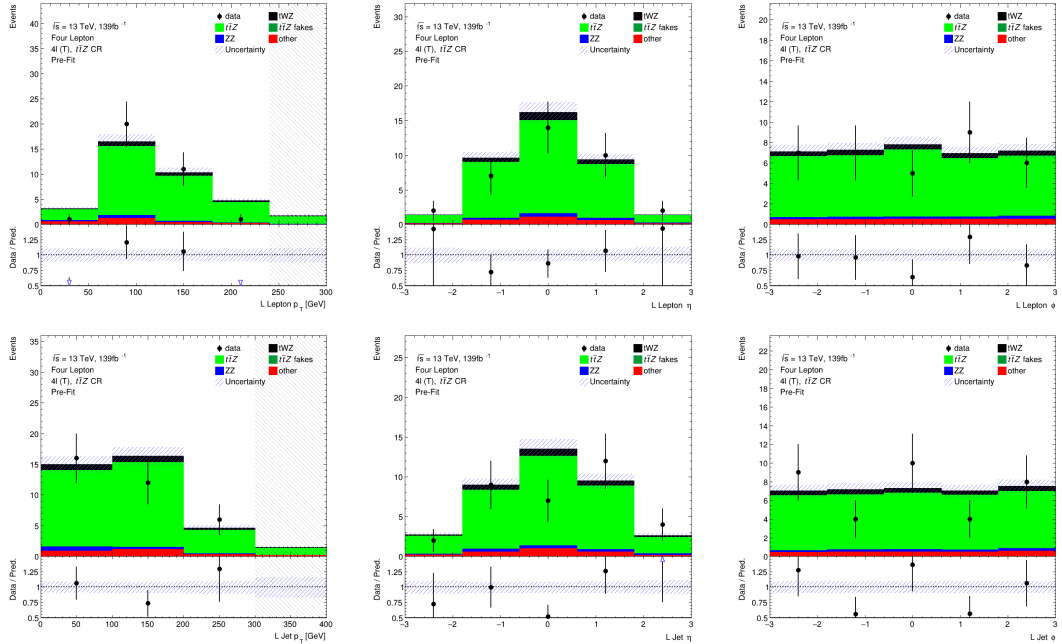


Figure 16: Comparisons of simulation and data of p_T , η and ϕ for leading (L) leptons (top row) and leading (NL) jets (bottom row) in the $t\bar{t}Z$ CR are shown.

713 The majority of the deviations in data and simulation for each plot in Figure 16 are within the expected uncertainties.
 714 The few plots which have bins where there is a disagreement between data and simulation are either within 2σ
 715 (L Jet ϕ) or 3σ (L Jet η) standard uncertainties from one another, or are show more than a 3σ (L Lepton p_T)
 716 disagreement. The disagreement in the L Lepton p_T distribution could be due to statistical fluctuations in data
 717 or simulation, since there are so few events in these bins. In Figure 17, comparisons of simulation and data of H_T
 718 (scalar sum of Jet p_T), the Number of jets, the scalar sum of b -tagged jet p_T and the number of b -tagged jets in the
 719 $t\bar{t}Z$ CR are shown.

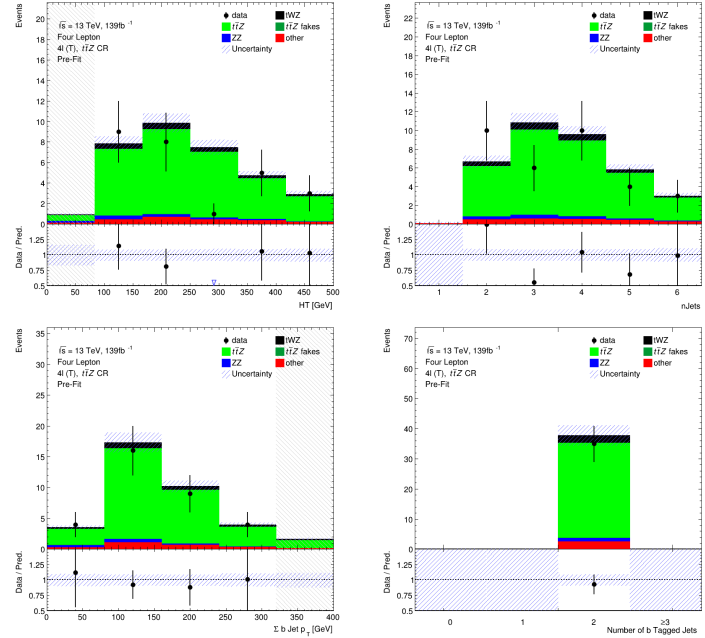


Figure 17: Comparisons of simulation and data of H_T (scalar sum of Jet p_T), the Number of jets, the scalar sum of b -tagged jet p_T and the number of b -tagged jets (top left to bottom right) in the $t\bar{t}Z$ CR are shown.

720 Almost all of the deviations in data and simulation for each plot in Figure 17 are within the expected uncertainties.
 721 There is a 2σ disagreement in one of the bins in the $nJets$ distribution and a large disagreement ($> 5\sigma$) in one
 722 of the bins in the HT distribution. The large disagreement between data and simulation in the HT distribution
 723 is surprising since all other bins in the distribution agree within 1σ uncertainties, and it is therefore not fully
 724 understood.

725 4.5.4 ZZb CR

726 In this section, expected number of events of variables in the ZZb CR are shown. In Figure 18, comparisons of
 727 simulation and data of p_T , η and ϕ for leading (L) leptons and leading (NL) jets in the ZZb CR are shown.
 728 Most of the deviations in data and simulation for each plot in Figure 18 are within the expected uncertainties.
 729 There are a few bins with 2σ and $> 2\sigma$ disagreements between data and simulation in the L Lepton p_T , L Lepton η
 730 and L Jet p_T distributions, with the disagreement being much more noticeable in the L Lepton distributions. This
 731 could suggest some mis-modelling for L Leptons in this region. In Figure 19, comparisons of simulation and data of
 732 H_T (scalar sum of Jet p_T), the Number of jets, the scalar sum of b -tagged jet p_T and the number of b -tagged jets
 733 in the ZZb CR are shown.

734 Most of the deviations in data and simulation for each plot in Figure 18 are within the expected uncertainties.

735 4.5.5 $(tWZ)_{\text{fake}}$ CR

736 In this section, expected number of events of variables in the $(tWZ)_{\text{fake}}$ CR are shown. In Figure 20, comparisons
 737 of simulation and data of p_T , η and ϕ for leading (L) leptons and leading (NL) jets in the $(tWZ)_{\text{fake}}$ CR are shown.
 738 The vast majority of bins for each plot in Figure 20 have $\frac{\text{signal}}{\text{background}}$ exceeding 0.1 and are therefore blinded. This
 739 region is therefore enriched in tWZ signal events. Most deviations in data and simulation in the bins which are
 740 not blinded, are within the expected uncertainties. Only two out of seven unblinded bins are not within expected

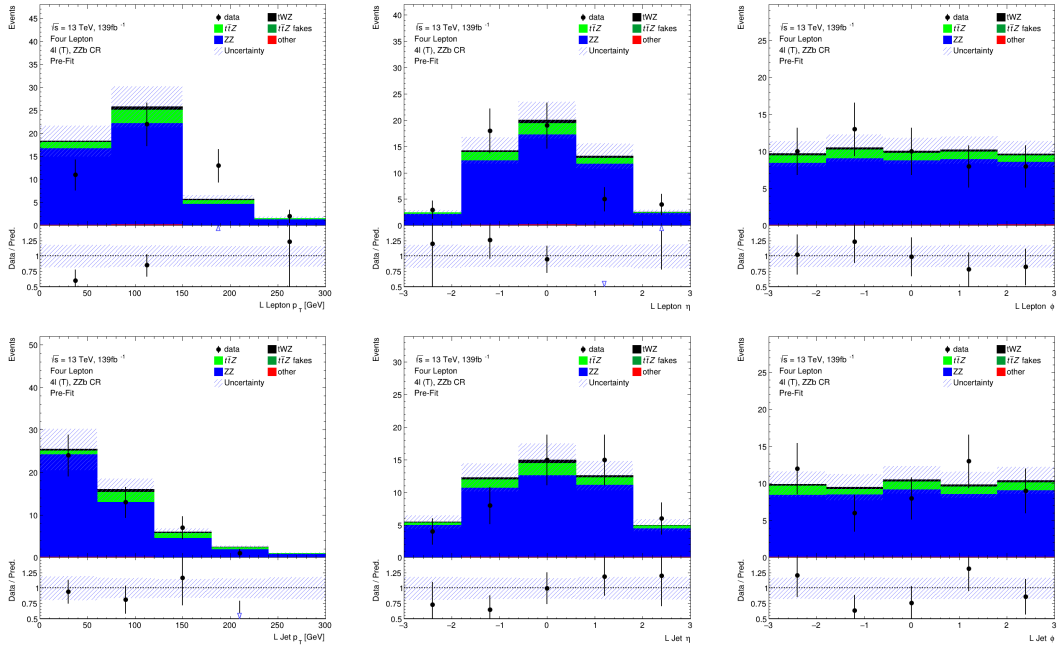


Figure 18: Comparisons of simulation and data of p_T , η and ϕ for leading (L) leptons (top row) and leading (NL) jets (bottom row) in the ZZb CR are shown.

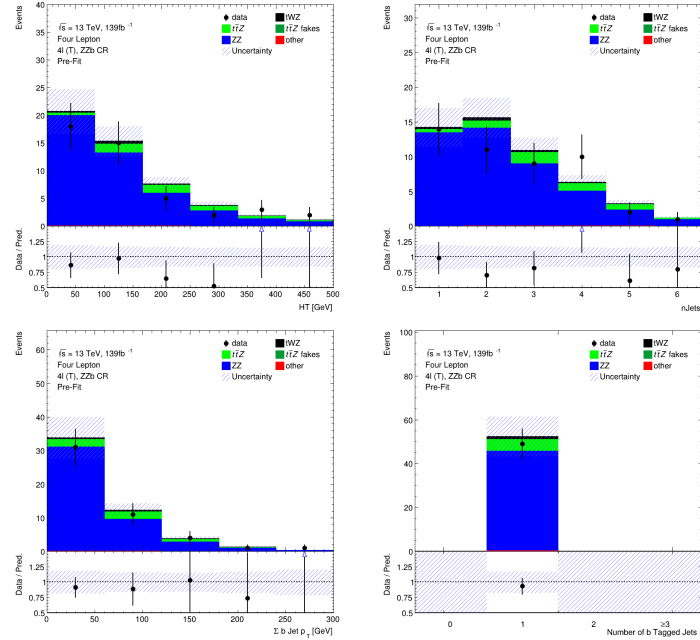


Figure 19: Comparisons of simulation and data of H_T (scalar sum of Jet p_T), the Number of jets, the scalar sum of b -tagged jet p_T and the number of b -tagged jets (top left to bottom right) in the ZZb CR are shown.

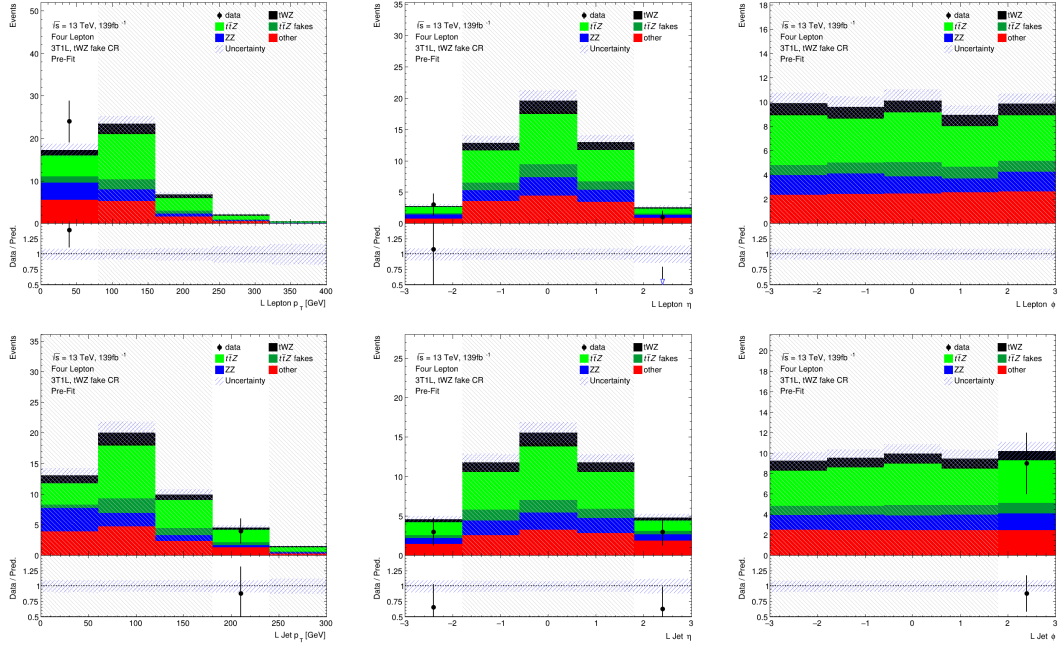


Figure 20: Comparisons of simulation and data of p_T , η and ϕ for leading (L) leptons (top row) and leading (NL) jets (bottom row) in the $(tWZ)_{\text{fake}}$ CR are shown.

uncertainties and are within a 2σ uncertainty. In Figure 21, comparisons of simulation and data of H_T (scalar sum of Jet p_T), the Number of jets, the scalar sum of b -tagged jet p_T and the number of b -tagged jets in the $(tWZ)_{\text{fake}}$ CR are shown.

The majority of bins for each plot in Figure 21 have $\frac{\text{signal}}{\text{background}}$ exceeding 0.1 and are therefore blinded. This region is therefore enriched in tWZ signal events. Most deviations in data and simulation in the bins which are not blinded, are within the expected uncertainties. Only two out of seven unblinded bins are not within expected uncertainties and are within a 2σ uncertainty.

4.6 Fake Lepton Estimation

Fake leptons are physics objects reconstructed as leptons, but do not correspond to the leptons which originate from the hard scatter process or those physics objects that are mis-identified as leptons. The sources of fake leptons include those originating from heavy hadron decays, light hadron decays or via the conversion of a photon to a lepton. In the ATLAS detector, the probability for a fake to occur is very low. In this section, the method used to estimate the fake lepton contribution is described.

As $t\bar{t}Z$ is the dominant background process ($\sim 75\%$ of the total background contribution), it is assumed that $t\bar{t}Z$ will also dominate the events containing fake leptons. The fake lepton efficiency, ϵ , can be written as $\epsilon = \frac{N_{\text{fake}}^{\text{tight}}}{N_{\text{fake}}^{\text{loose}}}$, where $N_{\text{fake}}^{\text{tight}}$ is the number of fake leptons which pass the tight lepton selection (See Section 4.2.1) and $N_{\text{fake}}^{\text{loose}}$ is the number of fake leptons which pass the loose lepton selection (See Section 4.2.1). The probability of one fake lepton to occur, $P(\text{one fake } \ell)$, is proportional to $\epsilon_1 \ll 1$ [65, 82] and the probability for two fakes to occur is, $P(\text{two fakes } \ell)$, is proportional to $\epsilon_2 < \epsilon_1 \ll 1$. In this analysis, an estimation of the fake lepton component to the highest order is investigated and therefore the case where at least one fake lepton occurs in a $t\bar{t}Z$ event is considered.

Firstly, the dominant $t\bar{t}Z$ background is split up into $t\bar{t}Z$ and $(t\bar{t}Z)_{\text{fake}}$ components. Secondly, a $(tWZ)_{\text{fake}}$ CR (See Section 4.4) is defined which is enhanced in fakes and aims to constrain the $(t\bar{t}Z)_{\text{fake}}$ background in the SR. All events which contribute to the $(t\bar{t}Z)_{\text{fake}}$ background are determined by the IFF Truth Classifier [59]. The IFF Truth Classifier is a tool which aims to classify leptons based off their truth information. It uses the more general MCTruthClassifier [70] tool's output as input and returns one of the following lepton categories: Unknown, KnownUnknown (leptons which can (in principle) be classified, but the MCTruthClassifier fails to classify the

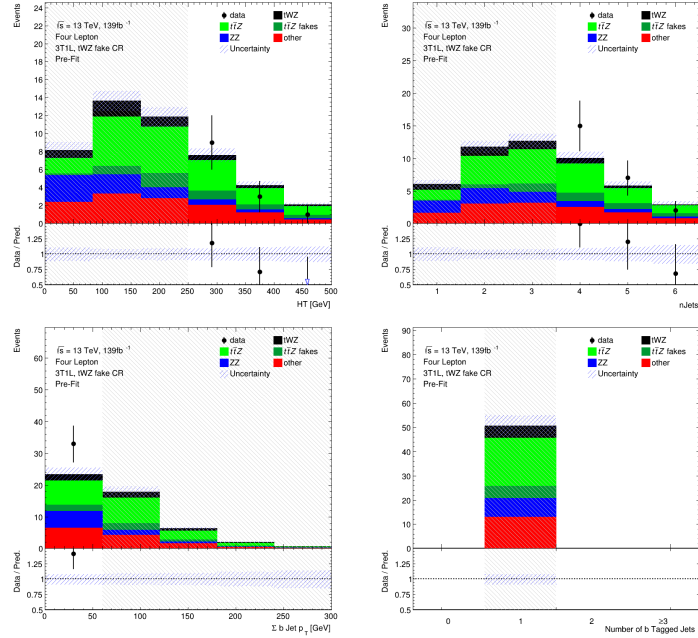


Figure 21: Comparisons of simulation and data of H_T (scalar sum of Jet p_T), the Number of jets, the scalar sum of b -tagged jet p_T and the number of b -tagged jets (top left to bottom right) in the $(tWZ)_{\text{fake}}$ CR are shown.

lepton's truth type or origin), IsoElectron, ChargeFlipIsoElectron, PromptMuon, PromptPhotonConversion, ElectronFromMuon, TauDecay, BHadronDecay, CHadronDecay or LightFlavorDecay (More details [60]). Given these categories, leptons are considered as fake if they are classified as PromptPhotonConversion, BHadronDecay, CHadronDecay or LightFlavorDecay (i.e. a lepton originating from the decay of a b -Hadron, c -Hadron or light-flavour jet). Events which contribute to the $(t\bar{t}Z)_{\text{fake}}$ background are those where at least one lepton from the $t\bar{t}Z$ sample are classified by the IFF Truth Classifier with one of the four aforementioned categories.

The $(tWZ)_{\text{fake}}$ CR aims to be as similar as possible to the tWZ SRs, but enhanced in fakes. This CR can then be used to constrain the normalisation of the $(t\bar{t}Z)_{\text{fake}}$ template. To ensure that this region is enhanced in fakes, it is required that it contains 3 tight leptons and 1 loose lepton, since loose leptons are more likely to be fakes. Leptons from heavy decays are produced in jets and are typically surrounded by other energetic particles. Since the loose lepton definition relaxes the isolation requirement, leptons satisfying the loose criteria are more enhanced in these fake leptons. By using the p_T of the loose lepton ($p_T(\text{Loose Lepton})$) in this region as the variable used in the fit, the shape (and normalisation) of the $(t\bar{t}Z)_{\text{fake}}$ template can be constrained. In Figure 22, the number of leptons classified as fake and the relative dominance of the different classifications for fake leptons, split up by their IFF Truth classification, in each region are shown.

The plot on the left illustrates that there is a large amount of fake leptons which pass our selection criteria for the $(tWZ)_{\text{fake}}$ CR, compared to remaining four regions. Therefore there is a significant amount of fake leptons present in the $(tWZ)_{\text{fake}}$ CR which allow the fake lepton component to be sufficiently constrained. The plot on the right illustrates that the majority of fake leptons which pass our selection criteria originate from the decay of b -hadrons, in all regions but the $t\bar{t}Z$ CR. The smaller proportion of fake leptons originating from b -hadron decays in the $t\bar{t}Z$ CR could possibly be due to statistical fluctuations resulting from the low number of fake leptons which pass our selection criteria in this region (~ 40 fake leptons). In Figure 23, the amount of fake and real $t\bar{t}Z$ events which pass our selection criteria, in each region, is shown.

Around 20% of all $t\bar{t}Z$ events are classified as fake events (having one or more of its leptons being classified as fake) in the $(tWZ)_{\text{fake}}$ CR. The tWZ OF SR, tWZ SF SR, $t\bar{t}Z$ CR and ZZb CR have less than 1% of their total $t\bar{t}Z$ events being fake. The significant fraction of fake $t\bar{t}Z$ events present in the $(tWZ)_{\text{fake}}$ CR allows the $t\bar{t}Z$ fake background to be sufficiently constrained by the $(tWZ)_{\text{fake}}$ CR.

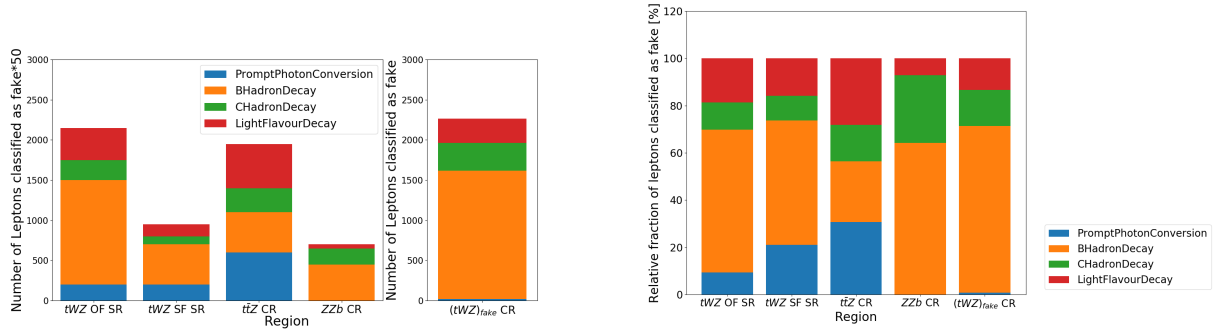


Figure 22: **Left:** The number of leptons classified as fake, split up by their IFF Truth classification, in each region is shown. The left panel shows the number of leptons classified as fakes, scaled by a factor of 50, on the y-axis. The right panel shows the number of leptons classified as fakes (unscaled), on the y-axis. The different signal and control regions are shown on the x-axes of the left and right panels. The IFF truth classification of the leptons are shown in the legend and correspond to the different coloured stacked histograms. **Right:** The relative dominance of the different classifications for fake leptons (classified by the IFF truth classified) in each region, is shown. The relative dominance of leptons classified as fakes, as a fraction of the total number of fake leptons (in each region), is shown on the y-axis. The different signal and control regions are shown on the x-axis. The IFF truth classification of the leptons are shown in the legend and correspond to the different coloured stacked histograms.

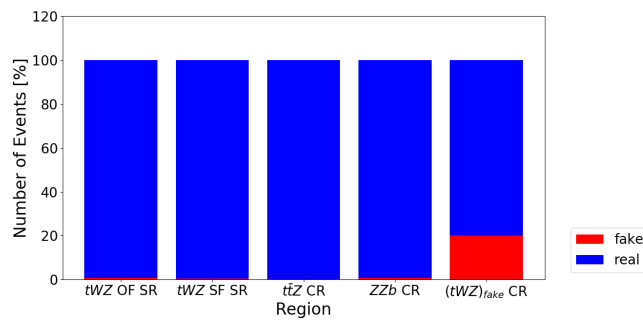


Figure 23: The percentage of fake and real $t\bar{Z}$ events which pass our selection criteria, in each region, is shown. The relative number of fake and real events (in % of the total number of events in the nominal and fake $t\bar{Z}$ background samples) is shown on the y-axis. The different signal and control regions are shown on the x-axis. The blue and red histograms represent the percentage of real and fake events (out of the total number of events in the nominal and fake $t\bar{Z}$ background samples), respectively.

4.7 Improving signal vs background discrimination

The presence of different numbers of top quarks is a key discriminator between signal and the dominant background process, $t\bar{t}Z$. This information is aimed to be exploited by reconstructing ℓb systems as a proxy for top quarks (since, $t \rightarrow W(\rightarrow \ell\nu)b$). This is done in two ways, firstly, by implementation of a kinematic reconstruction algorithm (Two Neutrino Scanning Method) which aims to determine the likelihood of an event containing two top quarks and secondly, by implementing a Boosted Decision Tree (BDT) which is used to classify ℓb systems originating from top quarks. In this thesis, this BDT is referred to as an *object-level* BDT. Certain variables constructed from event information show discrimination between signal and background events. This information can be exploited to discriminate between signal and background events by constructing a model which takes advantage of these discriminating variables. A BDT is implemented and is used to discriminate between tWZ events and its major backgrounds, $t\bar{t}Z$ and ZZ . Furthermore, this BDT takes information from the kinematic reconstruction algorithm and the object-level BDT in order to maximize its discriminating power. In this thesis, this BDT is referred to as an *event-level* BDT. The discriminator output from the object-level BDT can be converted to a variable which can then be used as an input to the event-level BDT.

4.7.1 Two Neutrino Scanning Method (2ν SM) Algorithm

The difference in the number of resonant top quarks in the tWZ signal and the dominant background, $t\bar{t}Z$, is a key feature which can be exploited in order to discriminate between these two processes. In Section 4.7.3, a BDT was implemented which exploits this information by aiming to identify ℓb systems originating from top quarks. In this section, a kinematic reconstruction algorithm (Two Neutrino Scanning Method) is implemented which exploits the same feature. The Two Neutrino Scanning Method (2ν SM) algorithm¹ [69, 68] aims to reconstruct $t\bar{t}$ systems in the 2ℓ , 3ℓ and 4ℓ final states (e.g. 2ℓ case: $t\bar{t} \rightarrow \ell^+\nu_\ell b\bar{b} - \bar{\nu}_\ell \bar{b}$). The 2ν SM algorithm aims to reconstruct a $t\bar{t}$ system by finding two neutrinos (ν_1 and ν_2) which are most likely to correspond to the neutrinos that originate from the decay of a $t\bar{t}$ system. This algorithm can be used in our analysis to discriminate between tWZ and $t\bar{t}Z$, since the OSSF leptons which decay from the Z boson can be easily reconstructed and removed before inputting the event into the algorithm. The removal of the Z boson results in tWZ events that don't resemble $t\bar{t}$ systems and $t\bar{t}Z$ events that do resemble $t\bar{t}$ systems, which the algorithm is designed to distinguish between. It would then be expected that the 2ν SM algorithm returns a higher score from a $t\bar{t}Z$ event (~ 1 , i.e. it looks like a $t\bar{t}$ event after removal of the Z boson) and a lower score from a tWZ event (~ 0 , i.e. it does not look like a $t\bar{t}$ event after removal of the Z boson). The first step in the 2ν SM algorithm involves stating four equations which correspond to the invariant masses of the top quark ($m(t)$) and W boson ($m(W)$) for the two top quark decays (i.e. $t \rightarrow W^+b \rightarrow \ell^+\nu_\ell$) in a dileptonic $t\bar{t}$ event. These can be written as,

$$(\ell_1 + \nu_1)^2 = m(W)^2 = (80.385 \text{ GeV})^2 \quad (4.3)$$

$$(\ell_1 + \nu_1 + b_{1,2})^2 = m(t)^2 = (172.5 \text{ GeV})^2 \quad (4.4)$$

$$(\ell_2 + \nu_2)^2 = m(W)^2 = (80.385 \text{ GeV})^2 \quad (4.5)$$

$$(\ell_2 + \nu_2 + b_{2,1})^2 = m(t)^2 = (172.5 \text{ GeV})^2 \quad (4.6)$$

where the subscripts indicate that these particles originate from the decay of two different top quarks in a $t\bar{t}$ system. An assumption is made such that the mass of the neutrinos (ν_1 and ν_2) are exactly zero, which leaves us with 6 unknowns, p_{T,ν_1} , ϕ_{ν_1} , η_{ν_1} , p_{T,ν_2} , ϕ_{ν_2} and η_{ν_2} (components of the two neutrino's 4-vectors). The 4-vectors of the two reconstructed leptons (not from the Z boson) and the two jets with the highest DL1r b -tagger score are used as input to the algorithm. For each neutrino (ν_1 and ν_2), a scan over a range of possible η and ϕ values is performed. These values were chosen to be $\phi_{\nu_1}, \phi_{\nu_2} \in [-\pi, \pi]$ with a step size of ≈ 0.25 and $\eta_{\nu_1}, \eta_{\nu_2} \in [-5, 5]$ with a step size of ≈ 0.31 . These ranges were chosen to maximize accuracy and minimize computation time. For each of these possible η and ϕ values, the corresponding p_T for each neutrino is calculated (p_{T,ν_1} and p_{T,ν_2}) via,

$$p_{T,\nu} = \frac{\frac{1}{2}(m(W)^2 - m(\ell)^2)}{E_\ell \cosh \eta_\nu - p_{\ell,z} \sinh \eta_\nu - p_{\ell,x} \cos \phi_\nu - p_{\ell,y} \sin \phi_\nu} \quad (4.7)$$

where E_ℓ is the energy of the lepton, $m(\ell)$ is the invariant mass of the lepton and $p_{\ell,z}, p_{\ell,x}, p_{\ell,y}$ are the z , x and y components of lepton's momentum. After computing $p_{T,\nu}$ for both neutrinos for each possible η and ϕ combination

¹software tool and weights provided by Thomas McCarthy ($t\bar{t}Z$ analysis group - Max Planck Institute)

838 in the defined ranges, a collection of possible 4-vectors for ν_1 and ν_2 can be reconstructed. Using ν_1 and ν_2 , two
839 possible $t\bar{t}$ systems are reconstructed,

$$t_1 = \ell_1 + b_1 + \nu_1 \text{ and } t_2 = \ell_2 + b_2 + \nu_2 \quad (4.8)$$

OR

$$t_1 = \ell_1 + b_2 + \nu_1 \text{ and } t_2 = \ell_2 + b_1 + \nu_2 \quad (4.9)$$

840 The 2ν SM algorithm is extremely computationally intensive. The computation time depends on the number step
841 size of the ϕ and η ranges which are scanned over to reconstruct the neutrinos. For example, consider the step sizes
842 chosen in this analysis, $\Delta\eta \approx 0.31$ and $\Delta\phi \approx 0.25$ which corresponds to 32 values for η and 25 values for ϕ . There
843 will be $(32)(32)(25)(25) = 640\,000$ possible pairs of neutrinos (ν_1 and ν_2) to consider per event. Since two possible
844 $t\bar{t}$ systems (See Equations 4.8 and 4.9) are considered, this number effectively increases to $(2)(640\,000) = 128\,000$
845 0 iterations per event. In order to reduce the number of $t\bar{t}$ systems needed to be considered, therefore decreasing
846 computation time, distributions of variables from $t\bar{t}$ events are studied to apply a veto to a possible reconstructed $t\bar{t}$
847 system if the variable in question is improbable or unlikely to be observed in a $t\bar{t}$ event. To achieve this, an allowed
848 range is defined for these variables (See Figure 25 and Figure 26), and if the possible reconstructed $t\bar{t}$ system's
849 corresponding value for this variable lies outside this range, it is vetoed and the algorithm continues with the next
850 iteration. The first variable which is considered, is the difference between average mass of the two possible ℓb system
851 combinations, $\Delta\langle m(\ell b) \rangle$. The two possible ℓb system combinations are,

$$(\ell_1 b_1) = \ell_1 + b_1 \text{ and } (\ell_2 b_2) = \ell_2 + b_2 \quad (4.10)$$

OR

$$(\ell_1 b_2) = \ell_1 + b_2 \text{ and } (\ell_2 b_1) = \ell_2 + b_1 \quad (4.11)$$

852 $\Delta\langle m(\ell b) \rangle$ is therefore defined as,

$$\Delta\langle m(\ell b) \rangle = \frac{1}{2} |[(m(\ell_1 b_1) + m(\ell_2 b_2)) - (m(\ell_1 b_2) + m(\ell_2 b_1))]| \quad (4.12)$$

853 The idea here is that, in events where the average masses of the two possible ℓb system combinations differ greatly,
854 the correct combination is usually given by the combination with the smaller average mass. Furthermore, it
855 was shown in Ref. [69] that reconstructed top quarks in a $t\bar{t}$ system that contain b -tagged jets in opposite hemi-
856 spheres² ($\eta(b_1) \times \eta(b_2) < 0$) of the ATLAS detector are easier to determine the correct ℓb system combination
857 than reconstructed $t\bar{t}$ systems that contain b -tagged jets in the same hemispheres ($\eta(b_1) \times \eta(b_2)$). To illustrate this,
858 the distributions (constructed from $t\bar{t}$ events) of the probability of choosing the correct ℓb system combination,
859 given that the one with the minimum $\langle m(\ell b) \rangle$ chosen ($P(\text{Correct combination of } \ell b \text{ systems} | \text{minimum}(\langle m(\ell b) \rangle))$)
860 vs $\Delta\langle m(\ell b) \rangle$ for b -tagged jets in the same and opposite hemispheres are investigated. In Figure 24, the
861 $P(\text{Correct combination of } \ell b \text{ systems} | \text{minimum}(\langle m(\ell b) \rangle))$ vs $\Delta\langle m(\ell b) \rangle$, for b -tagged jets in the same and opposite
862 hemispheres, constructed from $t\bar{t}$ events is shown.
863 From Figure 24, for both cases where the b -tagged jets are in the same and opposite hemispheres, the proba-
864 bility for a correct ℓb system being chosen, given that the ℓb system with the minimum average mass is under
865 consideration, is an increasing function which plateaus to 1 at ~ 90 GeV. One of these two distributions are
866 used (depending on whether or not the two b -tagged jets are in the same or opposite hemispheres) to interpolate
867 the $P(\text{Correct combination of } \ell b \text{ systems} | \text{minimum}(\langle m(\ell b) \rangle))$ from $\Delta\langle m(\ell b) \rangle$. A veto is applied to the ℓb combi-
868 nation with the maximum $\Delta\langle m(\ell b) \rangle$ if $P(\text{Correct combination of } \ell b \text{ systems} | \text{minimum}(\langle m(\ell b) \rangle)) > 0.8$, indicating that
869 there is at least an 80% certainty that the ℓb combination with the minimum $\langle m(\ell b) \rangle$ is the correct combination.
870 If $P(\text{Correct combination of } \ell b \text{ systems} | \text{minimum}(\langle m(\ell b) \rangle)) < 0.8$, both possible ℓb system combinations need to be
871 considered. The η of the $b\bar{b}\ell\ell$ system, $\eta(b\bar{b}\ell\ell)$, to veto improbable $\eta(\nu_1)$ and $\eta(\nu_2)$ values is then considered. In the
872 same way as for $\Delta\langle m(\ell b) \rangle$, a distribution is generated to determine values $\eta(\nu)$ which are improbable for a $t\bar{t}$ event.
873 In this case, a 2D histogram from simulated $t\bar{t}$ events (dileptonic final state) at generator-level of $\eta(\nu)$ vs $\eta(b\bar{b}\ell\ell)$
874 is generated. Using this histogram, a veto region (where a $t\bar{t}$ event is extremely unlikely to occur) is defined which
875 contains 95% of events. A veto is applied if either possible neutrino lies within this region. In Figure 25, a heatmap
876 of occupancy for $\eta(\nu)$ vs $\eta(b\bar{b}\ell\ell)$ (produced from simulated $t\bar{t}$ events) and its corresponding veto region are shown.
877 The final kinematic constraint which is considered is the scalar sum of lepton p_T , $L_T = p_T(\ell_1) + p_T(\ell_2)$, which
878 is used to veto certain possible neutrinos, ν_1 and ν_2 . Again, a distribution is generated to determine (and veto)

²The ATLAS detector can be split into two regions or *hemispheres*, defined where $z > 0$ and $z < 0$

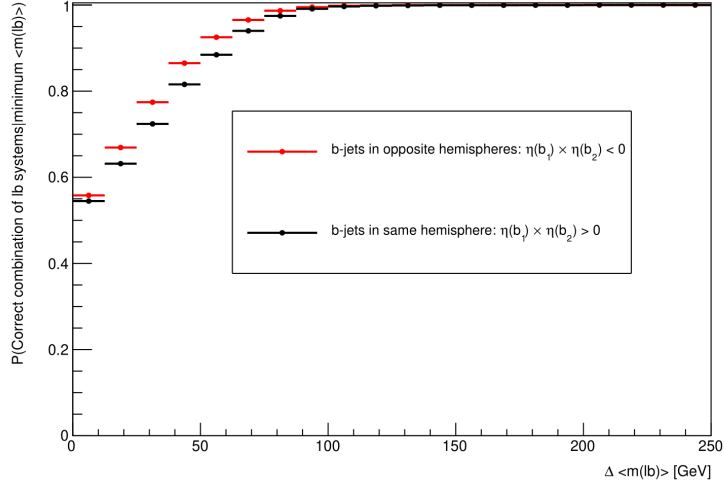


Figure 24: $P(\text{Correct combination of } \ell b \text{ systems} | \text{minimum}\langle m(\ell b) \rangle)$ vs $\Delta\langle m(\ell b) \rangle$, for b -tagged jets in the same and opposite hemispheres, constructed from $t\bar{t}$ events is shown. The horizontal red lines represent the distribution in the case when the two b -jets are in opposite hemispheres. The dot in the middle of the line represents the midpoint of the line. The horizontal black lines represent the distribution in the case when the two b -jets are in the same hemispheres. The dot in the middle of the line represents the midpoint of the line. The average $m(\ell b)$ is shown on the x-axis. The $P(\text{Correct combination of } \ell b \text{ systems} | \text{minimum}\langle m(\ell b) \rangle)$ is shown on the y-axis.

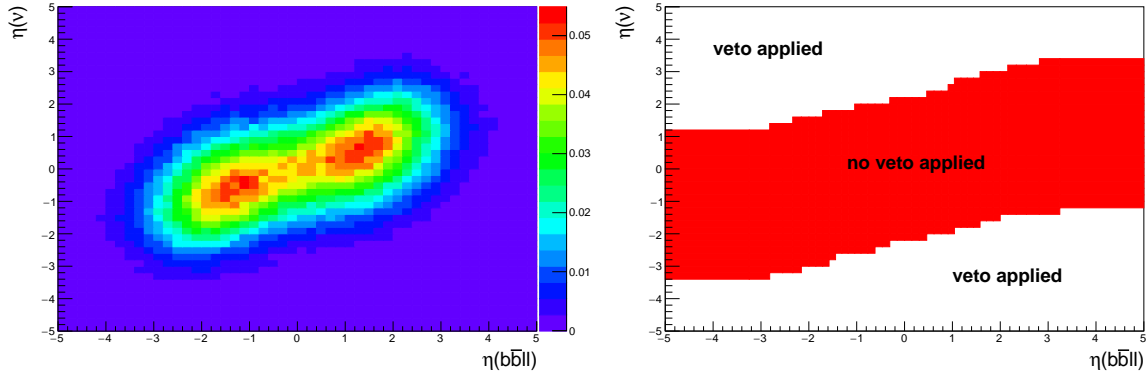


Figure 25: **Left:** Heatmap of occupancy for $\eta(\nu)$ vs $\eta(b\bar{b}\ell\ell)$ produced from simulated $t\bar{t}$ events (dileptonic final state) at generator-level is shown. η of the $b\bar{b}\ell\ell$ system is shown on the x-axis. η of the neutrino is shown on the y-axis. The colourbar on the right represents the fraction of events in the phase space. **Right:** The regions where vetoes are applied for the $\eta(b_1 b_2 \ell_1 \ell_2)$ constraint is shown. η of the $b\bar{b}\ell\ell$ system is shown on the x-axis. η of the neutrino is shown on the y-axis. The red band shows the region where the neutrino would not be vetoed. The white areas (above and below the red band) are regions where the neutrino is vetoed.

improbable possible neutrinos in simulated $t\bar{t}$ events (dilepton final state). Using the same method as described for Figure 25, a veto region is defined where a veto is applied if either possible neutrino lies within this region. In Figure 26, a heatmap of occupancy for $\Delta R(\ell, \nu)$ vs L_T (produced from simulated $t\bar{t}$ events) and its corresponding veto region are shown.

In order to choose the solution which best represents the two top quarks in a $t\bar{t}$ system, the likelihood of each solution is evaluated in the SM $t\bar{t}$ hypothesis. This is performed using the product of probabilities derived from certain distributions of variables from simulated $t\bar{t}$ events. The events in these distributions are obtained from an ATLAS simulation of generated $t\bar{t}$ events in the dileptonic final state. A normalised distribution of the mass of reconstructed top quarks, $m_{b\ell\nu}$, from a $t\bar{t}$ sample is generated to determine the probabilities $P_{m_{t_1}}$ and $P_{m_{t_2}}$ which correspond to the likelihood of the reconstructed top quarks under the SM $t\bar{t}$ hypothesis. The distribution is

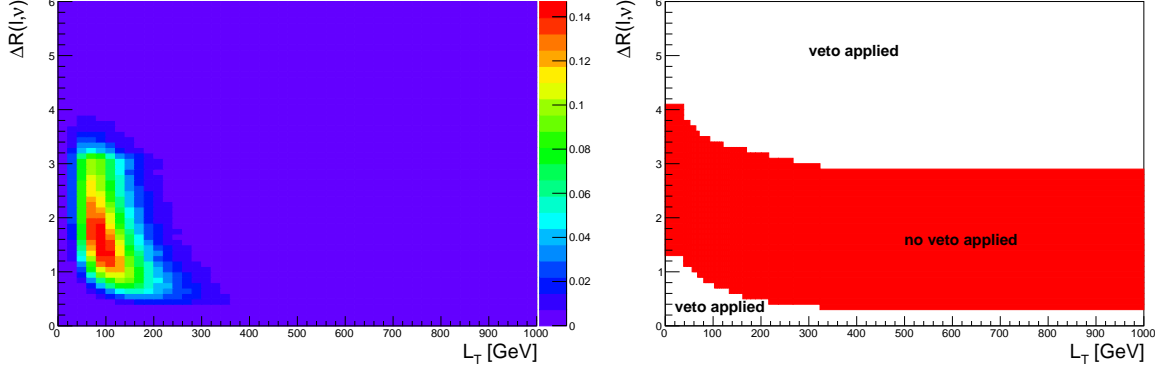


Figure 26: **Left:** A heatmap of occupancy for $\Delta R(\ell, \nu)$ vs L_T produced from simulated $t\bar{t}$ events (dileptonic final state) at generator-level is shown. ΔR between leptons and neutrinos is shown on the x-axis. L_T (scalar sum of lepton p_T) is shown on the y-axis. The colourbar on the right represents the fraction of events in the phase space. **Right:** The regions where vetoes are applied for the L_T constraint is shown. ΔR between leptons and neutrinos is shown on the x-axis. L_T (scalar sum of lepton p_T) is shown on the y-axis. The red band shows the region where the neutrino would not be vetoed. The white areas (above and below the red band) are regions where the neutrino is vetoed.

generated from reco-level leptons, generator-level neutrinos and reco-level jets matched in ΔR to generator-level b -quarks, therefore only filling the distribution with correct detector-level objects. For both reconstructed top quarks, $m(b\ell\nu)$ is calculated and interpolated (i.e. estimate the value of the distribution for some value of the independent variable), via linear interpolation based on the two nearest bin centres, against the $m_{b\ell\nu}$ distribution which returns a weight value from 0 to 1, with higher values corresponding to a reconstructed top quark which has a mass close to that of a top quark from a $t\bar{t}$ system. This interpolation is done for both reconstructed top quarks, t_1 and t_2 , corresponding to probabilities $P_{m_{t_1}}$ and $P_{m_{t_2}}$. A similar method is used to determine $P_{\Delta E_x}$ and $P_{\Delta E_y}$, which corresponds to the likelihood of the reconstructed top quarks under the SM $t\bar{t}$ hypothesis. In this case, a weight distribution of $\Delta E_x = (p_{T,\nu_1})_x + (p_{T,\nu_2})_x - (E_T^{\text{miss}})_x$ based off simulated $t\bar{t}$ events is generated. In particular, this distribution is generated using reco-level E_T^{miss} and generator-level neutrinos. The use of this distribution lies under the assumption that neutrinos are the dominant source of E_T^{miss} , and therefore, $(E_T^{\text{miss}})_x \approx (p_{T,\nu_1})_x + (p_{T,\nu_2})_x$ and $(E_T^{\text{miss}})_y \approx (p_{T,\nu_1})_y + (p_{T,\nu_2})_y$. This distribution is then used to interpolate the value of ΔE_x and ΔE_y from our reconstructed neutrinos. This returns a weight value from 0 to 1, with higher values corresponding to ΔE_x and ΔE_y (and in turn our reconstructed neutrino's p_T) closer to those observed in a $t\bar{t}$ event. It is expected that the ΔE_x and ΔE_y distributions have the same shapes, therefore only one is needed to be generated. In this case the the ΔE_x distribution was chosen. In Figure 27, the $m_{b\ell\nu}$ and ΔE_x distributions (generated from simulated $t\bar{t}$ events) are shown.
A final weight, $w_{2\nu SM} \in [0, 1]$, is then calculated by multiplying the four probabilities ($P_{m_{t_1}}$, $P_{m_{t_2}}$, $P_{\Delta E_x}$ and $P_{\Delta E_y}$) described above. This final weight represents a total probability of the reconstructed top quarks under the SM $t\bar{t}$ hypothesis, and can be written as,

$$w_{2\nu SM} = P_{m_{t_1}} \times P_{m_{t_2}} \times P_{\Delta E_x} \times P_{\Delta E_y} \quad (4.13)$$

The $w_{2\nu SM}$ is calculated for each pair of reconstructed neutrinos (or reconstructed $t\bar{t}$ systems), with the maximum value being chosen as the final value for the event. In Figure 28, a flow chart outlining the steps taken to calculate the $w_{2\nu SM}$ for a event is shown.

4.7.2 Boosted Decision Trees

Machine Learning techniques can be used to build multivariate discriminators (a model that is used to classify data in a dataset) that exploits information from many weak discriminators (those with a small amount of discriminating power) to form one strong discriminator (those with a large amount of discriminating power). A BDT is a Machine Learning technique which classifies data in a dataset into different categories by iteratively applying binary cuts on features of the data (input variables, in the context of this analysis) to segregate the data [101]. The method in which a BDT combines weak discriminators to build a single strong discriminator is called *boosting*. In boosting,

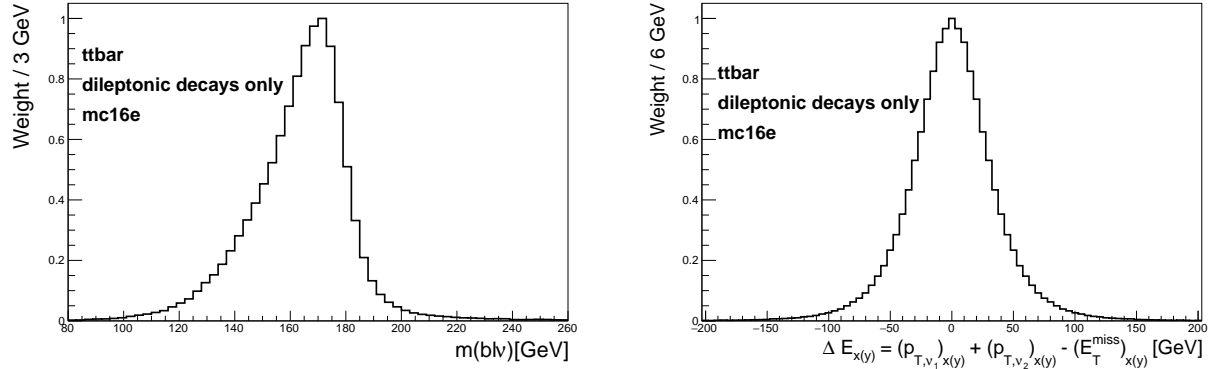


Figure 27: **Left:** $m_{b\ell\nu}$ distribution generated from simulated $t\bar{t}$ events, used to calculate $P_{m_{t_1}}$ and $P_{m_{t_2}}$ is shown. The $m_{b\ell\nu}$ distribution is shown by the black lined histogram. The mass of the $b\ell\nu$ system is shown on the x-axis. The corresponding weight of the $m_{b\ell\nu}$ distribution is shown on the y-axis. **Right:** ΔE_x distribution generated from simulated $t\bar{t}$ events, used to calculate $P_{\Delta E_x}$ and $P_{\Delta E_y}$ is shown. The ΔE_x distribution is shown by the black lined histogram. ΔE_x is shown on the x-axis. The corresponding weight of ΔE_x distribution is shown on the y-axis.

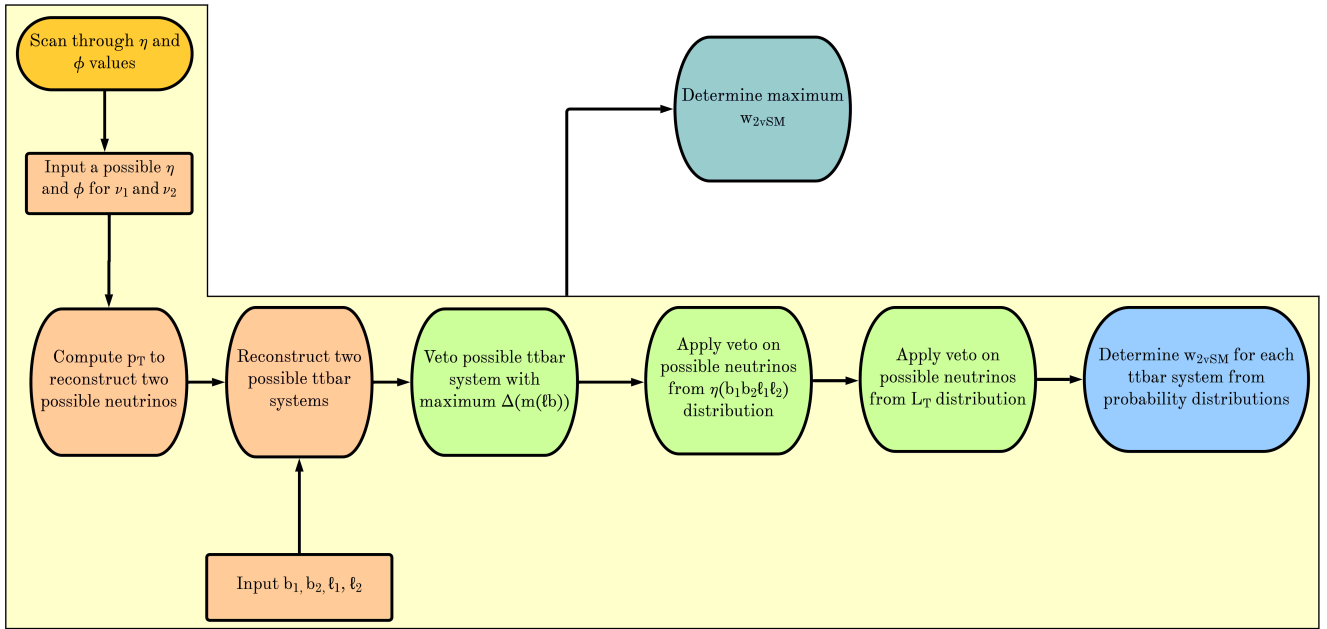


Figure 28: A flow chart outlining the steps taken to calculate the $w_{2\nu SM}$ algorithm is shown.

weak discriminators are sequentially combined, where each classifier iteration is fitted to the difference between the observed and predicted values (residuals) of the training set from the previous step, such that the classifier performance improves [56]. A few concepts related to Machine Learning and BDTs that are used in this analysis, are described briefly in the following text. Performance metrics can be used to evaluate how well a classifier performs in a classification problem [74]. A performance metric used extensively in this analysis is the *accuracy* of a classifier. The accuracy is defined as the percentage of correct predictions for the test dataset (accuracy = $\frac{\text{correct number of predictions}}{\text{total number of predictions}}$). Machine Learning classifiers can be susceptible to learning a training dataset too well, in such a way as to negatively affect its performance on unseen data. This is known as *over-training*. Over-training occurs when noise or random fluctuations in the training dataset are learnt by the classifier [28]. Cross Validation [77] is a procedure used to evaluate a Machine Learning classifier. Cross validation gives an estimate on how the classifier is expected to perform on unseen data and it can be useful tool to protect against over-training. In this analysis we use a type of cross validation called, *k-fold* cross validation. In k-fold cross validation, the training dataset is randomly split up into k subsets, or folds, of approximately equal size. A fold is defined

as a test dataset and the remaining $k-1$ folds are used to train the classifier. The classifier is then evaluated on the test set and a performance metric (or multiple) is evaluated. This procedure is performed once on each fold. Hyper-parameters are user-defined parameters of a classifier that are govern the entire training process. Typical examples of hyper-parameters include the learning rate, the number of discriminators and the type of loss function to be minimised. The learning rate determines the step size at each iteration in determining the minimum of the loss function. Hyper-parameter optimisation is a process which aims to determine the best hyper-parameters for a classifier, based off some performance metric. In this analysis hyper-parameter optimisation is performed using a *grid search*. In a grid search, a user-defined list of hyper-parameter values are chosen for each hyper-parameter that one aims to optimise. The classifier is then trained using each permutation of hyper-parameters and determines the set of hyper-parameters in which the performance metric is maximised. BDTs are chosen to be used in this analysis, since they are not prone to over-training and perform well with minimal optimisation or tweaking of the hyper-parameters. A multi-layered sequential neural network was tried, however, it was out-performed by a BDT. More specifically, Scikit-Learn's `GradientBoostingClassifier` [86] was used.

4.7.3 Object-level BDT

The object-level BDT was trained on an $t\bar{t}$ sample simulated using the same generator, parton shower and to the same order of QCD as the $t\bar{t}$ sample described in Section 4.1.2 but with an orthogonal baseline selection of exactly 1 tight lepton with $p_T > 28$ GeV such that there is no overlap between this sample and the nominal $t\bar{t}$ sample used in the analysis. Additionally, jets in this sample are required to have $p_T > 20$ GeV. Jets are identified as b -tagged jets by the 77% DL1r working point. These baseline selections were chosen to mimic those used in the event selection of the analysis (outlined in Table 6). The leptons and b -jets used for training the object-level BDT are required to pass the aforementioned baseline selections. This $t\bar{t}$ sample was utilised in training the BDT to avoid using a subset of events from the MC samples used in the rest of the analysis, therefore maximizing the amount of generated events available to use in other parts of the analysis. The signal class is defined to consist of reconstructed ℓb systems (defined as the sum of the 4-vectors of a lepton and a b -tagged jet) originating from top quarks which are well matched to their truth counterparts. All possible combinations of ℓ and b -tagged jets are selected from the events. In particular, it is required that ΔR between the reconstructed and truth ℓb system is less than 0.05. An additional requirement is implemented such that the reconstructed lepton and the truth top quark have charges with the same sign (since $t \rightarrow b\ell^+\bar{\nu}_\ell$ and $\bar{t} \rightarrow \bar{b}\ell^-\nu_\ell$). The background class is defined to consist of all reconstructed ℓb systems which fail to pass the criteria for ℓb systems which are labelled as signal. These definitions for the signal and background classes ensure that the signal class consists of mostly ℓb systems originating from top quarks and the background class consists of mostly ℓb systems which do not originate from top quarks. The input variables chosen to be used in the object-level BDT are related to measurable quantities of ℓb systems. The optimum values for the hyper-parameters used were determined via the use of a grid-search (See Section 4.7.2) that determined the set of hyper-parameters which maximized the mean accuracy (based off 5 fold kfold cross-validation). After hyper-parameter optimisation, the mean accuracy of each fold increased from 0.76 to 0.77 ($\sim 1\%$ increase). Input variables can be assigned a score called *variable importance*, based on their usefulness on predicting a target variable (in this case, a signal or background event). The variable importance for any given input variable was obtained by computing the mean accuracy of the classifier, removing the input variable from training, retraining the classifier and computing the mean accuracy of this new classifier. The difference between mean accuracies of the unaltered classifier and the retrained classifier (after removal of the input variable) gives us the variable importance of the given input variable. This method returns positive values for input variables which increase the mean accuracy of the classifier and negative values for input variables which decrease the mean accuracy of the classifier. Input variables with negative variable importances were completely removed from training. In Table 9, the input variables used for training the object-level BDT are shown.

Input Variable	Description	Variable Importance
$m(\ell b)$	Invariant mass of the ℓb system	0.0025
$p_T(\ell b)$	p_T of the ℓb system	0.0005
$\Delta\eta(\ell, b)$	$\Delta\eta$ between the ℓ and b -tagged jet	0.0003
$\Delta\phi(\ell, b)$	$\Delta\phi$ between the ℓ and b -tagged jet	0.0003
$\Delta R(\ell, b)$	ΔR between the ℓ and b -tagged jet	0.0001

Table 9: A list of the input variables used in the object-level BDT, ordered by variable importance (descending, top to bottom) is shown.

976 In Figure 29, normalised distributions of the input variables used in the object-level BDT, for the signal and
 977 background classes are shown.

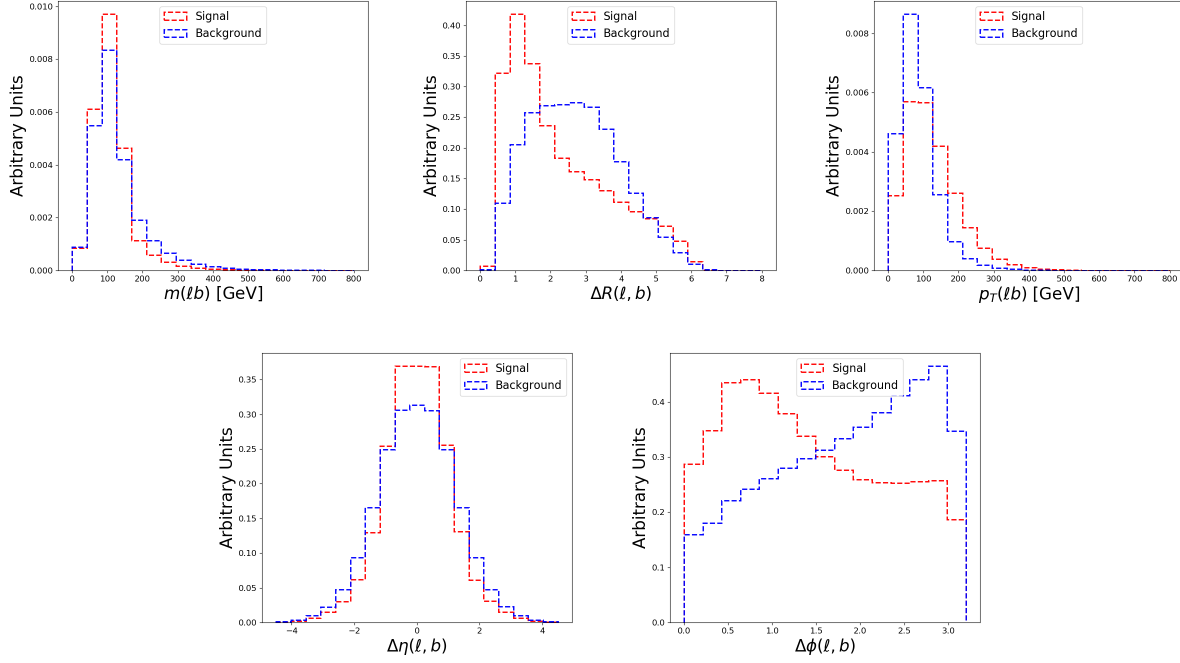


Figure 29: Normalised distributions of the input variables used in the object-level BDT (ordered from top left to bottom right via decreasing variable importance), for the signal and background classes are shown. **From top left to bottom right:** The invariant mass of the ℓb system, ΔR between the ℓ and b -tagged jet, the p_T of the ℓb system, $\Delta\eta$ between the ℓ and b -tagged jet, and $\Delta\phi$ between the ℓ and b -tagged jet. The red and blue dotted lined histograms represent the signal and background classes events (from the training set), respectively. These histograms are normalised to an area of 1. The input variable used in training is shown on the x-axis. The y-axis shows the relative number of events for the signal and background classes in arbitrary units.

978 The input variables used in the object-level BDT show a clear distinction between signal and background ℓb systems.
 979 The modelling of the input variables used in the object-level BDT can be checked by studying the agreement between
 980 data and simulation in the $t\bar{t}Z$ CR. In Figure 30, MC predictions for the input variables used in the object-level
 981 BDT in the $t\bar{t}Z$ CR are shown.

982 Overall, there is good agreement between data and simulation for the input variables used in the object-level BDT,
 983 in the $t\bar{t}Z$ CR. This suggests that the input variables used in the object-level BDT are well-modelled and are
 984 reasonable to include as inputs to the object-level BDT. A final check can be done to study the similarity of the ℓb
 985 systems present in the $t\bar{t}$ sample which are used for training the object-level BDT, and the ℓb systems which are
 986 aimed to be identified using the object-level BDT. More specifically, the study is done to ensure that the modelling
 987 of the ℓb systems in the $t\bar{t}$ sample are sufficiently similar to those in the tWZ and $t\bar{t}Z$ samples (see Table 3). This is
 988 done to understand how well the BDT (trained on ℓb systems in the $t\bar{t}$ sample) generalises to classifying ℓb systems
 989 in the analysis (tWZ and $t\bar{t}Z$ samples). In Figure 31, normalised distributions of the input variables used in the
 990 object-level BDT for the $t\bar{t}$, tWZ and $t\bar{t}Z$ samples, are shown.

991 The distributions of the signal events from all three processes for all of the input variables show minimal deviation
 992 between one another. This suggests that the ℓb systems, that are classified as signal in training, are similar to those
 993 used in the analysis and are therefore sufficient to include in training. There are substantially larger deviations
 994 in the distributions of the background events (compared to the signal events) from all three processes for all of
 995 the input variables. The deviations are especially noticeable in the $\Delta\phi(\ell, b)$ distribution, with a large excess of $t\bar{t}$
 996 background events over the remaining processes. These deviations suggest that the use of the $t\bar{t}$ sample in training
 997 the object-level BDT may be sub-optimal in classifying ℓb systems which do not originate from top quarks. However,
 998 it still represents the best option available, since our other options involve utilising of a subset of generated events
 999 used in the other parts of the analysis. This would result in a smaller number of generated events used in the
 1000 background prediction, leading to larger MC statistical uncertainties. In Table 10, the hyper-parameters used in

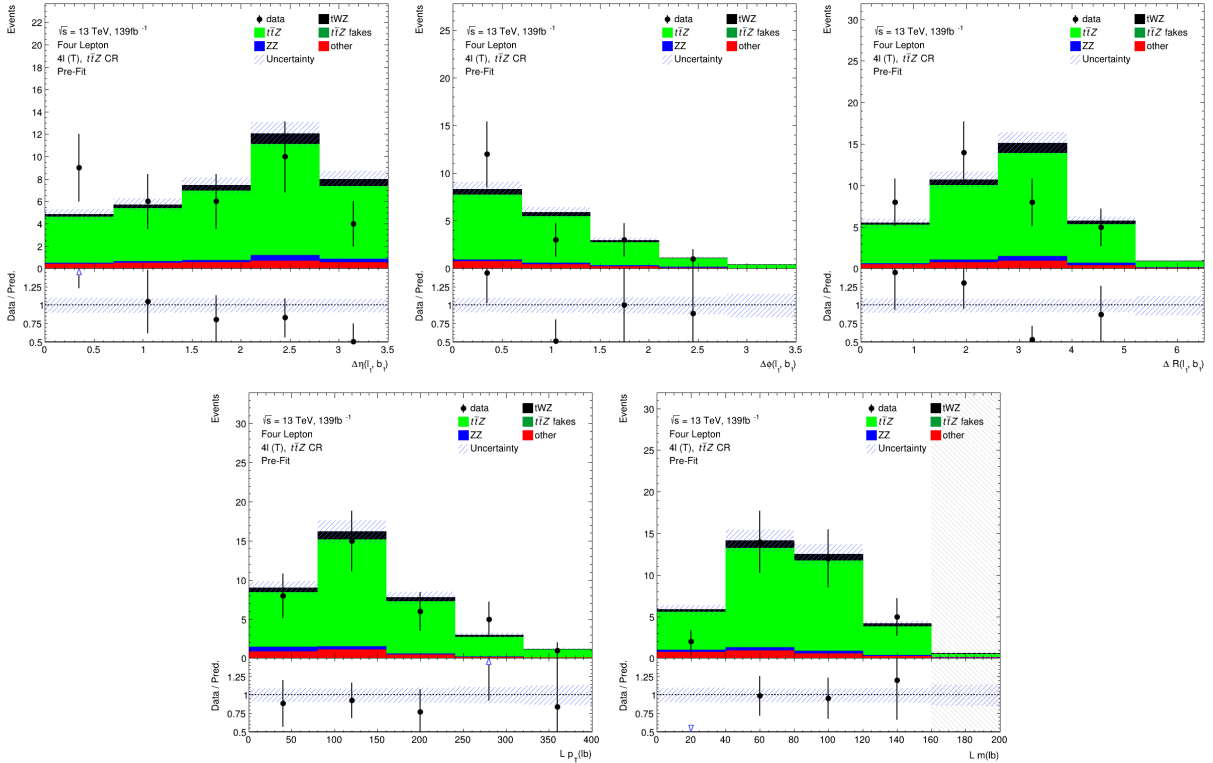


Figure 30: The expected number of events for the object-level BDT input variables (ordered from top left to bottom right via decreasing variable importance), in the $t\bar{t}Z$ CR, are shown. **From top left to bottom right:** $\Delta\eta$ between the lepton and b -jet of the leading ℓb system, $\Delta\phi$ between the lepton and b -jet of the leading ℓb system, ΔR between the lepton and b -jet of the leading ℓb system, p_T of the leading ℓb system, and the mass of the leading ℓb system. The data is given by the black points and the MC predictions for each process are given by the filled histograms. The vertical lines on the data points represent the statistical uncertainty in the data and the blue diagonally-lined bands represent the total (statistical and systematic added in quadrature) uncertainty. The lower panel in each plot shows the ratios of the data to the theoretical predictions. Bins with $\frac{\text{signal}}{\text{background}} > 0.1$ are kept blinded. Blinded bins are shaded with black diagonal lines and their data points are omitted.

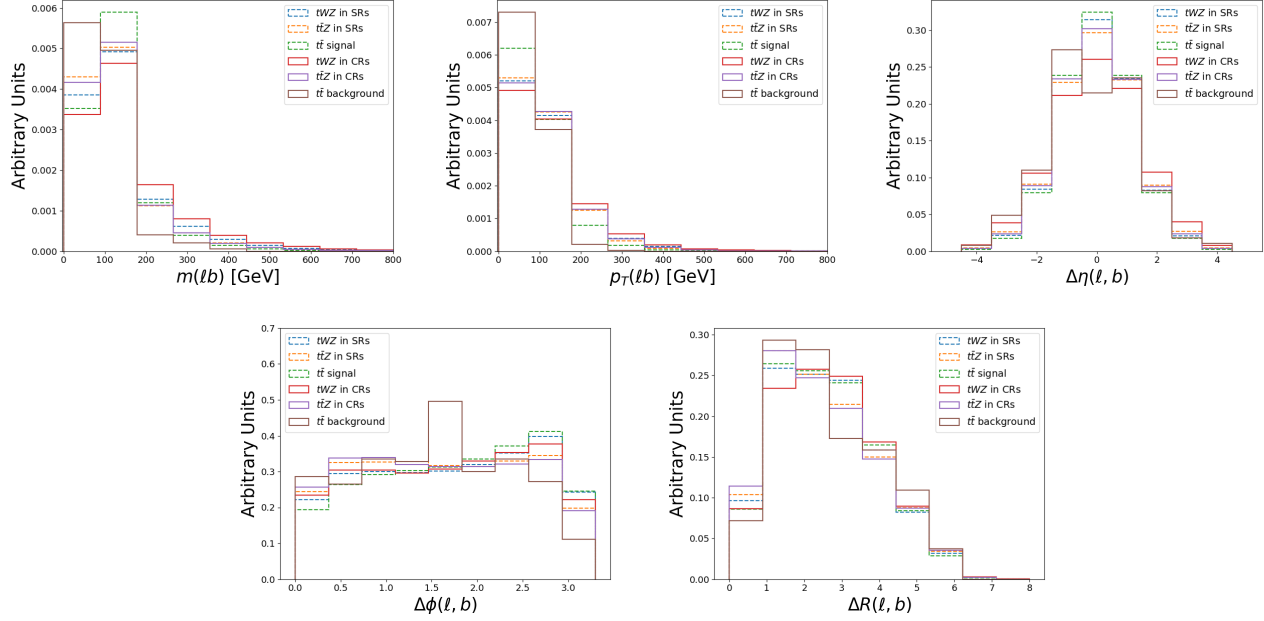


Figure 31: Normalised distributions of the input variables (ordered from top left to bottom right via decreasing variable importance) used in the object-level BDT for the $t\bar{t}$, tWZ and ttZ samples, are shown. **From top left to bottom right:** The invariant mass of the ℓb system, ΔR between the ℓ and b -tagged jet, the p_T of the ℓb system, $\Delta\eta$ between the ℓ and b -tagged jet, $\Delta\phi$ between the ℓ and b -tagged jet. The blue and orange dotted lined histograms represent events from the tWZ and ttZ samples in the SRs, respectively. The red and purple solid lined histograms represent events from the tWZ and ttZ samples in the CRs, respectively. The dotted lined green histogram and the solid lined brown histogram represents signal and background events from the $t\bar{t}$ sample, respectively. These histograms are normalised to an area of 1. The input variable used in training is shown on the x-axis. The y-axis shows the relative number of events in arbitrary units.

the object-level BDT is shown.

Hyper-parameter	Value	Description
loss	deviance	The loss function to be optimised
criterion	friedman_mse	The function used to measure the quality of a split
n_estimators	200	The number of boosting stages to perform
learning_rate	0.1	The step size at each iteration during optimisation
max_depth	6	The maximum depth of the individual regression estimators
min_samples_split	2	The minimum number of samples (events) required to split an internal node
min_samples_leaf	1	The minimum number of samples (events) required to be at a leaf node
validation_fraction	0.1	The proportion of training data to set aside as validation set for early stopping
n_iter_no_change	20	Training terminates when the validation score (determined by the validation set) does not improve in all of the previous

Table 10: A list of the hyper-parameters used in the object-level BDT is shown. Hyper-parameters not listed in this table use the default values as stated in the Scikit-learn Documentation[87].

1001
1002 The number of events used in training for the signal and background classes were 49871 and 384152 respectively.
1003 Imbalanced datasets can cause ML classifiers to ignore small classes while concentrating on classifying large classes
1004 more accurately, which may result in the trained BDT performing sub-optimally. In order to correct this dataset
1005 imbalance, it is ensured that the relative weighting of each event is such that the sum of the signal weights is equal
1006 to the sum of the background weights. In order to avoid over-training, the BDT outputs to the training set and a
1007 test set can be studied. If over-training occurs, the BDT will fit the data in the training set too closely, resulting
1008 in the BDT outputs of the training and test sets to differ. In Figure 32 the normalised histograms of the training
1009 and test sets (extracted from fold 5 from a 5 fold kfold cross validation) for signal and background is shown.
1010 The shapes of the training and test sets for both signal and background agree within uncertainties in the vast
1011 majority of bins. This is a good indicator that no over-training occurred, since it indicates that statistical fluctuations
1012 (or noise) present in the training set was not learnt during training. Another over-training check is performed using
1013 5 fold kfold cross validation. To ensure that the BDT is not over-training, it is ensured that the variance of the

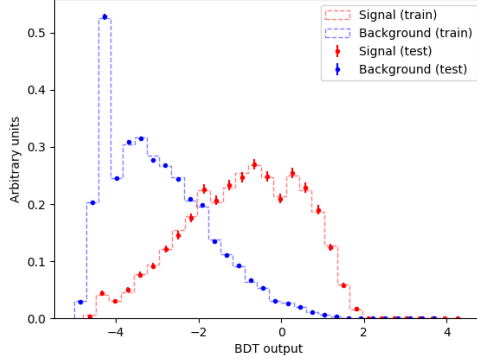


Figure 32: Normalised histograms of the object-level BDT discriminator output from the signal and background classes for the training and test sets from the 5th fold in a 5 fold kfold cross validation is shown. The output of the object-level BDT is shown on the x-axis and the relative number of events in arbitrary units, is shown on the y-axis. The training set for the signal class is shown by the red dotted histogram. The test set for the signal class is shown by the red points, with the total uncertainty represented by the vertical error bars. The training set for the background class is shown by the blue dotted histogram. The test set for the background class is shown by the blue points, with the total uncertainty represented by the vertical error bars.

mean accuracy of each folds' test set in cross validation is substantially small. This tells us that the BDT does not perform better on one subset of a dataset over another and it is therefore not prone to learning statistical fluctuations of a subset, which would result in a BDT which does not generalise well to unseen datasets. For the object-level BDT, a variance of 3.24×10^{-7} was calculated for the mean accuracies of each folds' test set in cross validation. This small variance therefore provides further evidence that no over-training occurred. The output of the object-level BDT is converted to an event-level variable to be used in the event-level BDT. This variable, $\text{BDTScore}(\frac{\text{Best}}{\text{2nd Best}})$, takes the ratio of the scores of the top scoring ℓb system to the 2nd best scoring ℓb system. The 2nd best scoring ℓb system in a tWZ event is expected to be low, since there is only one ℓb system originating from a top quark. Thus $\text{BDTScore}(\frac{\text{Best}}{\text{2nd Best}})$ is expected to be large for tWZ events and closer to one for $t\bar{t}Z$ events, therefore providing discrimination between tWZ and $t\bar{t}Z$. In Figure 33, normalised distributions of the signal and total background of the $\text{BDTScore}(\frac{\text{Best}}{\text{2nd Best}})$ variable in the tWZ OF SR, tWZ SF SR and $t\bar{t}Z$ CR are shown.

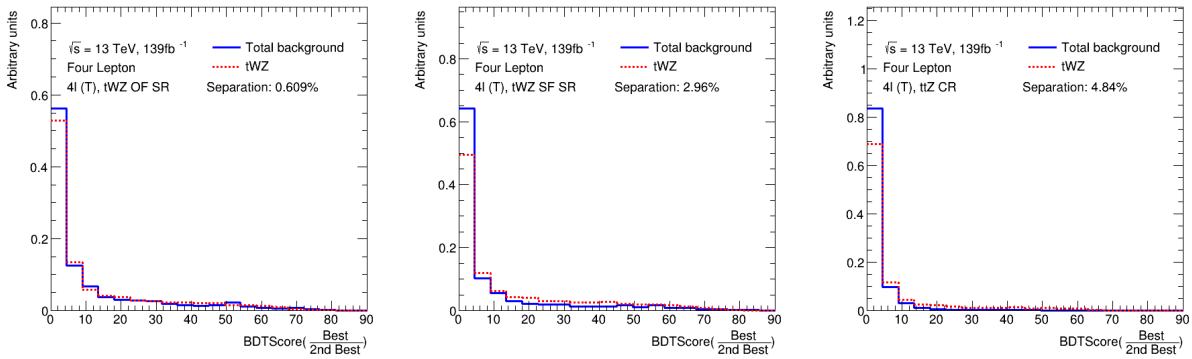


Figure 33: Normalised distributions of the signal and total background of the $\text{BDTScore}(\frac{\text{Best}}{\text{2nd Best}})$ variable in the tWZ OF SR, tWZ SF SR and $t\bar{t}Z$ CR (left to right) are shown. The dotted red and solid blue lines represent the distributions of the signal and total background events respectively. These histograms are normalised to an area of 1. The x-axis shows the $\text{BDTScore}(\frac{\text{Best}}{\text{2nd Best}})$ and the y-axis show the relative number of events in arbitrary units.

The amount of discrimination can be quantified by the separation metric, which gives the percentage of the total area of the distributions which do not overlap. A value of 1 indicates that the distributions are fully separated (no overlap) and a value of 0 indicates that the distributions have no separation (fully overlapped). The separation between signal and background for $\text{BDTScore}(\frac{\text{Best}}{\text{2nd Best}})$ in the tWZ OF SR, tWZ SF SR and $t\bar{t}Z$ CR are 0.609%,

2.96% and 4.84% respectively. The larger separation in the $t\bar{Z}$ CR, compared to the tWZ SRs, can be explained since there is a larger proportion of $t\bar{Z}$ events (events with two ℓb systems) in this region, due to the baseline selection requirement of exactly two b -tagged jets. In a similar way, the smaller separation in the two tWZ SRs can be explained by the tighter selection on the number of b -tagged jets (exactly one) leading to regions which are enriched in only one ℓb system which originates from a top quark. Using the $\text{BDTScore}(\frac{\text{Best}}{\text{2nd Best}})$ variable in training in the event-level BDT (see Section 4.7.4) improves the mean accuracy of the BDT. This tells us that the event-level BDT is taking advantage of the discrimination between signal and background present in the $\text{BDTScore}(\frac{\text{Best}}{\text{2nd Best}})$ variable. In an attempt to optimise the performance of the object-level BDT, signal events which are pure in ℓb systems originating from top quarks are targeted for training the BDT. Similarly, background events which are pure in ℓb systems which do not originate from top quarks are targeted for training the BDT. This is done by studying the distribution of ΔR between the reconstructed ℓb system and the truth ℓb system ($\Delta R((lb)_{reco}, (lb)_{truth})$), and excluding ℓb systems from training which are moderately matched in ΔR to their truth counterparts, leaving well matched ℓb systems being labelled as signal and badly matched ℓb systems labelled as background. The ΔR range where ℓb systems are excluded from training is referred to as the exclusion region. In Figure 34, the distribution of ΔR between the reconstructed ℓb system and the truth ℓb system ($\Delta R((lb)_{reco}, (lb)_{truth})$) in the $t\bar{t}$ sample, along with the exclusion region, is shown.

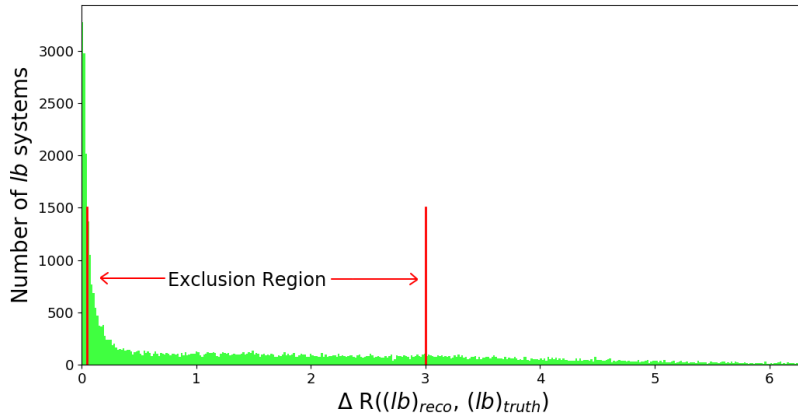


Figure 34: The distribution of ΔR between the reconstructed ℓb system and the truth ℓb system ($\Delta R((lb)_{reco}, (lb)_{truth})$) in the $t\bar{t}$ sample, along with the exclusion region, is shown. The ΔR distribution is shown in green. ΔR between the reconstructed ℓb system and the truth ℓb system ($\Delta R((lb)_{reco}, (lb)_{truth})$) is shown on the x-axis. The number of ℓb systems is shown on the y-axis. The exclusion region is shown between the vertical red lines situated at $\Delta R((lb)_{reco}, (lb)_{truth}) = 0.05$ and $\Delta R((lb)_{reco}, (lb)_{truth}) = 3.0$. Reconstructed ℓb systems with $\Delta R((lb)_{reco}, (lb)_{truth}) \leq 0.05$ are labelled as signal and reconstructed ℓb systems with $\Delta R((lb)_{reco}, (lb)_{truth}) \geq 3.0$ are labelled as background.

A large number of reconstructed ℓb systems have $\Delta R((lb)_{reco}, (lb)_{truth})$ at values near 0. These are matched (in ΔR) extremely well to truth ℓb systems originating from top quarks. Therefore our exclusion region is defined to be between $0.05 < \Delta R((lb)_{reco}, (lb)_{truth}) < 3.0$, such that all reconstructed ℓb systems with $\Delta R((lb)_{reco}, (lb)_{truth}) \leq 0.05$ are labelled as signal and reconstructed ℓb systems with $\Delta R((lb)_{reco}, (lb)_{truth}) \geq 3.0$ are labelled as background. All reconstructed ℓb systems with $0.05 < \Delta R((lb)_{reco}, (lb)_{truth}) < 3.0$ are excluded from training. The performance of the object-level BDT with and without the exclusion region can be compared by studying the discrimination between signal and background events in the $\text{BDTScore}(\frac{\text{Best}}{\text{2nd Best}})$ variable (object-level output converted to an event-level variable to be used in the event-level BDT) for both object-level BDTs. In Figure 35, normalised distributions of $\text{BDTScore}(\frac{\text{Best}}{\text{2nd Best}})$ using the object-level BDT without the exclusion region (see Figure 34) for the tWZ OF SR, tWZ SF SR and $t\bar{t}Z$ CR are shown.

The separation metrics can be compared between the $\text{BDTScore}(\frac{\text{Best}}{\text{2nd Best}})$ variable in the tWZ OF SR, tWZ SF SR and $t\bar{t}Z$ CR for the object-level BDT with (Figure 33) and without (Figure 35) the exclusion region by taking the absolute difference between the two values in each region. The differences are 0.31%, 0.37% and 0.36% for the tWZ OF SR, tWZ SF SR and $t\bar{t}Z$ CR, respectively. These differences are minimal and the object-level BDT with the exclusion region outperforms the object-level BDT without the exclusion region in the tWZ SF SR. Due to the small differences in performance between the two BDTs, the BDT with the exclusion region was chosen to be kept.

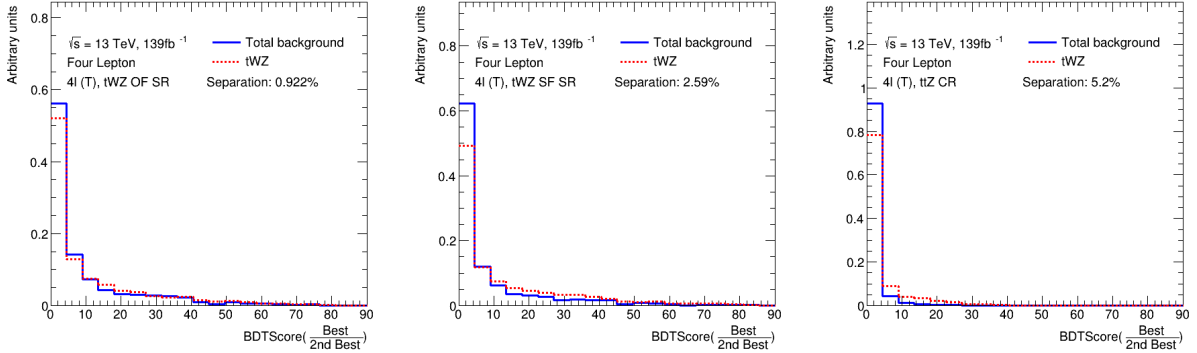


Figure 35: Normalised distributions of $\text{BDTScore}(\frac{\text{Best}}{\text{2nd Best}})$ using the object-level BDT without the exclusion region (see Figure 34) for the tWZ OF SR, tWZ SF SR and $t\bar{t}Z$ CR (left to right) are shown. The dotted red and solid blue lines represent the distributions of the signal and total background events respectively. These histograms are normalised to an area of 1. The x-axis shows the $\text{BDTScore}(\frac{\text{Best}}{\text{2nd Best}})$ and the y-axis show the relative number of events in arbitrary units.

1061 4.7.4 Event-level BDT

1062 The event-level BDT is used to distinguish between signal and its major background events, $t\bar{t}Z$ and ZZ . The
 1063 key difference between the object-level BDT and the event-level BDT is that while the former exploits information
 1064 associated with ℓb systems and thus distinguishes between ℓb systems, the event-level BDT exploits information
 1065 based on the entirety of the event and thus distinguishes between events. The event-level BDT was trained on 50%
 1066 of the tWZ MC sample's events for the signal class and similarly, 50% of the $t\bar{t}Z$ and ZZ MC sample's events
 1067 were used for the background class. The input variables used to train the BDT are chosen on the basis that they
 1068 are somewhat uncorrelated from one another and show some discrimination between tWZ and $t\bar{t}Z$. Similarly to
 1069 the object-level BDT, the optimum values for the hyper-parameters used were determined via a grid-search (See
 1070 Section 4.7.2) that determined the set of hyper-parameters which maximized the mean accuracy (based off 5 fold
 1071 kfold cross-validation). After hyper-parameter optimisation, the mean accuracy of each fold (determined from 5
 1072 fold kfold cross validation) increased from 0.72 to 0.74 ($\sim 3\%$ increase). The variable importance of each input
 1073 variable was computed in the same way as described for the object-level BDT (See Section 4.7.3). In Table 11, the
 input variables used for training the event-level BDT are shown.

Input Variable	Description	Variable Importance
$2\nu\text{SM}$	Maximum weight from the $2\nu\text{SM}$ algorithm (See Section 4.7.1)	0.029
HT	Scalar sum of jet p_T	0.016
LT	Scalar sum of lepton p_T	0.011
$\sum p_T(b - \text{jet})$	Scalar sum of b -tagged jet p_T	0.006
$\text{BDTScore}(\frac{\text{Best}}{\text{2nd Best}})$	Ratio of the top scoring ℓb system to the 2nd best scoring ℓb system from the output of the object-level BDT (object-level BDT)	0.006
$\Delta\eta(\ell_{1,\text{non-}Z}, \ell_{2,\text{non-}Z})$	$\Delta\eta$ between the two leptons, not coming from a Z candidate	0.005

Table 11: A list of the input variables used in the event-level BDT, ordered by variable importance (descending, top to bottom) is shown.

1074 In Figure 36, normalised distributions of the input variables used in the event-level BDT, for the signal and
 1075 background classes are shown.
 1076 The input variables used in the event-level BDT show a clear distinction between signal and background events. In
 1077 particular the output weight from the $2\nu\text{SM}$ algorithm shows the most discrimination. When determining which
 1078 input variables to use to train the event-level BDT, the output weight from $2\nu\text{SM}$ was shown to provide the most
 1079 sizeable boost in performance of the BDT. Surprisingly, the least important input variable, $\Delta\phi$ between the non- Z
 1080 lepton system (leptons not originating from a Z -candidate) and the leading b -tagged jet, seem to discriminate well
 1081 between signal and background. A possible explanation for its low ranking variable importance is due to it being
 1082 relatively highly correlated with many of the other input variables used in the BDT. The modelling of the input
 1083 variables used in the event-level BDT can be checked by referring to the expected number of events of data and
 1084 simulation in control regions where they are defined. Note that certain input variables which are ill-defined in
 1085 certain regions (e.g. $\Delta\eta(\ell_{1,\text{non-}Z}, \ell_{2,\text{non-}Z})$ in the ZZb CR, as all leptons originate from a b -jet in this region) will
 1086 not be shown. In Figure 37, MC predictions for the input variables used in the event-level BDT in the $t\bar{t}Z$ CR are

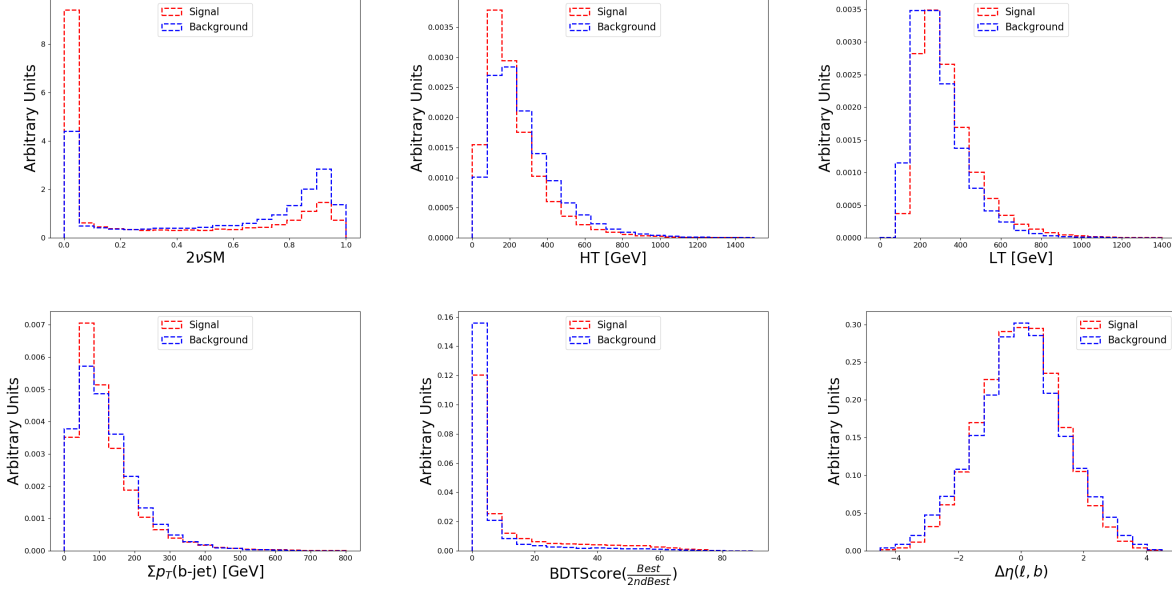


Figure 36: Normalised distributions of the input variables used in the event-level BDT (ordered from top left to bottom right via decreasing variable importance), for the signal and background classes are shown. **From top left to bottom right:** The output weight from the $2\nu\text{SM}$ algorithm (See Section 4.7.1), the scalar sum of jet p_T , the scalar sum of lepton p_T , the sum of b -tagged jet p_T , the ratio of the top scoring ℓb system to the 2nd best scoring ℓb system from the output of the object-level BDT (See Section 4.7.3), and $\Delta\eta$ between the two leptons, not coming from a Z candidate. The red and blue dotted lined histograms represent the signal and background classes events, respectively. These histograms are normalised to an area of 1. The input variable used in training is shown on the x-axis. The y-axis shows the relative number of events for the signal and background classes in arbitrary units.

1088 shown. The deviations between data and simulation, across all input variables used in the $t\bar{t}Z$ CR, in all but three
 1089 bins are within expected uncertainties. In Figure 38, MC predictions for the input variables used in the event-level
 1090 BDT in the ZZb CR are shown. The deviations between data and simulation, across all input variables used in
 1091 the ZZb CR, are within expected uncertainties. In Figure 39, MC predictions for the input variables used in the
 1092 event-level BDT in the $(tWZ)_{\text{fake}}$ CR are shown.

1093 The deviations between data and simulation, across all input variables used in the $(tWZ)_{\text{fake}}$ CR, in all but one
 1094 bin are within expected uncertainties. Overall, the vast majority of predictions between data and simulation in
 1095 the bins of the event-level BDT distributions in the $t\bar{t}Z$ CR, ZZb CR and $(tWZ)_{\text{fake}}$ CR, are within the expected
 1096 uncertainties. Therefore, these input variables are well-modelled and reasonable to include as inputs to the
 1097 event-level BDT.

1098

In Table 12, the hyper-parameters used in the event-level BDT are shown.

Hyper-parameter	Value	Description
loss	deviance	The loss function to be optimised
criterion	friedman_mse	The function used to measure the quality of a split
n_estimators	200	The number of boosting stages to perform
learning_rate	0.1	The step size at each iteration during optimisation
max_depth	6	The maximum depth of the individual regression estimators
min_samples_split	2	The minimum number of samples (events) required to split an internal node
min_samples_leaf	1	The minimum number of samples (events) required to be at a leaf node
validation_fraction	0.1	The proportion of training data to set aside as validation set for early stopping
n_iter_no_change	20	Training terminates when the validation score (determined by the validation set) does not improve in all of the previous

Table 12: A list of the hyper-parameters used in the event-level BDT is shown. Hyper-parameters not listed in this table use the default values as stated in the Scikit-learn Documentation[87].

1099

1100 Since the training is performed on $t\bar{t}Z$ and ZZ events for the background class, it is ensured that the relative
 1101 weighting of these events are such that they mimic the amount of $t\bar{t}Z$ and ZZ expected to be present in the regions
 1102 where the BDT discriminator (tWZ SRs and $t\bar{t}Z$ CR) is used. This is done by applying normalization weights to

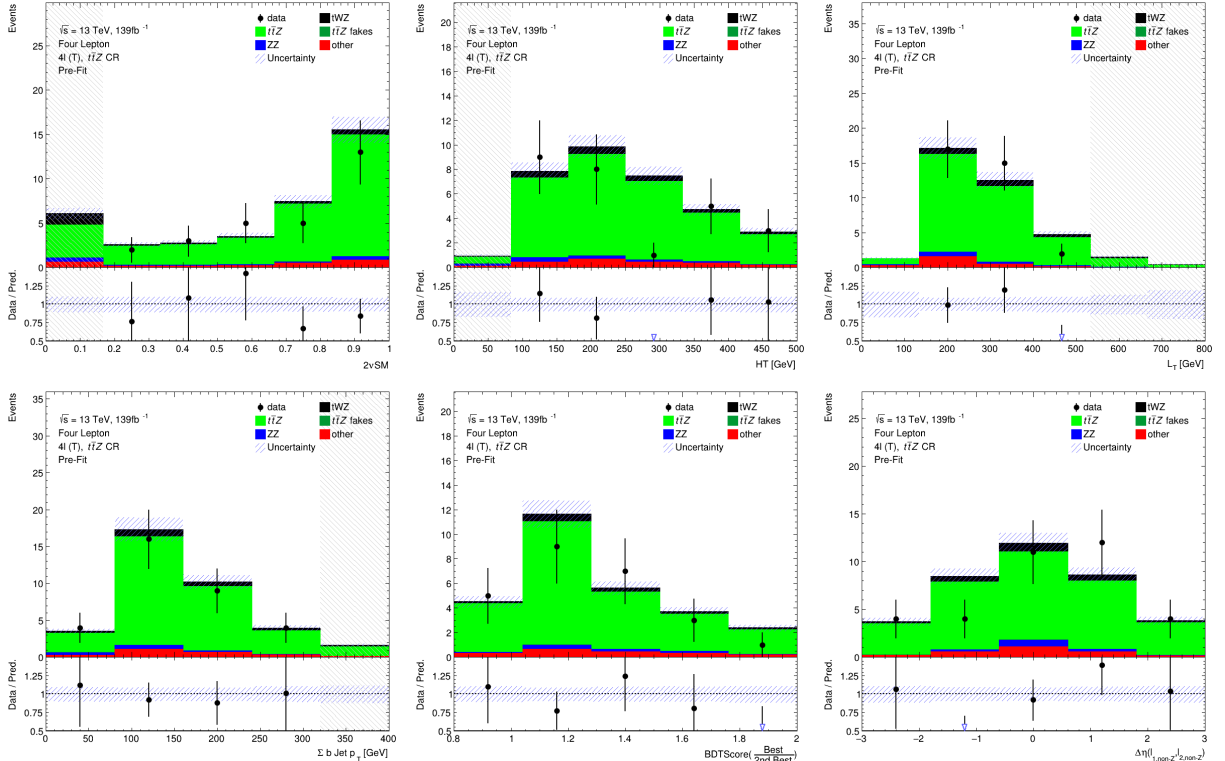


Figure 37: The expected number of events for the event-level BDT input variables (ordered from top left to bottom right via decreasing variable importance), in the $t\bar{t}Z$ CR, are shown. **From top left to bottom right:** The output weight from the 2ν SM algorithm (See Section 4.7.1), the scalar sum of jet p_T , the scalar sum of lepton p_T , the sum of b -tagged jet p_T , ratio of the top scoring ℓb system to the 2nd best scoring ℓb system from the output of the object-level BDT (See Section 4.7.3), and $\Delta\eta$ between the two leptons, not coming from a Z candidate. The data is given by the black points and the MC predictions for each process are given by the filled histograms. The vertical lines on the data points represent the statistical uncertainty in the data and the blue diagonally-lined bands represent the total (statistical and systematic added in quadrature) uncertainty. The lower panel in each plot shows the ratios of the data to the theoretical predictions. Bins with $\frac{\text{signal}}{\text{background}}$ greater than 0.1 are kept blinded. Blinded bins are shaded with black diagonal lines and their data points are omitted.

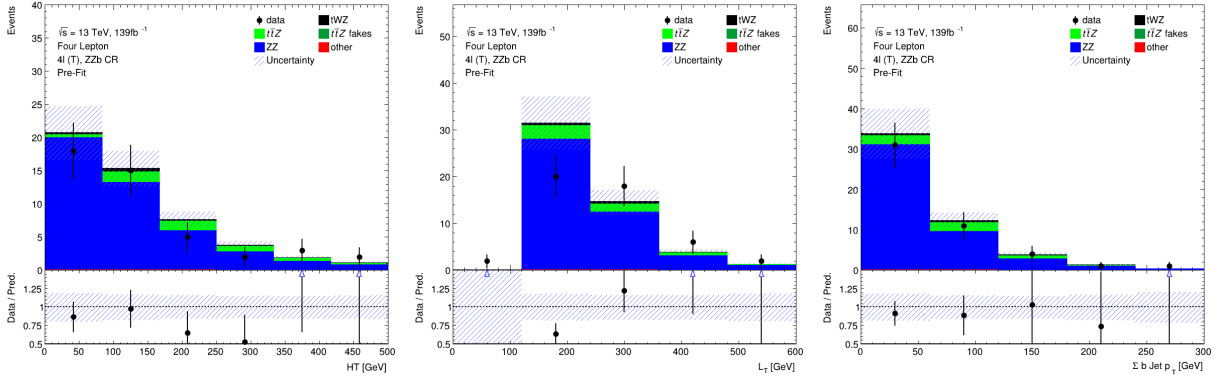


Figure 38: The expected number of events for the event-level BDT input variables (ordered from top left to bottom right via decreasing variable importance), in the ZZb CR, are shown. **From left to right:** The scalar sum of jet p_T , the scalar sum of lepton p_T , and the sum of b -tagged jet p_T . The data is given by the black points and the MC predictions for each process are given by the filled histograms. The vertical lines on the data points represent the statistical uncertainty in the data and the blue diagonally-lined bands represent the total (statistical and systematic added in quadrature) uncertainty. The lower panel in each plot shows the ratios of the data to the theoretical predictions. Bins with $\frac{\text{signal}}{\text{background}}$ greater than 0.1 are kept blinded. Blinded bins are shaded with black diagonal lines and their data points are omitted.

1103 each event, defined as,

$$W = \frac{\sigma \mathcal{L} \text{weight(MC)}}{\text{totalWeight(MC)}} \quad (4.14)$$

1104 where σ is the cross section of the process, \mathcal{L} is the integrated luminosity, weight(MC) is the weight assigned to the
 1105 event by the MC event generator and totalWeight(MC) is the sum of those weights for all the generated events.
 1106 The number of events used in training for the signal and background classes were 41066 and 22608 respectively.
 1107 Similarly to the object-level BDT, there is a dataset imbalance. This imbalance is corrected for (in the same way
 1108 as before with the object-level BDT) by ensuring that the relative weighting of each event is such that the sum of
 1109 the signal weights is equal to the sum of the background weights. In order to avoid over-training, in the same way
 1110 that was performed for the object-level BDT (See Section 4.7.3), the BDT outputs to the training set and a test
 1111 set can be studied. In Figure 40 the normalised histograms of the training and test sets (extracted from fold 5 from
 1112 a 5 fold kfold cross validation) for signal and background is shown.

1113 The shapes of the training and test sets for both signal and background agree within uncertainties in the vast
 1114 majority of bins. This is a good indicator that no over-training occurred, since it indicates that statistical fluctuations
 1115 (or noise) present in the training set was not learnt during training. As with the object-level BDT, another over-
 1116 training check is performed, by ensuring that the variance of the mean accuracy of each folds' test set in a 5 fold
 1117 kfold cross validation is sufficiently small. This indicates that fluctuations in features from different training sets
 1118 are not learnt by the BDT. For the event-level BDT, a variance of 0.00026 was calculated for the mean accuracies
 1119 of each folds' test set in cross validation, providing further evidence that no over-training occurred. In Figure 41,
 1120 normalised distributions of the signal and total background of the event-level BDT discriminator output in the
 1121 tWZ OF SR, tWZ SF SR and $t\bar{t}Z$ CR, are shown.

1122 The event-level BDT discriminates well between signal and background events in the tWZ OF SR, tWZ SF SR
 1123 and $t\bar{t}Z$ CR, with separations of 8.98%, 10.6% and 20.6%, respectively.

1124 4.8 Systematic Uncertainties

1125 The final results are obtained with a maximum likelihood fit (described in Section 4.9.1) in which normalisations and
 1126 shapes of distributions are allowed to vary to account for uncertainties of both experimental and theoretical origin.
 1127 Systematic uncertainties are allowed to vary within a pre-determined envelope (consisting of two MC templates)
 1128 which defines the bounds within which the systematic can vary. In this section, the methods used to determine the
 1129 variations that form the inputs to the fit are described.

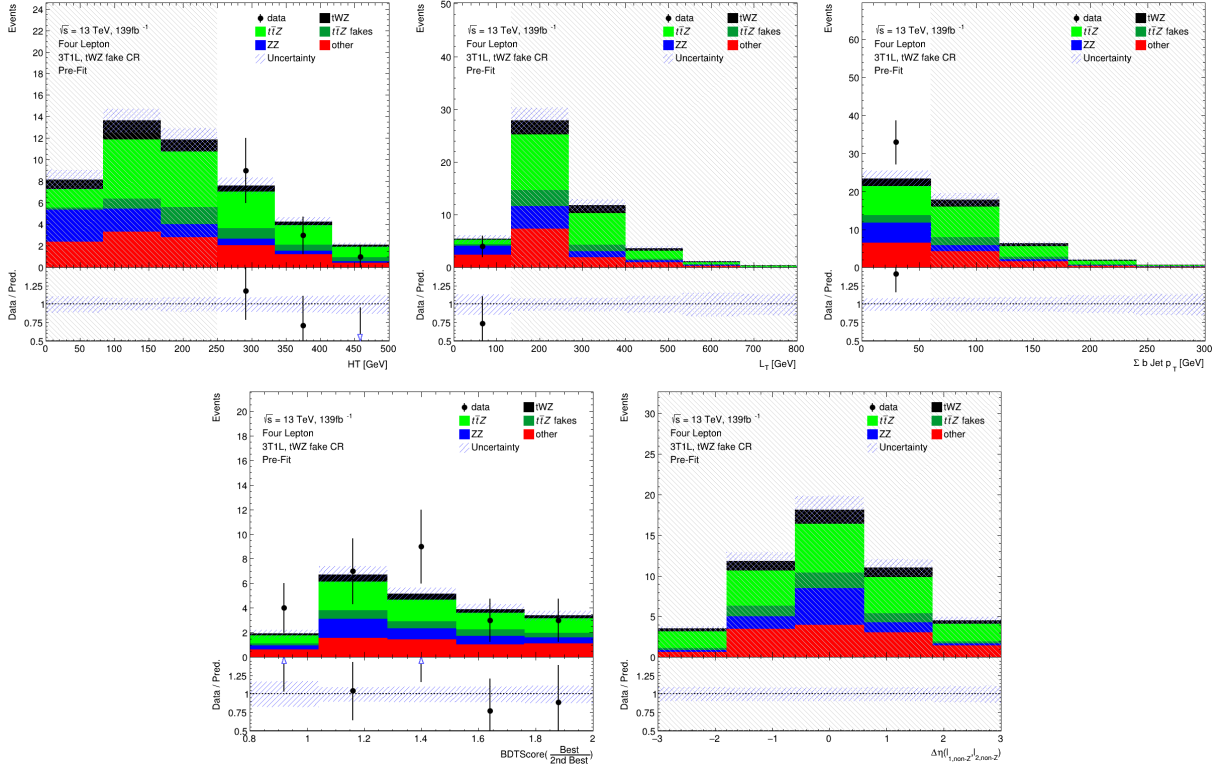


Figure 39: The expected number of events for the event-level BDT input variables (ordered from top left to bottom right via decreasing variable importance), in the $(tWZ)_{\text{fake}}$ CR, are shown. **From top left to bottom right:** The output weight from the $2\nu\text{SM}$ algorithm (See Section 4.7.1), the scalar sum of jet p_T , the scalar sum of lepton p_T , the sum of b -tagged jet p_T , ratio of the top scoring ℓb system to the 2nd best scoring ℓb system from the output of the object-level BDT (See Section 4.7.3), and $\Delta\eta$ between the two leptons, not coming from a Z candidate. The data is given by the black points and the MC predictions for each process are given by the filled histograms. The vertical lines on the data points represent the statistical uncertainty in the data and the blue diagonally-lined bands represent the total (statistical and systematic added in quadrature) uncertainty. The lower panel in each plot shows the ratios of the data to the theoretical predictions. Bins with $\frac{\text{signal}}{\text{background}}$ greater than 0.1 are kept blinded. Blinded bins are shaded with black diagonal lines and their data points are omitted.

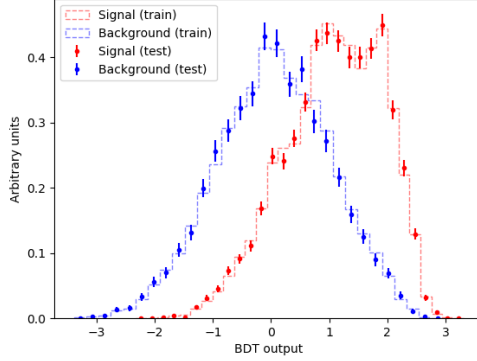


Figure 40: Normalised histograms of the event-level BDT discriminator output from the signal and background classes for the training and test sets from the 5th fold in a 5 fold kfold cross validation are shown. The output of the event-level BDT is shown on the x-axis and the relative number of events (normalised to have an area of 1, in arbitrary units) is shown on the y-axis. The training set for the signal class is shown by the red dotted histogram. The test set for the signal class is shown by the red points, with the total uncertainty represented by the vertical error bars. The training set for the background class is shown by the blue dotted histogram. The test set for the background class is shown by the blue points, with the total uncertainty represented by the vertical error bars.

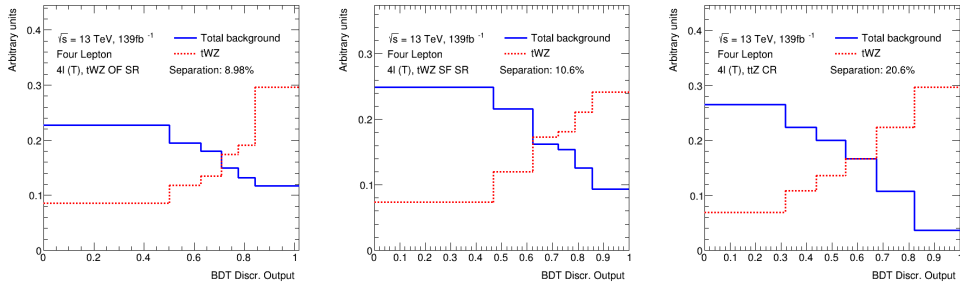


Figure 41: Normalised distributions of the signal and total background of the event-level BDT discriminator output in the tWZ OF SR, tWZ SF SR and ttZ CR (left to right) are shown. The dotted red and solid blue lines represent the distributions of the signal and total background events respectively. These histograms are normalised to an area of 1. The x-axis shows the event-level BDT discriminator output and the y-axis shows the relative number of events in arbitrary units.

1130 4.8.1 Experimental uncertainties

1131 In this section, the experimental systematic uncertainties are outlined.

- 1132 • **Luminosity:**

1133 The 2015-2018 luminosity estimate of 139fb^{-1} has a relative uncertainty of 3%. The uncertainty associated
1134 with the luminosity is obtained using the LUCID-2 detector [22], which is the primary luminosity monitor for
1135 ATLAS. This systematic uncertainty affects all processes modelled using MC simulations.

- 1136 • **Pile-up modelling:**

1137 An uncertainty related to the SFs used for MC to account for differences in pile-up distributions between
1138 MC and data is applied. This uncertainty is obtained by re-scaling the $\langle\mu\rangle$ value in data by 1.00 and 1/1.18
1139 corrections are only applied to MC.

- 1140 • **Jet vertex tagger:**

1141 Uncertainties associated to the JVT are applied via the `JetJvtEfficiency` package [20] which account for
1142 the residual contamination from pile-up jets after pile-up suppression and the MC generator choice [14].

1143 • **Heavy- and light-flavor tagging:**

1144 An additional uncertainty is assigned to account for the extrapolation of the b -tagging efficiency measurement
1145 from the p_T region used to determine the correction factors to regions with higher p_T .

1146 • **Electron efficiency:**

1147 Uncertainties associated with the electron efficiency SFs arise from the reconstruction, ID, isolation and trigger
1148 efficiencies [18]. They correct for the efficiency difference between data and MC [13] and are measured with
1149 a "tag-and-probe" method in $Z \rightarrow e^+e^-$ and $J/\psi \rightarrow e^+e^-$ events. The information on the correlation of
1150 the different components of the systematic uncertainties are provided for all efficiency measurements. The
1151 default correlation model for the uncertainties is used, which provides one up/down variation for each of the
1152 SF components separately [18, 19].

1153 • **Muon efficiency:**

1154 As for electrons, SFs obtained from $Z \rightarrow \mu^+\mu^-$ and $J/\psi \rightarrow \mu^+\mu^-$ events are applied to correct for the
1155 differences between data and MC in the muon ID, isolation and trigger efficiencies [16]. Uncertainties on these
1156 SFs are applied as up/down variations of the nominal SFs for each component.

1157 **4.8.2 Theoretical uncertainties**

1158 In this section, the theoretical systematic uncertainties are outlined.

1159 • **$t\bar{t}Z$ background:**

1160 An overall normalization uncertainty of 10% is considered for the $t\bar{t}Z$ background. Two generic shape system-
1161 atic uncertainties are considered for the $t\bar{t}Z$ background. They are constructed (see Section 4.8.3) by either
1162 applying a linear or triangular interpolation to up and down variations which are defined to be $\pm 20\%$ from
1163 the nominal $t\bar{t}Z$ background. These linear and triangular variations are applied to distributions used in the
1164 maximum likelihood fit (described in Section 4.9.1).

1165 • **ZZ background:**

1166 An overall normalization uncertainty of 30% is considered for the ZZ background.

1167 • **$t\bar{t}H$ background:**

1168 An overall normalization uncertainty of 20% is considered for the $t\bar{t}H$ background.

1169 • **tZq background:**

1170 An overall normalization uncertainty of 14% is considered for the tZq background.

1171 • **$t\bar{t}Z$ fake background:**

1172 An overall normalization uncertainty of 50% is considered for the $t\bar{t}Z$ fake background.

1173 • **other background processes:**

1174 The 'other' background consists of many processes which have minimal but non-negligible contribution in
1175 the signal regions (See Table 7). An overall normalization uncertainty of 30% is considered for the 'other'
1176 background processes.

1177 • **tWZ :**

1178 A modelling uncertainty on tWZ is considered by comparing the nominal sample (using the DR1 scheme) and
1179 a DR2 sample. Two generic shape systematic uncertainties are considered for the tWZ background. They
1180 are constructed (see Section 4.8.3) by either applying a linear or triangular interpolation to up and down
1181 variations which are defined to be $\pm 20\%$ from the nominal tWZ background.

4.8.3 Generic shape systematic uncertainties

The quantity which is measured from the maximum likelihood fit, the expected signal strength of tWZ ($\mu(tWZ)$), is defined as the ratio of the expected cross section of tWZ , $\sigma_{(tWZ)}$, to the SM cross section of tWZ , $\sigma_{SM}(tWZ)$ (described in more detail in Section 4.9.1). It is evident that the tetralepton channel is statistically limited, as seen by the small number of expected events in the control plots shown previously in Section 4.5. Therefore it is expected that the uncertainty on $\mu(tWZ)$ is dominated by statistical uncertainty and that the impact of shape systematic uncertainties will be negligible in comparison. In this analysis, not all sources of systematic uncertainties have been estimated, as this involves time consuming analysis of extra event samples, especially those related to the modelling of background processes. However, as described above, these missing systematic uncertainties are likely to have negligible impact. To cross check this assumption, generic systematic uncertainties are generated as a proxy for the missing systematic uncertainties for the modelling of processes. If these generic shape systematic uncertainties have negligible impact on the measurement of the expected $\mu(tWZ)$, it would give us confidence that the missing systematic uncertainties will not greatly alter our results when they are eventually added (this is outside the scope of this thesis). An envelope consisting of two MC templates is constructed that represents the bounds in which the systematic can vary in the fit. One with the nominal MC template increased by 20% on its normalisation and the other with the nominal MC template decreased by 20% on its normalisation. The templates are then modified from their original shape either by doing linear interpolation (from the leftmost-up variation to the rightmost-down variation) or triangular interpolation (shape is set to zero at the higher and lower parts and extends towards the envelope in the middle). The linear and triangular interpolation is done using TRF's `ForceShape` option [81], which alters the original templates (as described above). In Figure 42 the envelope before and after the shape change, for both the linear and triangular interpolations, for the $t\bar{t}Z$ background in the $t\bar{t}Z$ CR is shown.

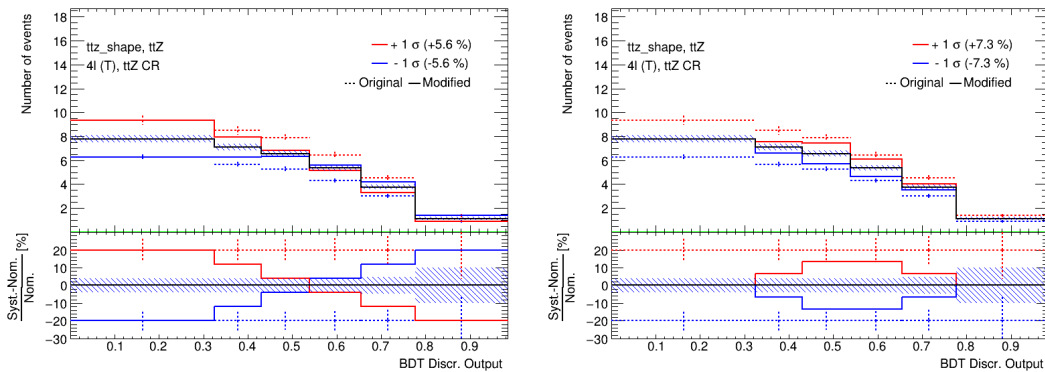


Figure 42: The $t\bar{t}Z$ generic shape systematic before (original) and after (modified) linear (left) and triangular (right) interpolation in the $t\bar{t}Z$ CR is shown. The output from the event-level BDT shown on the x-axis. In the upper panel, the number of events is shown on the y-axis. In the lower panel, the difference between the systematic variation (the envelope's templates) and the nominal template, divided by the nominal template, is shown on the y-axis. The nominal $t\bar{t}Z$ template is shown by the solid black lined histogram, with the diagonal lined bands representing its total uncertainty. The templates of the upper and lower envelopes, before modification, is given by the dotted red and blue lined histograms respectively. The templates of the upper and lower envelopes, after modification, is given by the solid red and blue lined histograms respectively, with the vertical dotted lines representing its total uncertainty.

Both a linear and a triangular generic systematic uncertainty are considered for tWZ and the most dominant background process, $t\bar{t}Z$.

4.9 Analysis Pipeline and **TRExFitter**

For this analysis, we make use of CERN's high energy data analysis framework, **ROOT**, which is written in *C++*, through **Python** using **PyROOT**. **Python** is used extensively in many fields of science (not limited to physics and data science) due to its simplicity and ongoing support by the communities which utilize it. In **PyROOT** users are able to access the full **ROOT** functionality within **Python**. More specifically, **PyROOT** provides **Python** bindings for **ROOT**. To produce all control plots (including fit statistics, e.g. limit, significance, μ_{tWZ}), we used **TRExFitter** (tag: **TRExFitter-00-04-13**), which is a framework for binned template profile likelihood fits [96].

The analysis pipeline starts with sample derivations (data and simulation from ATLAS with certain selection criteria applied in order to reduce its file size such that it is more manageable to work with) being submitted to the grid for dataset production. This applies cuts and selections to the already reduced derivations and produces datasets with trees containing variables (e.g. scale factors, variables, MC truth flags) that will be used at future stages in the analysis. These datasets are then read by PyROOT where the events are looped over, before being written to ROOT files as input to **TRExFitter**. The Python scripts are used to define the different regions and apply the final cuts and selections outlined in Table 6. In addition to this purpose, they are used to train the two BDTs and to produce the output from these trained BDTs. As each event is looped over, the cuts and selection criteria are checked for the given event and is either discarded (if the event does not pass the selection criteria), or gets written to a ROOT file (if the event passes the selection criteria) corresponding to the MC sample and Run 2 data-set which it belongs to. These ROOT files contain all variables, weights and scale factors (corresponding to an event) which we wish to use in **TRExFitter**. **TRExFitter** then takes these files as input, runs a maximum likelihood fit and produces relevant plots (e.g. expected number of events, pull plots) and statistical parameters (e.g. limit, significance, μ_{tWZ}).

4.9.1 Fitting Procedure

Maximum likelihood fits can be used to calculate the probability of data being consistent with a given hypothesis. In this analysis, the hypothesis is represented by the signal strength of tWZ production, $\mu(tWZ)$, defined as,

$$\mu(tWZ) = \frac{\sigma(tWZ)}{\sigma_{SM}(tWZ)} \quad (4.15)$$

where $\sigma_{(tWZ)}$ expected cross section of tWZ and $\sigma_{SM}(tWZ)$ is the SM cross section of tWZ . The maximum likelihood fit is performed by finding the set of values for the parameters which maximize a likelihood function or equivalently by minimizing the negative logarithm of the likelihood function. In this context, the likelihood function is constructed from probability distributions of the expected number of events in each bin of a distribution and the nuisance parameters. The data in a given bin of a distribution is expected to follow a Poisson probability distribution representing its expected number of events. Nuisance parameters represent the systematic uncertainties that could affect the estimation of signal and background but are not directly related to our final measurement. The likelihood function, $L(\mu, \theta)$, used in analyses involving binned histograms of signal and background events is therefore constructed as a product of Poisson probability terms for all bins (N_{bins}) and probability density functions of the nuisance parameters, and is given by [24],

$$L(\mu, \theta) = \prod_i^{N_{bins}} \frac{(\mu s_i(\vec{\theta}) + b_i(\vec{\theta}))^{n_i}}{n_i!} e^{-(\mu s_i(\vec{\theta}) + b_i(\vec{\theta}))} \prod_{\theta \in \vec{\theta}} \rho(\theta) \quad (4.16)$$

where μ is the signal strength of the process of interest, s_i and b_i represent the expected number of signal and background events in bin i of the distribution respectively, θ represents a nuisance parameter contained in the set of all nuisance parameters ($\vec{\theta}$) and $\rho(\theta)$ represents the probability density functions which define the nuisance parameter's distribution. In analyses with multiple regions, the likelihood function contains all bins across the regions. A fit across all regions in the tetralepton channel is performed to determine the sensitivity of tWZ in this channel. Plots shown prior to the fit are referred to as *pre-fit* and those shown after the fit are referred to as *post-fit*. In this analysis, the *mixed data and MC* fit setup [97] is used. This is done to obtain the most accurate prediction of the expected results while keeping the signal regions blinded. For this setup, first a background-only fit to the control regions using data is performed to estimate the nuisance parameters. Then these estimates are used to construct a modified Asimov dataset in the signal regions. Finally, the fit is performed using data in the control regions and the aforementioned modified Asimov data-set in the signal regions. In these fits, the POI is $\mu(tWZ)$. The POI is ultimately the quantity to be measured and it is set as a *free parameter* in the fit. This means that during the fitting procedure, $\mu(tWZ)$ is unconstrained and can take any value in the fit. The nuisance parameters are assigned to the systematic uncertainties outlined in Section 4.8. Furthermore, a gamma (γ) nuisance parameter for a bin is added to the likelihood function if the statistical uncertainty in the bin exceeds 0.1% of its nominal value. A sample's shape and normalisation nuisance parameter is pruned (removed from the limit/fit) if the impact of the systematic uncertainty on the POI is less than 0.01. Pruning is done per sample and per region on the shape and normalisation uncertainties for samples. An auto-binning algorithm, **TransfoD** [32, 33], was used to define the binning. This aims to maximise $\frac{\text{signal}}{\text{background}}$ in each bin. Furthermore, it aims to avoid defining bins with a low number of events. The auto-binning algorithm works by scanning through the bins of the given distribution with

1259 user-defined bins of equal width, and merges bins until a certain fraction of $\frac{\text{signal}}{\text{background}}$ events is obtained. The
 1260 merging threshold, MT , is defined as,

$$MT = z_s \frac{n_s}{N_s} + z_b \frac{n_b}{N_b} \quad (4.17)$$

1261 where n_s and n_b are the number of signal and background events in the merging bin, respectively. The total number
 1262 of signal and background events is given by N_s and N_b , respectively. User-defined parameters, z_s and z_b , control
 1263 the maximum fraction of signal and background events in each bin with the condition, $z_s + z_b = \text{Number of Bins}$.
 1264 A bin is formed when $MT \geq 1$. To characterise the sensitivity and associated uncertainty of our measurement
 1265 of $\mu(tWZ)$, we compute two metrics: the expected significance (Z_μ^{exp}) and the expected upper limit ($\mu_{\text{up}}^{\text{exp}}$). In
 1266 this context, the expected significance can be interpreted as, the probability that the expected signal is due to a
 1267 background fluctuation. The expected significance, Z_μ^{exp} , is related to the p -value. The p -value can be defined as
 1268 the probability, under the assumption of a given hypothesis (in the context of this analysis, this would refer to
 1269 the background-only hypothesis), of finding data of equal or greater incompatibility with the predictions of the
 1270 hypothesis [43]. The expected significance can be written in terms of the p -value (p) by,

$$Z_\mu^{\text{exp}} = \Phi^{-1}(1 - p) \quad (4.18)$$

1271 where Φ^{-1} is the inverse of the cumulative function of the standard Gaussian distribution. This is defined such that
 1272 a Gaussian distributed variable found Z_μ^{exp} standard deviations above its mean has an area under its rightmost
 1273 tail equal to p . Larger values indicate lower probabilities and smaller values indicate higher probabilities. Particles
 1274 physicists have adopted a standard to define the significance necessary for evidence and discovery of a particular
 1275 particle or phenomena. A 3σ (corresponding to a background fluctuation probability of $\approx 10^{-3}$) significance is
 1276 considered to be evidence and a 5σ (corresponding to a background fluctuation probability of $\approx 10^{-7}$) is considered
 1277 to be a discovery. The expected upper limit is a single-sided interval test statistic, associated with the parameter
 1278 of interest (POI) in the maximum-likelihood fit ($\mu(tWZ)$, in our case). In this context, the expected upper limit
 1279 can be understood in the following way: consider running an ensemble of MC toy experiments, each with their own
 1280 confidence interval (a range of possible values for $\mu(tWZ)$). An expected upper limit, at some fixed percentage $x\%$
 1281 (or *confidence level*), can be determined from this ensemble. The expected upper limit tells us that, $x\%$ of the toy
 1282 MC experiment's confidence intervals will contain the true value of $\mu(tWZ)$. A commonly used percentage in particle
 1283 physics is 95%, which we adopt for this analysis. In particle physics, this is referred to as the *CLs Method* [43].
 1284 The CLs test statistic can be calculated 'brute force' by running these MC toy experiments, however this is very
 1285 CPU intensive. Asymptotic formulae are able to describe the underlying CLs test statistic distributions under
 1286 certain approximations [10]. Instead of running toy MC experiments, we use asymptotic formulae to perform the
 1287 CLs method, which considerably reduces computation time. The significance and upper limits which are calculated
 1288 in this analysis are given a prefix of 'expected' to indicate that these are results from a blinded analysis.

1289 4.10 Results

1290 In the section, an expected upper limit and an expected significance are set on the signal strength of tWZ . This is
 1291 performed for the current analysis in the tetralepton channel as well as for a combined analysis across the trilepton
 1292 and tetralepton channels. The trilepton analysis was performed as an independent study by Benjamin Warren
 1293 (UCT) [99]. Note that throughout this section, all signal regions remain blinded.

1294 4.10.1 Tetralepton Channel

1295 In Figure 43, the pre-fit distributions of the expected number of events as a function of the variables used in the
 1296 likelihood fit in each region are shown.

1297 In Figure 44, the post-fit distributions of the expected number of events as a function of the variables used in the
 1298 likelihood fit in each region are shown.

1299 In Table 13, the expected number of events (after the fit) for each sample in each region is shown.
 1300 The expected upper limit of tWZ in the tetralepton channel is measured as, $\mu_{\text{up}}^{\text{exp}} = 1.61^{+2.35}_{-1.16}$. The expected
 1301 significance of tWZ in the tetralepton channel is measured as, $Z_\mu^{\text{exp}} = 1.44\sigma$. The best-fit value of the signal
 1302 strength, $\mu(tWZ) = \frac{\sigma(tWZ)}{\sigma(tWZ)_{SM}}$, from the likelihood fit is measured as, $\mu(tWZ) = 1.91^{+0.95}_{-0.82}$. The best fit value of
 1303 the signal strength is inconsistent with 1 by 9%. This indicates a disagreement between data and the post-fit model
 1304 within post-fit model uncertainties. This may suggest that there is some mis-modelling in the backgrounds of the
 1305 post-fit model. Since there is a small number of events in the regions of tetralepton channel, the disagreement may

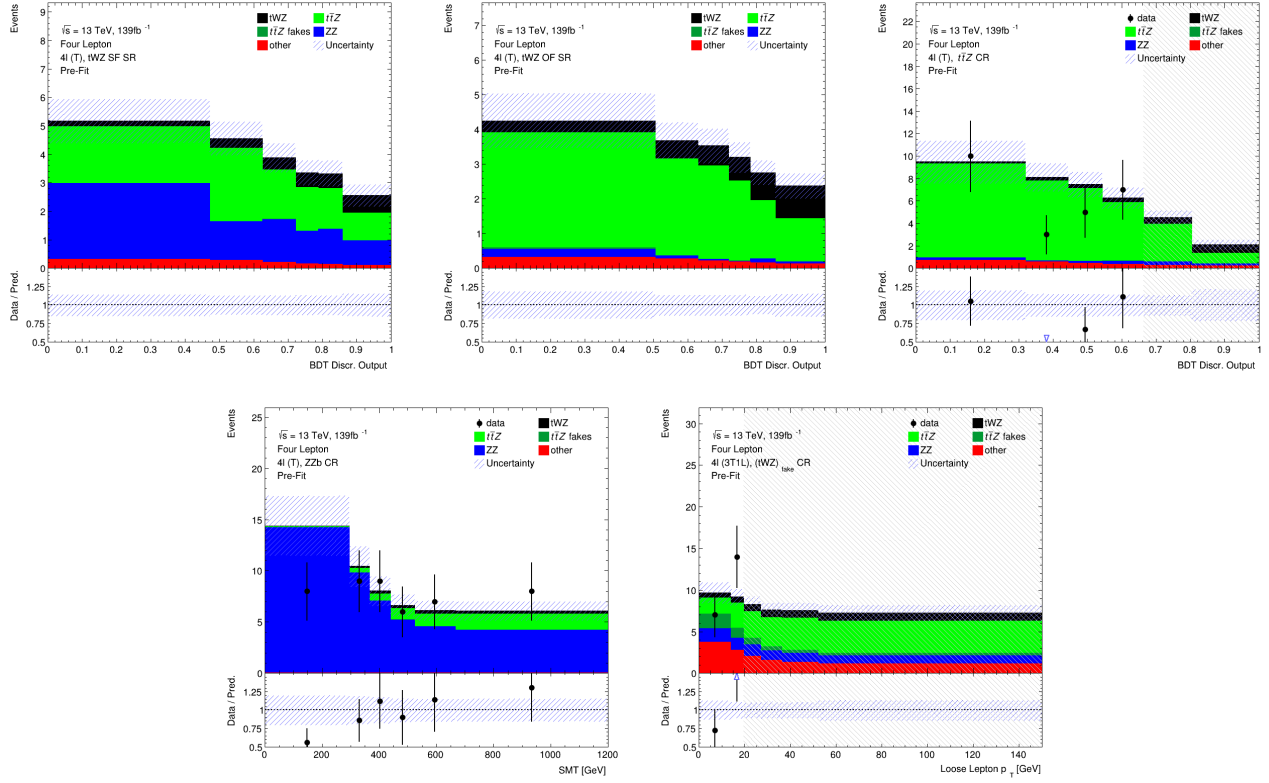


Figure 43: Pre-fit distributions (blinded) of variables used in the fit are shown. **From top left to bottom right:** The event-level BDT Disc. Output in the tWZ SF SR, the event-level BDT Disc. Output in the tWZ OF SR, the event-level BDT Disc. Output in the ttZ CR, $SMT = \sum p_T(\ell) + \sum p_T(jet) + E_T^{\text{miss}}$ in the ZZb CR, and p_T (loose lepton) in the $(tWZ)_\text{fake}$ (3T1L) CR. The data is given by the black points and the MC predictions for each process are given by the filled histograms. The vertical lines on the data points represent the statistical uncertainty in the data and the diagonally-lined bands represent the total (statistical and systematic added in quadrature) uncertainty. The lower panel in each plot shows the ratios of the data to the theoretical predictions. Bins in the CRs with $\frac{\text{signal}}{\text{background}}$ greater than 0.1 are kept blinded. Blinded bins in the CRs are shaded with black diagonal lines and their data points are omitted. The plots in the tWZ OF SR and tWZ SF SR are kept blinded by omitting the data points.

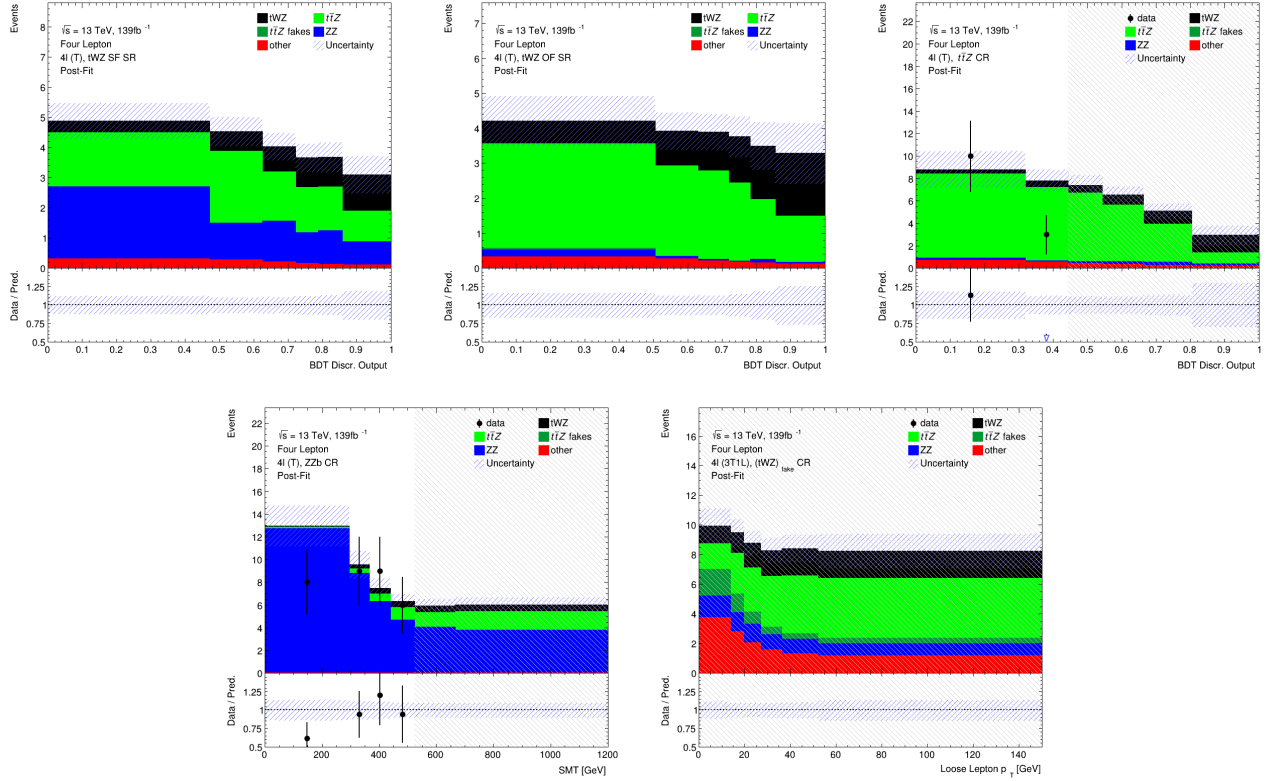


Figure 44: Post-fit distributions (blinded) of variables used in the fit are shown. **From top left to bottom right:** The event-level BDT Disc. Output in the tWZ SF SR, the event-level BDT Disc. Output in the tWZ OF SR, the event-level BDT Disc. Output in the $t\bar{t}Z$ CR, $SMT = \sum p_T(\ell) + \sum p_T(jet) + E_T^{\text{miss}}$ in the ZZb CR, and p_T (loose lepton) in the $(tWZ)_{fake}$ (3T1L) CR. The data is given by the black points and the MC predictions for each process are given by the filled histograms. The vertical lines on the data points represent the statistical uncertainty in the data and the diagonally-lined bands represent the total (statistical and systematic added in quadrature) uncertainty. The lower panel in each plot shows the ratios of the data to the theoretical predictions. Bins in the CRs with $\frac{\text{signal}}{\text{background}}$ greater than 0.1 are kept blinded. Blinded bins in the CRs are shaded with black diagonal lines and their data points are omitted. The plots in the tWZ OF SR and tWZ SF SR are kept blinded by omitting the data points.

		tWZ OF SR	tWZ SF SR	$t\bar{t}Z$ CR	ZZb CR	$(tWZ)_{\text{fake}}$ CR
$t\bar{t}Z$		13.2 ± 1.5	9.6 ± 1.1	29.9 ± 3.6	5.1 ± 0.6	18.5 ± 2.2
$t\bar{t}Z$ fakes		0.070 ± 0.047	0.033 ± 0.026	0.072 ± 0.042	0.052 ± 0.021	5.1 ± 2.3
tWZ		7.8 ± 3.3	5.3 ± 2.2	5.7 ± 2.6	2.9 ± 1.2	10.2 ± 4.3
ZZ		0.48 ± 0.12	7.7 ± 1.2	1.1 ± 0.2	40.6 ± 6.3	6.9 ± 1.1
other	$t\bar{t}$	$6e-06 \pm 3e-06$	0.25 ± 0.44	0.27 ± 0.22	$6e-06 \pm 3e-06$	2.4 ± 0.9
	tZq	0.083 ± 0.040	0.076 ± 0.035	0.064 ± 0.030	0.060 ± 0.024	4.9 ± 0.7
	$t\bar{t}tW$	0.0067 ± 0.0079	0.0028 ± 0.0028	$6e-06 \pm 3e-06$	0.0023 ± 0.0056	0.94 ± 0.29
	WZ	0.04 ± 0.02	0.04 ± 0.02	0.013 ± 0.013	0.047 ± 0.033	1.8 ± 0.4
	$t\bar{t}t$	0.0010 ± 0.0007	0.002 ± 0.001	0.014 ± 0.005	$6e-06 \pm 3e-06$	0.010 ± 0.003
	$t\bar{t}\bar{t}$	0.009 ± 0.008	0.011 ± 0.008	0.06 ± 0.02	$6e-06 \pm 3e-06$	0.02 ± 0.01
	$t\bar{t}WW$	0.029 ± 0.026	0.03 ± 0.02	0.3 ± 0.1	0.01 ± 0.03	0.2 ± 0.1
	$VVV(V = W/Z)$	0.3 ± 0.1	0.2 ± 0.1	0.10 ± 0.02	0.17 ± 0.05	0.26 ± 0.08
	$t\bar{t}H$	0.9 ± 0.2	0.7 ± 0.1	2.0 ± 0.4	0.20 ± 0.03	2.2 ± 0.5
	Total	22.9 ± 3.0	24.0 ± 2.1	39.4 ± 3.4	49.1 ± 6.0	53.4 ± 4.3
	data	-	-	36	49	57

Table 13: The expected number of events (after the fit) for each sample in each region is shown.

1306 be due to statistical fluctuations in data or simulation.

1307
1308 The effect of each systematic uncertainty on the POI, $\mu(tWZ)$, in the fit can be studied from a *ranking plot* [84].
1309 A ranking plot lists the nuisance parameters used in the fit in order of their *impact* on the POI. The impact of a
1310 nuisance parameter describes to what degree the nuisance parameter effects the extracted value of the POI from
1311 the fit. The impact of a nuisance parameter (denoted by θ) is calculated by first fixing the pre-fit and post-fit
1312 uncertainties (denoted by $\Delta\theta$ and $\Delta\hat{\theta}$ respectively) of all the nuisance parameters to ± 1 , performing the fit, and
1313 extracting the nominal value of the POI. The impact of a given nuisance parameter is then defined by the difference
1314 in this reference POI value to a POI value extracted from a fit performed by removing the given nuisance parameter.
1315 In Figure 45, a ranking plot showing the impact of the systematic uncertainties on the POI, $\mu(tWZ)$ is shown.
1316 The systematic uncertainties with largest impacts are the cross sections of $t\bar{t}Z$ and ZZ , and shape modelling on
1317 $t\bar{t}Z$ ($t\bar{t}Z$ triangular shape) and tWZ (tWZ -DR2 and tWZ triangular shape). The cross section of ZZ is slightly
1318 shifted down in the fit from its nominal value. The $t\bar{t}Z$ cross section, tWZ -DR2 and $t\bar{t}Z$ triangular shape nuisance
1319 parameters are similarly shifted down in the fit from their nominal values, but to a much lesser degree than the
1320 cross section of ZZ . These pulls are all within 1σ uncertainty and are thus relatively small. It is expected that
1321 the modelling uncertainties (shape and normalisations) of the most dominant backgrounds (e.g. $t\bar{t}Z$, ZZ) have
1322 relatively large impacts on $\mu(tWZ)$, since the uncertainty of the analysis is dominated by statistical uncertainty.

1323 4.10.2 Trilepton and Tetralepton Channels

1324 In the section, an expected upper limit and an expected significance are set on the signal strength of tWZ
1325 ($\mu(tWZ)$) from the combined fit across all regions of tWZ in the tetralepton and trilepton channels.

1326
1327 The trilepton channel is an entirely independent analysis [99] that uses separate data and simulated events
1328 compared to the tetralepton channel. Although the trilepton channel uses separate data and simulated events, the
1329 treatment of the statistical and systematic uncertainties (and therefore the statistical model) in the combined fit
1330 is entirely coherent with the tetralepton channel. Therefore the inclusion of the trilepton channel in the combined
1331 fit is only a matter of adding the regions in the trilepton channel to the likelihood definition. The trilepton
1332 analysis follows a similar analysis strategy to that of the tetralepton analysis. It includes an event-level BDT
1333 which aims to discriminate between the tWZ and all background as well as an object-level BDT which aims to
1334 identify hadronically decaying W bosons to discriminate between tWZ and the large WZ background. One tWZ
1335 SR is defined and five CRs are defined. The WZ and $t\bar{t}Z$ CRs are defined to constrain the dominant WZ and
1336 $t\bar{t}Z$ backgrounds. Three CRs which require that one of the three selected leptons are loose, are defined for WZ ,
1337 $t\bar{t}Z$ and tWZ in order to constraint the fake lepton component (using the MC template method - similar to the
1338 method used in Section 4.6 to estimate the fake lepton component).

1339
1340 The expected upper limit of tWZ in the trilepton channel is measured as, $\mu_{up}^{exp} = 2.65^{+3.67}_{-1.91}$. The expected signif-

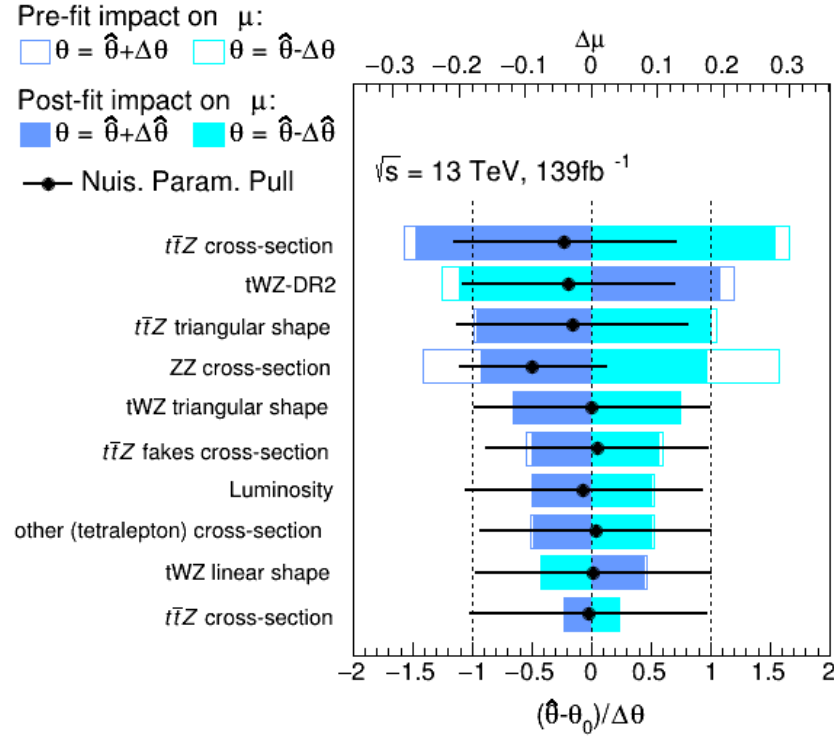


Figure 45: A ranking plot showing the impact (ordered from top to bottom via decreasing impact) of the systematic uncertainties (top 10) on the POI, $\mu(tWZ)$, in the tetralepton channel is shown. The best-fit value of the nuisance parameter is given by $\hat{\theta}$. The post-fit and pre-fit uncertainties are given by $\Delta\hat{\theta}$ and $\Delta\theta$ respectively. The post-fit and pre-fit impact of each nuisance parameter on $\mu(tWZ)$ are shown with the solid and lined rectangles respectively. The empty and solid blue rectangles correspond to the pre-fit and post-fit impacts on $\mu(tWZ)$ respectively. These impacts are shown on the upper axis ($\Delta\mu$). On the lower axis, the nuisance parameter pull, $\frac{\theta - \theta_0}{\Delta\theta}$, is shown (θ_0 is the nominal pre-fit value of the nuisance parameter). The nuisance parameter pull is indicated by the black points, with their relative post-fit errors ($\frac{\Delta\hat{\theta}}{\Delta\theta}$) shown by the black horizontal error bars.

1341 significance of tWZ in the trilepton channel is measured as, $Z_\mu^{exp} = 0.75\sigma$. The best-fit value of the signal strength,
 1342 $\mu(tWZ) = \frac{\sigma(tWZ)}{\sigma(tWZ)_{SM}}$, from the likelihood fit is measured as, $\mu(tWZ) = 1.16^{+1.33}_{-1.30}$. The best fit value of the signal
 1343 strength is consistent with 1. This indicates an agreement between data and the post-fit model within post-fit
 1344 model uncertainties. Therefore, this demonstrates that the model is able to sufficiently model the background
 1345 processes. In Table 14, the nuisance parameters that are included (or excluded) in terms of the likelihood function
 1346 corresponding to a certain channel, used in the fit, are shown. Note that the $\sigma(tWZ - DR2)$ systematic uncertainty
 1347 was not included in the trilepton analysis, and the trilepton analysis was unaltered when used in this analysis for
 1348 the combined fit. The expected upper limit of tWZ across both channels is measured as, $\mu_{up}^{exp} = 1.43^{+2.04}_{-1.03}$. The
 1349 expected significance of tWZ across both channels is measured as, $Z_\mu^{exp} = 1.61\sigma$. The best-fit value of the signal
 1350 strength, $\mu(tWZ) = \frac{\sigma(tWZ)}{\sigma(tWZ)_{SM}}$, from the likelihood fit is measured as, $\mu(tWZ) = 1.80^{+0.70}_{-0.65}$. In Figure 46, the
 1351 expected upper limits and the best-fit values of $\mu(tWZ)$ in the trilepton channel, tetralepton channel and both
 1352 channels combined are shown.
 1353 It can be seen that the sensitivity of tWZ is mostly driven by the tetralepton analysis, with the trilepton analysis
 1354 attributing a small decrease in the expected upper limit of the combined analysis, and its associated uncertainty.
 1355 The best fit value for the signal strength on tWZ , $\mu(tWZ)$, and the expected limits for the tri- and tetralepton
 1356 channels are consistent with one-another (their uncertainties overlap). Therefore it is appropriate to combine these
 1357 two analyses. In Figure 47, a ranking plot showing the impact of the systematic uncertainties on the POI, $\mu(tWZ)$,
 1358 in the combined fit across both the tri- and tetralepton channels is shown.
 1359 Some nuisance parameters are pulled down from their nominal pre-fit values, however these are all within 1σ
 1360 uncertainty and are thus relatively small. The systematic uncertainties with largest impacts are the cross sections
 1361 of $t\bar{t}Z$, ZZ and $WZ+b$, and shape modelling on $t\bar{t}Z$ ($t\bar{t}Z$ triangular shape). The aforementioned nuisance parameters
 1362 are slightly shifted down in the fit from their nominal value. The lower ranked systematic uncertainties are pulled

Nuisance Parameter	Channel	
	trilepton	tetralepton
$\sigma(t\bar{t}H)$	✓	✓
$\sigma(t\bar{t}Z)$	✓	✓
$\sigma(WZ)$	✓	✓
$\sigma(tZq)$	✓	✓
$\sigma(ZZ)$	✓	✓
$\sigma(\text{other(trilepton)})$	✓	✗
$\sigma(\text{other(tetralepton)})$	✗	✓
$\sigma(t\bar{t}Z)_{\text{fakes}}$	✗	✓
$\sigma(t\bar{t})_{\text{fakes}}$	✓	✗
$\sigma(Z + \text{jets})_{\text{fakes}}$	✓	✗
Luminosity	✓	✓
jvt	✓	✓
pileup	✓	✓
DL1r SF (b jets)	✓	✓
DL1r SF (light jets)	✓	✓
$\sigma(tWZ - DR2)$	✗	✓
lepton SF	✓	✓
$t\bar{t}Z$ triangular shape	✓	✓
$t\bar{t}Z$ linear shape	✓	✓
$WZ + b$ triangular shape	✓	✗
$WZ + b$ linear shape	✓	✗
$WZ + c$ triangular shape	✓	✗
$WZ + c$ linear shape	✓	✗

Table 14: A summary of the nuisance parameters used in the combined fit is shown. Nuisance parameters that are included in terms of the likelihood function corresponding to a certain channel are indicated with a ✓ and those which are excluded are indicated with a ✗.

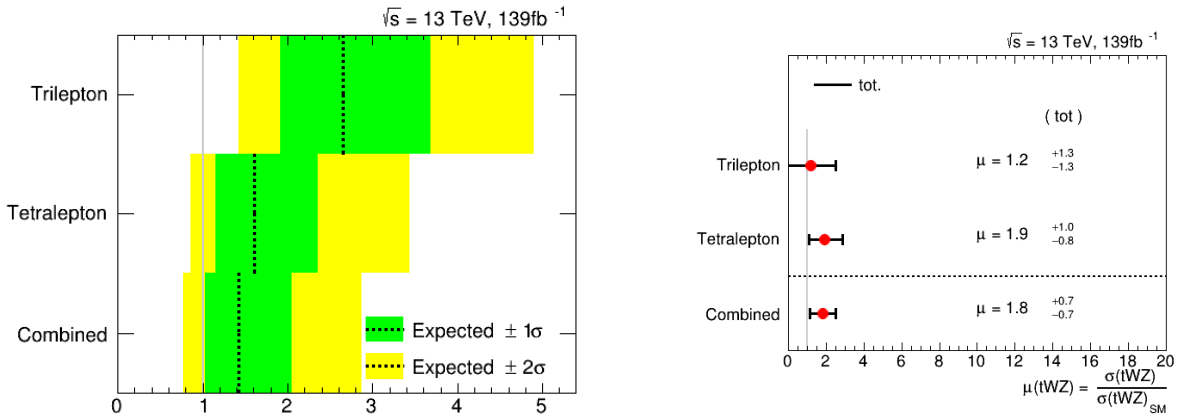


Figure 46: **Left:** The expected upper limits of the trilepton channel, tetralepton channel and both channels combine are shown. The y-axis shows the channels in which the fitting procedure was performed. The expected limits are represented by the vertical dotted line. One- and two- σ uncertainty bands are shown in green and yellow respectively. The vertical grey line indicates when $\mu(tWZ) = 1$. **Right:** The best-fit values of $\mu(tWZ)$ from the fit for the trilepton channel, tetralepton channel and both channels combined are shown. The y-axis shows the channels in which the fitting procedure was performed. The signal strength $\mu(tWZ)$ is shown on the x-axis. The nominal signal strengths are represented by the red dots. The total uncertainty associated with the best-fit $\mu(tWZ)$ value is shown by the black error bars.

in the fit from their nominal values, but to a much lesser degree than the cross section of those mentioned above.
 It is expected that the modelling uncertainties (shape and normalisations) of the most dominant backgrounds (e.g. $t\bar{t}Z$, ZZ and $WZ + b$) have relatively large impacts on $\mu(tWZ)$, since the uncertainty of the analysis is dominated by statistical uncertainty.

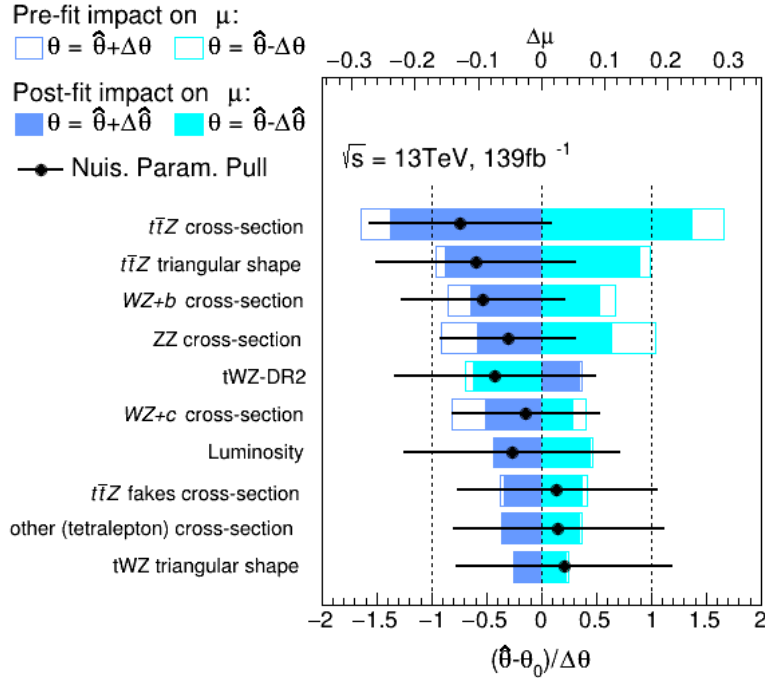


Figure 47: A ranking plot showing the impact of the systematic uncertainties (top 10) on the POI, $\mu(tWZ)$, in the combined fit across both the tri- and tetralepton channels is shown. The best-fit value of the nuisance parameter is given by $\hat{\theta}$. The post-fit and pre-fit uncertainties are given by $\Delta\hat{\theta}$ and $\Delta\theta$ respectively. The post-fit and pre-fit impact of each nuisance parameter on $\mu(tWZ)$ are shown with the solid and lined rectangles respectively. The empty and solid blue rectangles correspond to the pre-fit and post-fit impacts on $\mu(tWZ)$ respectively. These impacts are shown on the upper axis ($\Delta\mu$). On the lower axis, the nuisance parameter pull, $\frac{\hat{\theta} - \theta_0}{\Delta\theta}$, is shown (θ_0 is the nominal pre-fit value of the nuisance parameter). The nuisance parameter pull is indicated by the black points, with their relative post-fit errors ($\frac{\Delta\hat{\theta}}{\Delta\theta}$) shown by the black horizontal error bars.

1367 4.10.2.1 Projection to Higher Luminosity

1368 The expected significance of tWZ across both channels was measured as 1.61σ and it is likely that the analysis is
 1369 statistically limited. Therefore, the question naturally arises whether or not it is possible to observe tWZ with a 3σ
 1370 or 5σ significance and how much data one would need to achieve this. In this section we apply a fully blinded fit to
 1371 the Asimov dataset for integrated luminosities larger than the 139fb^{-1} currently available from the ATLAS Full Run
 1372 2 dataset. This study gives us insight into the sensitivity of tWZ which we could expect if we were to replicate the
 1373 current analysis, given more data. Given the upgrades planned for the LHC and the ATLAS detector, we will soon
 1374 expect a large increase in available pp collision data (reaching $\mathcal{L} = 3000\text{fb}^{-1}$ [36]). This study therefore gives us an
 1375 idea of the sensitivity of tWZ which we can expect in the future. It would also provide a clear indication whether
 1376 or not the uncertainties in this analysis is dominated by statistical uncertainties. In Figure 48, the expected upper
 1377 limit and significance for combined fully blinded fits to the Asimov dataset across both the tri- and tetralepton
 1378 channels for a range integrated luminosities are shown.

1379 As we increase the total integrated luminosity, the sensitivity of tWZ increases. The increase in sensitivity is shown
 1380 by the rapid decrease of the expected upper limit and the rapid increase of the expected significance with increasing
 1381 integrated luminosity. It can be noted that a 3σ expected significance is achieved at $\mathcal{L} \sim 400 \text{ fb}^{-1}$, indicating
 1382 evidence for observation of tWZ . The 5σ significance 'discovery' standard is above our 1000fb^{-1} luminosity range
 1383 of study. Furthermore, these plots show that the sensitivity of tWZ is hindered by the low amount of events we
 1384 observe, rather than the systematic effects. This is evident since increasing the luminosity, therefore increasing the
 1385 number of events we see in the detector, directly causes a steady increase in sensitivity.

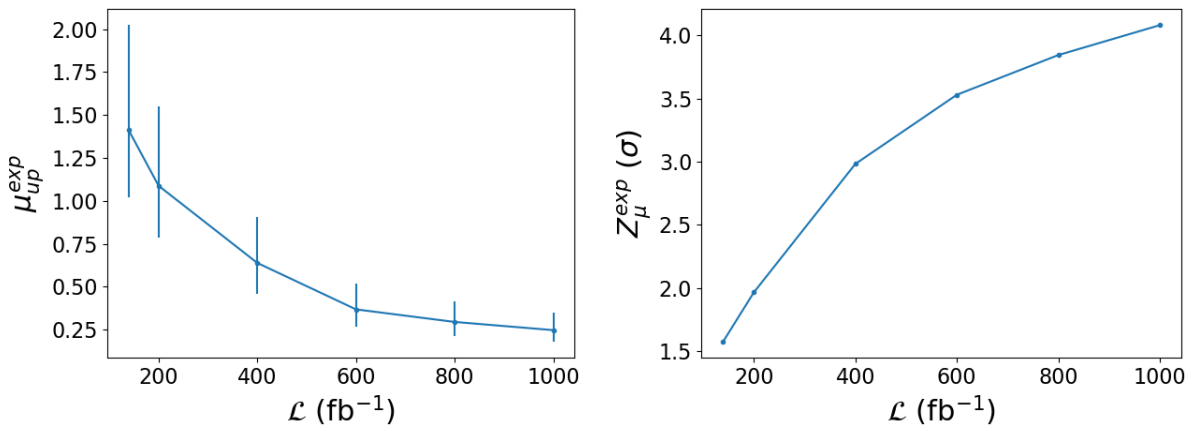


Figure 48: The expected upper limit (left) and significance (right) for combined fully blinded fits to the Asimov dataset across both the tri- and tetralepton channels for a range integrated luminosities are shown. **Left:** The integrated luminosity, \mathcal{L} , is shown on the x-axis. The expected upper limit, μ_{up}^{exp} , is shown on the y-axis. The vertical lines represent the total uncertainty ($\pm 1\sigma$) on the expected upper limit. **Right:** The integrated luminosity, \mathcal{L} , is shown on the x-axis. The expected significance, Z_μ^{exp} , is shown on the y-axis. The vertical lines represent the total uncertainty ($\pm 1\sigma$) on the expected significance.

1386

Chapter 5

1387

Summary and Conclusions

1388 The tWZ process is an important process in the search for new physics since its cross section is sensitive to the
 1389 charged and neutral couplings to the top quark, which is strongly coupled to the Higgs boson. The top quark's
 1390 couplings are often modified in many scenarios of new physics that aim to resolve the Hierarchy Problem, therefore
 1391 a constraint placed on the cross section of tWZ is expected to be impactful in constraining such BSM models. A
 1392 search for tWZ production using 139 fb^{-1} of pp collision data at a centre-of-mass energy of $\sqrt{s} = 13 \text{ TeV}$, recorded
 1393 by the ATLAS experiment at CERN, has been presented. This thesis targeted the tetralepton final state channel.
 1394 Two SRs and three CRs were defined. Two SRs, instead of one, were defined in order to suppress and constrain the
 1395 ZZ background. The dominant background processes, $t\bar{t}Z$ and ZZ were constrained by the definition of $t\bar{t}Z$ and
 1396 ZZ CRs, respectively. The dominant source of fake leptons, originating from the $t\bar{t}Z$ background, was constrained
 1397 by the $(tWZ)_{\text{fake}}$ CR, using the MC template method. Two BDTs were implemented: an object-level BDT which
 1398 aims to classify between ℓb systems coming from top quarks and an event-level BDT which aims to discriminate
 1399 between tWZ and our major backgrounds, $t\bar{t}Z$ and ZZ . The output from the object-level BDT was converted to
 1400 an event-level variable to be used as input to the event-level BDT. A kinematic reconstruction algorithm, $2\nu\text{SM}$,
 1401 was used to reconstruct top quarks in order to discriminate between tWZ and $t\bar{t}Z$. The output from this algorithm
 1402 was used as an input variable to the event-level BDT. The trained BDT was shown to discriminate well between
 1403 signal and background events. Using a modified Asimov dataset in the SRs and real data in the CRs, a blinded
 1404 maximum-likelihood fit was performed across all regions in the tetralepton channel. The best-fit value of the signal
 1405 strength in the tetralepton channel was,

$$\mu(tWZ) = 1.91^{+0.95}_{-0.82} \quad (5.1)$$

1406 with an expected significance of 1.44σ . The expected upper limit on the signal strength of tWZ in the tetralepton
 1407 channel was,

$$\mu_{up}^{\text{exp}} = 1.61^{+2.35}_{-1.16} \quad (5.2)$$

1408 To further increase the sensitivity of tWZ , a blinded maximum-likelihood fit was performed across all regions across
 1409 the trilepton (studied in an independent analysis by Benjamin Warren (UCT) [99]) and tetralepton channels. The
 1410 best-fit value of the signal strength across both the trilepton and tetralepton channels were,

$$\mu(tWZ) = 1.80^{+0.70}_{-0.65} \quad (5.3)$$

1411 with an expected significance of 1.61σ . The expected upper limit on the signal strength of tWZ across both the
 1412 trilepton and tetralepton channels were,

$$\mu_{up}^{\text{exp}} = 1.43^{+2.04}_{-1.03} \quad (5.4)$$

1413 Although this result does not satisfy the 3σ evidence nor the 5σ discovery standards, an unblinding of this analysis
 1414 in the future may still provide the tightest ever constraint on the tWZ process. The results in this analysis are
 1415 heavily statistically limited, it is therefore expected that future analyses of this process, using larger datasets (such
 1416 as that from the HL-LHC), would significantly improve the results.

1417

Bibliography

- [1] M. Aaboud et al. “Electron reconstruction and identification in the ATLAS experiment using the 2015 and 2016 LHC proton–proton collision data at $\sqrt{s} = 13$ TeV”. In: *The European Physical Journal C* 79.8 (Aug. 2019). ISSN: 1434-6052. DOI: 10.1140/epjc/s10052-019-7140-6. URL: <http://dx.doi.org/10.1140/epjc/s10052-019-7140-6>.
- [2] M. Aaboud et al. “Measurement of the $t\bar{t}Z$ and $t\bar{t}W$ cross sections in proton-proton collisions at $\sqrt{s} = 13$ TeV with the ATLAS detector”. In: *Phys. Rev. D* 99 (7 Apr. 2019), p. 072009. DOI: 10.1103/PhysRevD.99.072009. URL: <https://link.aps.org/doi/10.1103/PhysRevD.99.072009>.
- [3] Aaboud, M. and Aad, G. and Abbott, B. and Abbott, D. C. and Abdinov, O. and Abed Abud, A. and Abhayasinghe, D. K. and Abidi, S. H. and AbouZeid, O. S. and et al. “Measurement of ZZ production in the $\ell\ell\nu\nu$ final state with the ATLAS detector in pp collisions at $s \sqrt{s} = 13$ TeV”. In: *Journal of High Energy Physics* 2019.10 (Oct. 2019). ISSN: 1029-8479. DOI: {10.1007/jhep10(2019)127}. URL: %7B[http://dx.doi.org/10.1007/JHEP10\(2019\)127](http://dx.doi.org/10.1007/JHEP10(2019)127)%7D.
- [4] G. Aad et al. “Measurement of the $t\bar{t}$ production cross-section in the lepton+jets channel at $s=13$ TeV with the ATLAS experiment”. In: *Physics Letters B* 810 (2020), p. 135797. ISSN: 0370-2693. DOI: <https://doi.org/10.1016/j.physletb.2020.135797>. URL: <https://www.sciencedirect.com/science/article/pii/S0370269320306006>.
- [5] G. Aad et al. “Muon reconstruction performance of the ATLAS detector in proton–proton collision data at $\sqrt{s} = 13$ TeV”. In: *The European Physical Journal C* 76.5 (May 2016). ISSN: 1434-6052. DOI: 10.1140/epjc/s10052-016-4120-y. URL: <http://dx.doi.org/10.1140/epjc/s10052-016-4120-y>.
- [6] Shunichi Akatsuka and Shion Chen. *Isolation WPs summary: PLV + LowPtPLV*. Oct. 2019. URL: <https://indico.cern.ch/event/854783/contributions/3595486/attachments/1929380/3195230/PLV-Summary.pdf>.
- [7] G. ALTARELLI, R. BARBIERI, and F. CARAVAGLIOS. “ELECTROWEAK PRECISION TEST: A CONSISTENT REVIEW”. In: *International Journal of Modern Physics A* 13.07 (Mar. 1998), pp. 1031–1058. ISSN: 1793-656X. DOI: 10.1142/s0217751x98000469. URL: <http://dx.doi.org/10.1142/S0217751X98000469>.
- [8] Guido Altarelli. *The Higgs and the Excessive Success of the Standard Model*. 2014. arXiv: 1407.2122 [hep-ph].
- [9] J. Alwall et al. “The automated computation of tree-level and next-to-leading order differential cross sections, and their matching to parton shower simulations”. In: *JHEP* 07 (2014), p. 079. DOI: 10.1007/JHEP07(2014)079. arXiv: 1405.0301 [hep-ph].
- [10] Aaron Armbruster. *Asymptotic Formulae*. Feb. 2013. URL: https://indico.cern.ch/event/233551/contributions/493678/attachments/389871/542293/asymptotics_armbruster.pdf.
- [11] Pierre Astier et al. “Kalman filter track fits and track breakpoint analysis”. In: *Nuclear Instruments and Methods in Physics Research Section A: Accelerators, Spectrometers, Detectors and Associated Equipment* 450.1 (2000), pp. 138–154. ISSN: 0168-9002. DOI: [https://doi.org/10.1016/S0168-9002\(00\)00154-6](https://doi.org/10.1016/S0168-9002(00)00154-6). URL: <https://www.sciencedirect.com/science/article/pii/S0168900200001546>.
- [12] ATLAS Collaboration. “ATLAS b -jet identification performance and efficiency measurement with $t\bar{t}$ events in pp collisions at $\text{sqrt}s = 13$ TeV”. In: *Eur. Phys. J. C* 79 (2019), p. 970. DOI: 10.1140/epjc/s10052-019-7450-8. arXiv: 1907.05120 [hep-ex].
- [13] ATLAS Collaboration. “Electron and photon performance measurements with the ATLAS detector using the 2015-2017 LHC proton-proton collision data”. In: *JINST* 14 (2019), P12006. DOI: 10.1088/1748-0221/14/12/P12006. arXiv: 1908.00005 [hep-ex].

- [14] ATLAS Collaboration. “Identification and rejection of pile-up jets at high pseudorapidity with the ATLAS detector”. In: *Eur. Phys. J. C* 77 (2017), p. 580. DOI: 10.1140/epjc/s10052-017-5081-5. arXiv: 1705.02211 [hep-ex].
- [15] ATLAS Collaboration. “Measurements of b -jet tagging efficiency with the ATLAS detector using $t\bar{t}$ events at $\sqrt{s} = 13\text{TeV}$ ”. In: *JHEP* 08 (2018), p. 089. DOI: 10.1007/JHEP08(2018)089. arXiv: 1805.01845 [hep-ex].
- [16] ATLAS Collaboration. “Muon reconstruction and identification efficiency in ATLAS using the full Run 2 pp collision data set at $\sqrt{s} = 13\text{TeV}$ ”. In: (2020). arXiv: 2012.00578 [hep-ex].
- [17] Manuel Guth on behalf of the ATLAS collaboration. *Deep-Neural-Network-based b -Tagging as Basis for Improvements in Top Analyses*. URL: <https://cds.cern.ch/record/2693088/files/ATL-PHYS-SLIDE-2019-751.pdf>.
- [18] ATLAS Internal. *Electron Efficiencies for Analyses*. 2021. URL: <https://twiki.cern.ch/twiki/bin/viewauth/AtlasProtected/ElectronEfficienciesForAnalysis>.
- [19] ATLAS Internal. *Electron Efficiency Correlation Model*. 2021. URL: <https://twiki.cern.ch/twiki/bin/view/AtlasProtected/ElectronEfficiencyCorrelationModel>.
- [20] ATLAS Internal. *Jet Vertex Tagger for Run 2 in reco and analysis*. 2021. URL: <https://twiki.cern.ch/twiki/bin/view/AtlasProtected/JetVertexTaggerTool>.
- [21] ATLAS Internal. *Muon Efficiencies for Analyses*. 2021. URL: <https://twiki.cern.ch/twiki/bin/view/AtlasProtected/MuonEfficienciesForAnalysis>.
- [22] G. Avoni et al. “The new LUCID-2 detector for luminosity measurement and monitoring in ATLAS”. In: *JINST* 13.07 (2018), P07017. DOI: 10.1088/1748-0221/13/07/P07017.
- [23] Richard D. Ball et al. “Parton distributions for the LHC run II”. In: *Journal of High Energy Physics* 2015.4 (Apr. 2015). ISSN: 1029-8479. DOI: 10.1007/jhep04(2015)040. URL: [http://dx.doi.org/10.1007/JHEP04\(2015\)040](http://dx.doi.org/10.1007/JHEP04(2015)040).
- [24] Roger Barlow and Christine Beeston. “Fitting using finite Monte Carlo samples”. In: *Computer Physics Communications* 77.2 (1993), pp. 219–228. ISSN: 0010-4655. DOI: [https://doi.org/10.1016/0010-4655\(93\)90005-W](https://doi.org/10.1016/0010-4655(93)90005-W). URL: <https://www.sciencedirect.com/science/article/pii/001046559390005W>.
- [25] Olga Bessidskaia Bylund. *Measurement of $t\bar{t}Z$ and $t\bar{t}W$ production at ATLAS in 13 TeV data, using trilepton and same charge dimuon final states*. Tech. rep. Geneva: CERN, Aug. 2016. DOI: 10.22323/1.276.0237. URL: <https://cds.cern.ch/record/2211022>.
- [26] Enrico Bothmann et al. “Event generation with Sherpa 2.2”. In: *SciPost Physics* 7.3 (Sept. 2019). ISSN: 2542-4653. DOI: 10.21468/scipostphys.7.3.034. URL: <http://dx.doi.org/10.21468/SciPostPhys.7.3.034>.
- [27] Ilaria Brivio and Michael Trott. “The standard model as an effective field theory”. In: *Physics Reports* 793 (Feb. 2019), pp. 1–98. ISSN: 0370-1573. DOI: 10.1016/j.physrep.2018.11.002. URL: <http://dx.doi.org/10.1016/j.physrep.2018.11.002>.
- [28] Jason Brownlee. *Overfitting and Underfitting With Machine Learning Algorithms*. URL: <https://machinelearningmastery.com/overfitting-and-underfitting-with-machine-learning-algorithms/>.
- [29] Oliver Sim Brüning et al. *LHC Design Report*. CERN Yellow Reports: Monographs. Geneva: CERN, 2004. DOI: 10.5170/CERN-2004-003-V-1. URL: <https://cds.cern.ch/record/782076>.
- [30] Gustavo Burdman et al. “Colorless top partners, a 125 GeV Higgs boson, and the limits on naturalness”. In: *Physical Review D* 91.5 (Mar. 2015). ISSN: 1550-2368. DOI: 10.1103/physrevd.91.055007. URL: <http://dx.doi.org/10.1103/PhysRevD.91.055007>.
- [31] Matteo Cacciari, Gavin P. Salam, and Gregory Soyez. “The anti- k_t jet clustering algorithm”. In: *JHEP* 04 (2008), p. 063. DOI: 10.1088/1126-6708/2008/04/063. arXiv: 0802.1189 [hep-ph].
- [32] Thomas Calvet. *Automatic binning implementation in TTHFitter - Htop(bb)*. URL: https://indico.cern.ch/event/455289/contributions/1953694/attachments/1209081/1762963/Calvet_binning_Htop-160108.pdf.
- [33] Thomas Philippe Calvet. “Search for the production of a Higgs boson in association with top quarks and decaying into a b-quark pair and b-jet identification with the ATLAS experiment at LHC”. Presented 08 Nov 2017. Dec. 2017. URL: <https://cds.cern.ch/record/2296985>.

- [34] Anadi Canepa. "Searches for supersymmetry at the Large Hadron Collider". In: *Reviews in Physics* 4 (2019), p. 100033. ISSN: 2405-4283. DOI: <https://doi.org/10.1016/j.revip.2019.100033>. URL: <https://www.sciencedirect.com/science/article/pii/S2405428318300091>.
- [35] CERN Twiki - TOP WG Summary Plots. URL: <https://twiki.cern.ch/twiki/bin/view/LHCPhysics/LHCTopWGSummaryPlots>.
- [36] CERN Yellow Reports: Monographs. *CERN Yellow Reports: Monographs, Vol. 10 (2020): High-Luminosity Large Hadron Collider (HL-LHC): Technical design report.* en. 2020. DOI: 10.23731/CYRM-2020-0010. URL: <https://e-publishing.cern.ch/index.php/CYRM/issue/view/127>.
- [37] Shion Chen. *Track isolation variable for the PFlow WPs.* Oct. 2019. URL: https://indico.cern.ch/event/854783/contributions/3595529/attachments/1926980/3190772/IFF_20191003_PflowWPs.pdf.
- [38] KyungEon Choi. "Tracking and Vertexing with the ATLAS Inner Detector in the LHC Run-2". In: *Springer Proc. Phys.* 213 (2018). Ed. by Zhen-An Liu, pp. 400–403. DOI: 10.1007/978-981-13-1316-5_75.
- [39] CMS Collaboration. *Measurements of $pp \rightarrow ZZ$ production cross sections and constraints on anomalous triple gauge couplings at $\sqrt{s} = 13$ TeV.* 2020. arXiv: {2009.01186} (hep-ex).
- [40] CMS Collaboration. "Measurement of the ttbar production cross section using events with one lepton and at least one jet in pp collisions at $\sqrt{s}=13$ TeV". In: (Jan. 2017).
- [41] The ATLAS Collaboration et al. "The ATLAS Experiment at the CERN Large Hadron Collider". In: *Journal of Instrumentation* 3.08 (Aug. 2008), S08003–S08003. DOI: 10.1088/1748-0221/3/08/s08003. URL: <https://doi.org/10.1088/1748-0221/3/08/s08003>.
- [42] I. Connelly. "Performance and calibration of b-tagging with the ATLAS experiment at LHC Run-2". In: 2017.
- [43] Glen Cowan et al. "Asymptotic formulae for likelihood-based tests of new physics". In: *The European Physical Journal C* 71.2 (Feb. 2011). ISSN: 1434-6052. DOI: 10.1140/epjc/s10052-011-1554-0. URL: <http://dx.doi.org/10.1140/epjc/s10052-011-1554-0>.
- [44] Federico Demartin et al. "tWH associated production at the LHC". In: *Eur. Phys. J. C* 77.1 (2017), p. 34. DOI: 10.1140/epjc/s10052-017-4601-7. arXiv: 1607.05862 [hep-ph].
- [45] *Electron identification efficiency in data for electrons with $E_T > 30\text{GeV}$.* URL: https://atlas.web.cern.ch/Atlas/GROUPS/PHYSICS/PAPERS/EGAM-2018-01/fig_16.png.
- [46] F. Englert and R. Brout. "Broken Symmetry and the Mass of Gauge Vector Mesons". In: *Phys. Rev. Lett.* 13 (9 Aug. 1964), pp. 321–323. DOI: 10.1103/PhysRevLett.13.321. URL: <https://link.aps.org/doi/10.1103/PhysRevLett.13.321>.
- [47] *Errors in weighted histograms.* URL: <https://www.zeuthen.desy.de/~wischnew/amanda/discussion/wgterror/working.html>.
- [48] Lyndon Evans and Philip Bryant. "LHC Machine". In: *Journal of Instrumentation* 3.08 (Aug. 2008), S08001–S08001. DOI: 10.1088/1748-0221/3/08/s08001. URL: <https://doi.org/10.1088/1748-0221/3/08/s08001>.
- [49] Guido Fantini et al. *The formalism of neutrino oscillations: an introduction.* 2020. arXiv: 1802.05781 [hep-ph].
- [50] *Forward Jet Vertex Tagging: A new technique for the identification and rejection of forward pileup jets.* Tech. rep. All figures including auxiliary figures are available at <https://atlas.web.cern.ch/Atlas/GROUPS/PHYSICS/PUBNOTES/ATL-PHYS-PUB-2015-034>. Geneva: CERN, Aug. 2015. URL: <https://cds.cern.ch/record/2042098>.
- [51] Stefano Frixione, Paolo Nason, and Carlo Oleari. "Matching NLO QCD computations with parton shower simulations: the POWHEG method". In: *JHEP* 11 (2007), p. 070. DOI: 10.1088/1126-6708/2007/11/070. arXiv: 0709.2092 [hep-ph].
- [52] Michele Gallinaro. "Top quark physics: A tool for discoveries". In: *Journal of Physics Conference Series* 447 (July 2013), pp. 2012–. DOI: 10.1088/1742-6596/447/1/012012.
- [53] *Good Run Lists for Analysis Run 2 - ATLAS Twiki.* URL: <https://twiki.cern.ch/twiki/bin/viewauth/AtlasProtected/GoodRunListsForAnalysisRun2>.
- [54] *GoodRunListsForAnalysisRun2.* URL: <https://twiki.cern.ch/twiki/bin/viewauth/AtlasProtected/GoodRunListsForAnalysisRun2>.

- [55] Particle Data Group et al. “Review of Particle Physics”. In: *Progress of Theoretical and Experimental Physics* 2020.8 (Aug. 2020). 083C01. ISSN: 2050-3911. DOI: 10.1093/ptep/ptaa104. eprint: <https://academic.oup.com/ptep/article-pdf/2020/8/083C01/33653179/ptaa104.pdf>. URL: <https://doi.org/10.1093/ptep/ptaa104>.
- [56] Trevor Hastie. *The elements of statistical learning : data mining, inference, and prediction*. New York: Springer, 2009. ISBN: 978-0-387-84858-7.
- [57] Peter W. Higgs. “Broken Symmetries and the Masses of Gauge Bosons”. In: *Phys. Rev. Lett.* 13 (1964). Ed. by J. C. Taylor, pp. 508–509. DOI: 10.1103/PhysRevLett.13.508.
- [58] Peter W. Higgs. “Spontaneous Symmetry Breakdown without Massless Bosons”. In: *Phys. Rev.* 145 (1966), pp. 1156–1163. DOI: 10.1103/PhysRev.145.1156.
- [59] *IFFTruthClassifier GitLab Repository*. URL: <https://gitlab.cern.ch/ATLAS-IFF/IFFTruthClassifier/-/tree/master>.
- [60] *IFFTruthClassifier Lepton Categories*. URL: <https://gitlab.cern.ch/ATLAS-IFF/IFFTruthClassifier/-/tree/master#3-details-about-the-lepton-categories>.
- [61] N. Jarosik et al. “SEVEN-YEAR WILKINSON MICROWAVE ANISOTROPY PROBE (WMAP) OBSERVATIONS: SKY MAPS, SYSTEMATIC ERRORS, AND BASIC RESULTS”. In: *The Astrophysical Journal Supplement Series* 192.2 (Jan. 2011), p. 14. ISSN: 1538-4365. DOI: 10.1088/0067-0049/192/2/14. URL: <http://dx.doi.org/10.1088/0067-0049/192/2/14>.
- [62] F. Jegerlehner. “The hierarchy problem of the electroweak Standard Model revisited”. In: (May 2013).
- [63] V. Khachatryan et al. “Measurement of the ZZ production cross section and $Z \rightarrow \ell^+\ell^-\ell^+\ell^-$ branching fraction in pp collisions at $\sqrt{s} = 13\text{TeV}$ ”. In: *Physics Letters B* 763 (2016), pp. 280–303. ISSN: 0370-2693. DOI: <https://doi.org/10.1016/j.physletb.2016.10.054>. URL: <https://www.sciencedirect.com/science/article/pii/S0370269316306256>.
- [64] H. J. W. Kirsten. *Introduction to supersymmetry*. Singapore Hackensack, NJ: World Scientific, 2010. ISBN: 978-9814293426.
- [65] Arthur Alexis Jules Lesage. *Lepton and photon performance at ATLAS and CMS*. 2017. arXiv: 1709.02598 [hep-ex].
- [66] Fabio Maltoni, Luca Mantani, and Ken Mimasu. “Top-quark electroweak interactions at high energy”. In: *Journal of High Energy Physics* 2019.10 (Oct. 2019). ISSN: 1029-8479. DOI: 10.1007/jhep10(2019)004. URL: [http://dx.doi.org/10.1007/JHEP10\(2019\)004](http://dx.doi.org/10.1007/JHEP10(2019)004).
- [67] Luigi Marchese. *Lepton and photon reconstruction and identification performance in ATLAS and CMS*. Tech. rep. Geneva: CERN, Sept. 2019. DOI: 10.22323/1.350.0237. URL: <https://cds.cern.ch/record/2688452>.
- [68] Thomas McCarthy. *Macro developed to compare t/W/Z reconstruction performance (2 ℓ , 3 ℓ , 4 ℓ)*. URL: https://indico.cern.ch/event/986357/contributions/4172907/attachments/2169451/3666801/reco_performance_macro_20210112.pdf.
- [69] Thomas McCarthy and Florian Fischer. *Exploiting full/partial $t\bar{t}$ reconstruction for background suppression in 2 ℓ* . URL: https://indico.cern.ch/event/955360/contributions/4016465/attachments/2102418/3534816/top_reco_bkgd_suppression_2L_20200915.pdf.
- [70] *MCTruthClassifier - ATLAS Twiki*. URL: <https://twiki.cern.ch/twiki/bin/view/AtlasProtected/MCTruthClassifier>.
- [71] *Measurement of the $t\bar{t}$ production cross-section and lepton differential distributions in $e\mu$ dilepton events from pp collisions at $\sqrt{s} = 13\text{ TeV}$ with the ATLAS detector*. Tech. rep. All figures including auxiliary figures are available at <https://atlas.web.cern.ch/Atlas/GROUPS/PHYSICS/CONFNOTES/ATLAS-CONF-2019-041>. Geneva: CERN, Aug. 2019. URL: <https://cds.cern.ch/record/2686255>.
- [72] F. Meloni. “Primary vertex reconstruction with the ATLAS detector”. In: *Journal of Instrumentation* 11.12 (Dec. 2016), pp. C12060–C12060. DOI: 10.1088/1748-0221/11/12/c12060. URL: <https://doi.org/10.1088/1748-0221/11/12/c12060>.
- [73] Ken Mimasu. *Top quark electroweak interactions*. 2021. arXiv: 2105.10261 [hep-ph].
- [74] Aditya Mishra. *Metrics to Evaluate your Machine Learning Algorithm*. URL: <https://towardsdatascience.com/metrics-to-evaluate-your-machine-learning-algorithm-f10ba6e38234>.

- [75] Users MissMJ and Cush. *Standard model of elementary particles - Wikimedia Commons*. URL: https://en.wikipedia.org/wiki/File:Standard_Model_of_Elementary_Particles.svg.
- [76] *Monte Carlo to Monte Carlo scale factors for flavour tagging efficiency calibration*. Tech. rep. ATL-PHYS-PUB-2020-009. Geneva: CERN, May 2020. URL: <https://cds.cern.ch/record/2718610>.
- [77] Hussain Mujtaba. *What is Cross Validation in Machine learning? Types of Cross Validation*. URL: <https://www.mygreatlearning.com/blog/cross-validation/>.
- [78] *MuonSelectionTool, ATLAS TWiki*. URL: <https://twiki.cern.ch/twiki/bin/view/Atlas/MuonSelectionTool>.
- [79] O. Ogul Oncel. “Search for Single Top Quark Production in Association with a W and a Z Boson in the 3 Lepton Final State with the ATLAS Experiment at 13 TeV”. Presented 04 Jun 2018. May 2018. URL: <http://cds.cern.ch/record/2625170>.
- [80] António Onofre. “Top Quark Couplings and Search for New Physics at the LHC”. In: *Journal of Physics Conference Series* 447 (July 2013), pp. 2030–. DOI: 10.1088/1742-6596/447/1/012030.
- [81] *Option to force a shape withing an error band by hand - TRF documentation*. URL: https://trexfitter-docs.web.cern.ch/trexfitter-docs/model_building/shape/.
- [82] *Performance of the ATLAS Electron and Photon Trigger in p-p Collisions at $\sqrt{s} = 7$ TeV in 2011*. Tech. rep. All figures including auxiliary figures are available at <https://atlas.web.cern.ch/Atlas/GROUPS/PHYSICS/CONFNOTES/ATLAS-CONF-2012-048>. Geneva: CERN, May 2012. URL: <https://cds.cern.ch/record/1450089>.
- [83] *Pileup jet recommendations*. URL: <https://twiki.cern.ch/twiki/bin/view/AtlasProtected/PileupJetRecommendations>.
- [84] Michele Pinamonti. *Statistical methods at ATLAS and CMS*. URL: https://indico.cern.ch/event/727396/contributions/3021899/attachments/1657532/2654085/Statistical_methods_at_ATLAS_and_CMS_2.pdf.
- [85] *Recommended isolation working points*. URL: <https://twiki.cern.ch/twiki/bin/view/AtlasProtected/RecommendedIsolationWPs>.
- [86] *scikit-learn Documentation - Gradient Boosting Classifier*. URL: <https://scikit-learn.org/stable/modules/generated/sklearn.ensemble.GradientBoostingClassifier.html>.
- [87] *Scikit-Learn GradientBoostingClassifier Documentation*. URL: <https://scikit-learn.org/stable/modules/generated/sklearn.ensemble.GradientBoostingClassifier.html>.
- [88] Pedro Ferreira da Silva. *Top quark production at the LHC*. 2016. arXiv: 1605.05343 [hep-ex].
- [89] T. Sjöstrand, S. Mrenna, and P. Skands. “A brief introduction to PYTHIA 8.1”. In: *Comput. Phys. Commun.* 178 (2008), pp. 852–867. DOI: 10.1016/j.cpc.2008.01.036. arXiv: 0710.3820 [hep-ph].
- [90] Torbjörn Sjöstrand et al. “An introduction to PYTHIA 8.2”. In: *Comput. Phys. Commun.* 191 (2015), p. 159. DOI: 10.1016/j.cpc.2015.01.024. arXiv: 1410.3012 [hep-ph].
- [91] Jory Sonneveld. *Searches for physics beyond the standard model at the LHC*. 2019. arXiv: 1905.06239 [hep-ex].
- [92] Mark Thomson. *Modern particle physics*. Cambridge, United Kingdom New York: Cambridge University Press, 2013. ISBN: 9781107034266.
- [93] *TopRecoObjTwikiModel*. URL: <https://twiki.cern.ch/twiki/bin/view/AtlasProtected/TopRecoObjTwikiModel>.
- [94] *Total Integrated Luminosity and Data Quality in 2015-2018 - LuminosityPublicResultsRun2*. URL: <https://twiki.cern.ch/twiki/bin/view/AtlasPublic/LuminosityPublicResultsRun2>.
- [95] Daniel R. Tovey. “Transformation properties of the transverse mass under transverse Lorentz boosts at hadron colliders”. In: *The European Physical Journal C* 79.4 (Apr. 2019). ISSN: 1434-6052. DOI: 10.1140/epjc/s10052-019-6813-5. URL: <http://dx.doi.org/10.1140/epjc/s10052-019-6813-5>.
- [96] *TRExFitter*. URL: <https://twiki.cern.ch/twiki/bin/viewauth/AtlasProtected/TtHFitter>.
- [97] *TRExFitter: Mixed data and MC fit*. URL: <https://trexfitter-docs.web.cern.ch/trexfitter-docs/AdvancedTutorial2020/Mixed/>.

- 1661 [98] Tommy Tschida. “Cross section measurements of processes with a single top quark and two vector bosons
1662 with the CMS experiment”. MA thesis. Vienna, Tech. U., 2020. DOI: 10.34726/hss.2020.79420.
- 1663 [99] Benjamin Warren. “A search for tWZ production in the trilepton channel using Run 2 data from the ATLAS
1664 experiment.” In: (2021).
- 1665 [100] Kenneth G. Wilson. “Confinement of quarks”. In: *Phys. Rev. D* 10 (8 Oct. 1974), pp. 2445–2459. DOI:
1666 10.1103/PhysRevD.10.2445. URL: <https://link.aps.org/doi/10.1103/PhysRevD.10.2445>.
- 1667 [101] Katherine Woodruff. *Introduction to boosted decision trees*. URL: <https://indico.fnal.gov/event/15356/contributions/31377/attachments/19671/24560/DecisionTrees.pdf>.
- 1668